Fakultät für Maschinenwesen
Lehrstuhl für Nukleartechnik
CERN Radiation Protection Group

CERN Radiation Protection (RP) calibration facilities

Fabio Pozzi

Vollständiger Abdruck der von der Fakultät für Maschinenwesen der Technischen Universität München zur Erlangung des akademischen Grades eines

Doktor-Ingenieurs (Dr.-Ing.)

genehmigten Dissertation.

Vorsitzender: Prof. Dr.-Ing. Harald Klein

Prüfer der Dissertation:

1. Prof. Dr. Rafael Macián-Juan
2. Prof. Dr.-Ing. Stefano Agosteo

Die Dissertation wurde am 21.09.2015 bei der Technischen Universität München eingereicht und durch die Fakultät für Machinenwesen am 14.04.2016 angenommen.

To Gioia, the Mate of my heart
Elodie Myriam, the Smile of our hearts
and Natanaele, the Angel of our lives

Contents

List of Figures

List of Tables

Abstract

Radiation protection calibration facilities are essential to ensure the correct operation of radiation protection instrumentation. Calibrations are performed in specific radiation fields according to the type of instrument to be calibrated: neutrons, photons, X-rays, beta and alpha particles. Some of the instruments are also tested in mixed radiation fields as often encountered close to high-energy particle accelerators. Moreover, calibration facilities are of great importance to evaluate the performance of prototype detectors; testing and measuring the response of a prototype detector to well-known and -characterized radiation fields contributes to improving and optimizing its design and capabilities.

The CERN Radiation Protection group is in charge of performing the regular calibrations of all CERN radiation protection devices; these include operational and passive dosimeters, neutron and photon survey-meters, and fixed radiation detectors to monitor the ambient dose equivalent, H*(10), inside CERN accelerators and at the CERN borders. A new state-of-the-art radiation protection calibration facility was designed, constructed and commissioned following the related ISO recommendations to replace the previous ageing (more than 30 years old) laboratory. In fact, the new laboratory aims also at the official accreditation according to the ISO standards in order to be able to release certified calibrations. Four radiation fields are provided: neutrons, photons and beta sources and an X-ray generator. Its construction did not only involve a pure civil engineering work; many radiation protection studies were performed to provide a facility that could answer the CERN calibration needs and fulfill all related safety requirements. Monte Carlo simulations have been confirmed to be a valuable tool for the optimization of the building design, the radiation protection aspects, e.g. shielding, and, as consequence, the overall cost. After the source and irradiator installation, the facility was commissioned by measuring the calibration quantities of interest, e.g. H*(10), as a function of the source-to-detector distance. In the case of neutron measurements, a comparison with the Monte Carlo results was carried out; in fact, the neutron scattering can be an important issue and the Monte Carlo method can contribute to its estimation and optimization.

Neutron calibrations often need to be performed at neutron energies or spectra

very much different from those generated by radioactive sources employed in standard calibration laboratories. Unfortunately, fields with a broad neutron spectrum extending to a few GeVs are very rare and the scientific community is calling for worldwide sharing of the existing facilities. The CERN RP group has been managing the CERN-EU high-energy Reference Field (CERF) facility for 20 years, which is a unique calibration field in its kind. CERF is a workplace field that reproduces the neutron spectrum encountered in the vicinity of high-energy accelerators and at commercial flight altitudes. Within the context of providing a well-characterized workplace field to the scientific community, Monte Carlo simulations were performed with the present development version of the FLUKA code. The simulations were compared with experimental measurements showing promising results for the future ISO accreditation of the facility as workplace reference facility. Even though the accreditation process is fairly long, the work achieved so far is setting the bases to start this process in the right way.

Chapter 1

Introduction: radiation protection calibration facilities

1.1 Motivations and thesis overview

1.1.1 CERN radiation protection calibration laboratory

The Radiation Protection (RP) group of the Occupational Health & Safety and Environmental Protection (HSE) unit is in charge of the CERN radiation protection calibration laboratory. Until 2015 the installation was located in building 172 (Figure 1.1) close to the main CERN entrance.

The laboratory is of great importance for CERN since it is used for the regular calibration of all radiation protection monitors and personal dosimeters. About 800 portable instruments, 1500 operational dosimeters and 8000 passive dosimeters are calibrated every year at CERN. Moreover, the facility serves several users carrying out tests on accelerators instrumentation and prototypes, and is also used to test the response and characteristics of new instruments available on the market. All CERN RP monitors and dosimeters must be calibrated periodically to comply with the regulations of the Host States even though for the time being the laboratory is not accredited to provide official calibration certificates.

In 2010 the RP group was tasked to consider the technical constraints of the facility, its proximity to office spaces and site boundaries, changes to CERN's infrastructure and space management. From these considerations a consolidation plan was written and approved for the renewal of this facility. In order to meet the current and future needs of the Organisation, a number of different options were considered.

- Outsourcing the calibration of all instruments. The installation would not have been renewed and all instruments would have been sent to a pri-

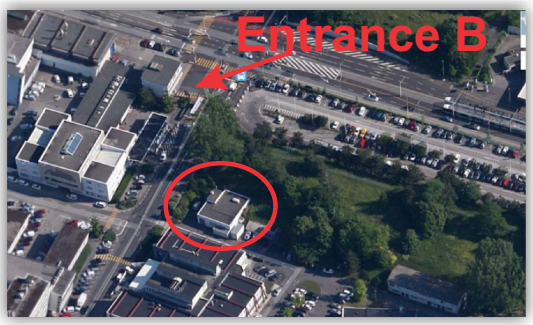

(a) *CERN main entrance*

(b) *Building 172*

Figure 1.1: *The building of the "old" calibration laboratory.*

mary/secondary standard calibration laboratory for their regular calibrations. The main drawbacks of this option were the time for having an instrument calibrated (from 4 to 10 weeks) and the loss for CERN of valuable technical expertise. The total cost of this option was estimated to be about 500 kCHF per year.

- Replacement of the calibration benches in building 172. The estimated cost of new instrumentation in building 172 was estimated to be about 700 kCHF. However, building 172 showed several signs of fatigue and an additional cost for its consolidation had to be taken into account.

- Installation of a new facility in an existing CERN building. The main problem was to find an existing building having adequate shielding walls and surface (minimum 200 m^2). This kind of building was not available.

- Building a new state-of-the-art facility. An adequate location could be found at CERN. The new facility will last for at least 15 years and could obtain the accreditation to provide official calibrations. The estimated cost was about 2.0 MCHF.

After a thorough evaluation and in order to meet Host States legal requirements, as well as CERN strict technical requirements, the decision was taken to build a new state-of-the-art calibration laboratory (Chapter 4).

The choice of the facility location took into account two main factors: a place sufficiently far away from CERN borders and highly populated buildings, and an area not influenced by external radiation sources, e.g. particle accelerators. Radiation measurements were carried out to validate the choice of the location before the beginning of the construction work (Section 4.1.1). The design of the facility

(Section 4.1.2), the selection of the radioactive sources (Section 4.1.3) and irradiators (Section 4.1.4) were mainly driven by the calibration needs and economic constraints. An approximate evaluation of the neutron scattering was performed by means of Monte Carlo (MC) calculations (Section 4.1.4) to define the set-up of the irradiators within the main calibration hall. The safety systems were defined in collaboration with the irradiator supplier and were optimized keeping them simple but effective (Section 4.1.5). The radiation protection studies performed with MC simulations optimized the shielding of the laboratory reducing the overall cost (Sections 4.2.2 and 4.2.3). The shielding calculations were then verified via measurements when all the sources were installed (Section 4.2.7). The safety of the laboratory for what concerns activation issues (Section 4.2.5) and ozone production (Section 4.2.6) was also studied via MC simulations. Further MC studies concerning the neutron scattering (Section 4.3) and the radiation field characterization contributed to commission the laboratory together with experimental measurements (Section 4.4).

1.1.2 CERF calibration facility

The RP group is also in charge of the CERN-EU high-energy Reference Field facility, CERF (Chapter 5). This is not a conventional calibration laboratory such as the calibration facility described in the previous section; it is a "field calibration" facility for radiation protection instrumentation that simulates the workplace field that can be encountered in the proximity of high-energy accelerators and at flight altitudes. Such a facility is unique in its kind and is usually operated for one week twice per year. Many users from all over the world come to CERF to test and calibrate active and passive dosimeters, rem-counters, spectrometers and prototype detectors. For the time being the facility is not officially accredited even though the scientific community is demanding this service. Within the framework of providing CERN with state-of-the-art calibration facilities to answer not only to its own needs but also to those of the international scientific community, a study was initiated to upgrade CERF; this work was also carried out with the aim of establishing a reliable facility that may ask to be officially accredited as workplace field.

First, a verification of the beam monitor calibration factor, on which all the measurements rely, was planned. The calibration was performed not only via the well-known ^{27}Al-foil activation technique, but also investigating a new activation reaction on ^{nat}Cu (Section 5.2). The calibrations and tests performed at CERF also rely on H*(10) reference values and spectra provided by MC simulations. They were calculated in the nineties with the 1997 version of the FLUKA code. Therefore, new simulations were carried out with the present development version of the code and upgraded values were provided. The latest were benchmarked with

recent neutron measurements (Section 5.3). Finally, the capabilities of CERF were also tested and extended to experimental measurements of high-energy spallation cross-sections (Section 5.4) on various elements.

1.2 Neutron calibration facilities

Neutron sources are used and neutron radiation fields are generated in various scientific research areas and applications, e.g. radiation therapy, radionuclide production for medical applications, material science studies, design of electronic components, energy production, military activities, and neutron radiography. In order to perform measurements of neutron fields, or for benchmark measurements of calculated fields, it is necessary to calibrate instruments in reference fields at energies from thermal up to about 1 GeV [1]. A reliable measurement of neutron radiation is a difficult task because of the wide energy range of neutrons, their complex and energy-dependent interaction mechanisms with matter and, consequently, the imperfect response characteristics of most instruments. Moreover, in any calibration facility neutrons scattered on floor, walls and support structures ("room scatter"), by air ("air scatter") and in the neutron source ("source scatter") may contribute significantly to the radiation field at a given position and thus influence the reading of an instrument to be calibrated (the neutron scattering topic is widely described in Section 4.3). Hence, calibration procedures and calibration facilities play a key role [2]. Different types of calibration fields have been developed and made available at several institutions:

- broad energy distributions produced by radionuclide sources;
- thermal and filtered neutron beams produced by reactors;
- nearly monoenergetic neutron fields produced with particle accelerators;
- simulated workplace fields with broad energy distributions similar to those observed in workplaces.

Ref. [3] indicates the main radionuclides that shall be used for neutron calibrations:

- Cf-252 (D_2O moderate);
- bare Cf-252;
- ^{241}Am-B (α,n);
- ^{241}Am-Be (α,n).

Preferably ^{241}Am-Be (from now-on Am-Be) and/or Cf-252 spontaneous fission sources should be used for routine calibration [3]. Cf-252 sources generally have high specific source strength and are therefore comparatively small. However, because of their half-life of 2.65 years, they need regular replacement. Am-Be has a half life of 432 years and is therefore suitable for routine calibrations. Their spectra are rather similar (fluence average energies are 2.13 MeV and 4.16 MeV for Cf-252 and Am-Be, respectively). Another important difference is the price since Cf-252 sources are much more expensive than Am-Be ones. The neutron energy distribution can be modified using a moderator around the sources. Ref. [3] recommends the use of a heavy water sphere 30 cm in diameter around the Cf-252 source to obtain an increase in the contribution of lower energy neutrons (fluence average energy of 0.55 MeV).

Research reactors were used earlier to produce reference neutron fields with the help of "filters". The production of quasi-monoenergetic neutron radiation makes use of the existence of deep relative minimima in the total cross-sections of certain materials at distinct energies (2, 24 and 144 keV).

Accelerators are generally used to produce monoenergetic or quasi-monoenergetic neutrons. An accelerator providing protons and deuterons up to an energy of 3.5 MeV is required to generate neutrons with energies between 2 keV and 19 MeV. It should be noted that care must be taken to account for scattered neutrons. Higher energy neutrons up to at least 200 MeV can be produced with protons on thin targets of low-Z material such as Li and Be. The spectral distribution shows a high-energy peak resulting from transitions populating the ground state and first excited states of the residuals nucleus and continuum caused by break-up reactions and interactions of the neutrons with the collimators.

Owing to the generally strong energy dependence of radiation protection devices, attempts were made to produce well-characterised neutron fields with energy distributions similar to those at typical workplaces. A first group of calibration fields tries to simulate workplace fields in nuclear industry, which consist of: a high-energy component representing the uncollided neutrons, a scattered component with an approximately $1/E_n$ dependence (where E_n is the neutron energy), and a thermal-neutron component. A second group are radiation environments containing neutrons with energies greater than 10 MeV, contributing 30% to 50% to the ambient dose equivalent and personal dose equivalent; those are located in the vicinity of high-energy particle accelerators and in aircrafts flying at altitudes of 10 km to 15 km. The calibration of neutron dosimeters and survey meters by means of radioactive sources can result in an inaccurate estimate of the ambient dose equivalent when such devices are used in neutron fields markedly different from the ones of the sources [4]. Therefore, the establishment of simulated workplace neutron spectra in a calibration laboratory is necessary. Unfortunately these

facilities are rather scarce and the CERF field at CERN (widely described in Chapter 5) is the only one capable to simulate the high-energy radiation field typical of high-energy accelerators and similar to those encountered at flight altitudes.

1.3 Gamma calibration facilities

Four groups of reference radiation exist for calibrating protection-level dosimeters and doserate meters at air kerma rates from 10 μGy/h to 10 Gy/h and for determining their response as a function of photon energy:

- in the energy range from about 7 keV to 250 keV, continuous filtered X radiation and the gamma radiation of Am-241;
- in the energy range 8 keV to 100 keV, fluorescence X radiation;
- in the energy range 600 keV to 1.3 MeV, gamma radiation emitted by radionuclides;
- in the energy range 4 MeV to 9 MeV, gamma radiation produced by reactors and accelerators.

The characteristics of the X radiation are not exploited in this work, even though the laboratory is provided with an X-ray generator. The characterization and commissioning of this irradiator will be the scope of a future work. Concerning the energy range between 600 keV and 1.3 MeV, ref. [5] recommends to use the following sources to calibrate dosimeters and rate dosimeters: Co-60 (two energy lines at 1.173 and 1.333 MeV, respectively), Cs-137 (662 keV) and Am-241 (60 keV). The air-kerma rate due to the principal radioactive impurity shall be less than 1% of the air-kerma rate due to the radiation of the isotope to be utilized. The secondary standard ionization chamber (Section 3.2) used for all measurements shall be of adequate sensitivity. Its variation in response per unit air kerma as a function of the energy and direction of radiation should be small and known for the energy range in question. Moreover, the air-kerma rate due to radiation scattered by the environment shall not exceed 5% of that due to direct radiation. Detailed information about scattered photons is only accessible through an investigation of spectra by performing MC simulations. However, the 5% contribution can be avoided by implementing one of the two geometries here described [5].

- Uncollimated geometry installation: the source should be used in a room with a size of at least 4 m x 4 m x 3 m high. The source and detector should be used on supports, which have very low content of low-atomic number materials. They should be positioned at half height of the room .

- Collimated geometry installation: a collimator shall be employed to define the shape and size for the photon beam. The beam cross-section shall be larger than that of the detectors to be irradiated. The distance between the detector and the collimator should be greater than or equal to 30 cm.

The air-kerma rates shall be measured on the axis of the beam at the various points of test. After correcting for air attenuation, the air-kerma rates shall be proportional within 5% to the inverse square of the distance from the source centre to the detector centre [5].

Chapter 2

The Monte Carlo method

2.1 Monte Carlo method for particle transport

2.1.1 History of the Monte Carlo method

The Monte Carlo (MC) method is a technique of numerical analysis that is based on the use of sequences of random numbers to obtain sample values for the problem variables. The calculation process used in MC is an artificial construct, usually a computer program that is mathematically equivalent to the problem being analysed [6]. The individual numbers are sampled from valid representative collections of input data; they are some sort of a frequency distribution that is converted to a probability distribution. The desired solution of the problem can be obtained along with estimates of the associated uncertainties. Ref. [6] says that: "The sample evaluation in a Monte Carlo calculation is somewhat equivalent to conducting and experiment". Actually, both a MC calculation and an experiment will produce a result that is a possible outcome of the process under study, and both contain uncertainties that can often be reduced by repeating the measurements and estimated by means of statistical analysis.

Credit for inventing the MC method often goes to Stanislaw Ulam, a Polish born mathematician who worked for John von Neumann on the United States' Manhattan Project during World War II. Although Ulam is known for having designing the hydrogen bomb in 1951, he also invented the MC method in 1946 while pondering the probabilities of winning a card game of solitaire. Initially he tried to solve this problem with pure combinatorial calculations, but then he thought that playing multiple hands of solitaire and observe the frequency of wins would have been much more effective [7]. However, the real use of MC methods as research tool comes from a work on the atomic bomb. This work involved a direct simulation of the probabilistic problems concerned with random neutron diffusion in fissile material; nevertheless, at an early stage of these investigations, von Neumann and

Table 2.1: *Integration efficiency of the MC method compared to traditional numerical integration methods (e.g. Simpson's rule). n = number of dimensions, N = number of "points" (interval).*

n	Traditional methods	Monte Carlo	Remark
1	1/N	$1/\sqrt{N}$	MC not convenient
2	$1/\sqrt{N}$	$1/\sqrt{N}$	About equivalent
>2	$1/^{n}\sqrt{N}$	$1/\sqrt{N}$	MC converges faster

Ulam refined this direct simulation with certain variance-reducing techniques, in particular "Russian roulette" and "splitting" methods. The possibility of applying MC methods to deterministic problems was discovered by Fermi, von Neumann and Ulam and popularized by them in the immediate post-war years [8].

MC is now used routinely in many different fields, from the simulation of complex physical phenomena such as radiation transport in the earth atmosphere to the simulation of the esoteric sub-nuclear processes in high-energy physics experiments. Its name does not mean to imply that the method is either a "gamble" or a "risky" but simply refers to the manner in which individual numbers are sampled from valid frequency distributions.

2.1.2 Particle transport Monte Carlo

MC can be defined in several possible ways: a mathematical method for numerical integration or a computer simulation of a physical process. Both definitions are valid and, depending on the problem, one or the other can be more effective. Originally, the MC method was not a simulation method but a device to solve a multidimensional integro-differential equation by building a stochastic process such that some parameters of the resulting distributions would satisfy that equation. The equation itself did not necessarily refer to a physical process, and if it did, that process was not necessarily stochastic. The integration efficiency of the MC method is described in Table 2.1. For number of dimensions greater than two, MC converges faster; it is worth noting that a typical particle transport MC problem is a 7-D problem (position: x, y, z; momentum: p_x, p_y, p_z; time: t).

All particle transport calculations aim to solve the Boltzmann equation, which can be seen as a balance equation in phase space: at any phase-space-point, the increment of particle phase-space-density is equal to the sum of all "production terms" minus a sum of all "destruction terms". For instance, the following can be considered as production terms: sources, "in-scattering", particle production

and decay. Destruction terms are often absorption, "out-scattering" and decay. Solutions of different type can be explored: at a number of (real or phase) space points, averages over (real or phase) space regions, projected on selected phase space hyper-planes, stationary or time-dependent. Before the calculation can begin, the user must define the problem (e.g. source, geometry); once the problem is defined, the random walk of the particles through the problem geometry can be executed. The basic set of steps consists of the following [6].

1. Problem geometry definition: the geometry and material constituents of the problem shall be defined since the particle interactions are based on this description.

2. Source term: its definition is essential to initiate the random walk procedure (e.g. a neutron with a specific position, energy, time and direction of travel).

3. Random sampling of the outcome of physical events according to an appropriate probability distribution.

4. All the secondaries from the same primary are transported before a new history is started

5. Computation of the response: the results of the random walk are used to calculated the quantity of interest and its statistical uncertainty.

As already underlined, random numbers, i.e. values of a variable distributed according to a probability distribution function, are the basis for all MC integration. In the real world one can consider the random outcome of a physical process, e.g. the radioactive decay, in the computer world pseudo-random numbers are used; they are sequences that reproduce the uniform distribution, constructed from mathematical algorithms. The main assumptions of the particle transport MC that allow the superposition principle to be used are:

- static, homogeneous, isotropic and amorphous media (and geometry);
- Markovian process: the fate of a particle depends only on its actual properties, not on previous events or histories;
- particles do not interact with each other;
- particles interact with individual atoms/nuclei/molecules (invalid at low energies);
- material properties are not affected by particle reactions.

The accuracy and reliability of a MC code depends on the models or data on which the probability distribution functions are based. Instead, the statistical precision of the results depends on the number of histories and its convergence can be accelerated by "biasing" techniques.

In particle transport it is fundamental to define the mean free path, λ *[cm]*, i.e. the average distance travelled by a particle in a material before an interaction. The macroscopic cross section, Σ, is its inverse (Eq. 2.1) and is the probability of interaction per unit distance. Both λ and Σ depend on the material and on the particle type and energy.

$$\Sigma = \frac{1}{\lambda} \tag{2.1}$$

For N identical particles, the number of reactions R occurring in a given time interval will be described by Eq. 2.2:

$$R = N \cdot l \cdot \Sigma \tag{2.2}$$

where $N{\cdot}l$ is the total distance travelled by the particles. The reaction rate, $\dot{R}$ will be therefore:

$$\dot{R} = N \cdot \frac{dl}{dt} \cdot \Sigma = N \cdot v \cdot \Sigma \tag{2.3}$$

where v is the average particle velocity. If $n(\vec{r},v)$ in Eq. 2.4 is the density of particles with velocity v at a spatial position $\vec{r}$, then the reaction rate, $d\dot{R}$, inside the volume element dV will be given by Eq. 2.5.

$$n(\vec{r}, v) = \frac{dN}{dV}[cm^{-3}] \tag{2.4}$$

$$\frac{d\dot{R}}{dV} = n(\vec{r}, v) \cdot v \cdot \Sigma \tag{2.5}$$

The quantity $\dot{\Phi} = n(\vec{r}, v)v$ is called fluence rate or flux density and has dimensions of [cm^{-2} s^{-1}]. The time integration of the fluence rate gives the fluence (Eq.2.6), Φ, which describes the density of particle tracks.

$$\Phi(\vec{r}, v) = n(\vec{r}, v) \cdot dl[cm^{-2}] \tag{2.6}$$

The physical meaning of fluence is related to the fact that the number of particle interactions is proportional to the total distance travelled by the particles.

2.1.3 Features of Monte Carlo neutron simulations

The transport of neutrons can be performed in two ways depending on the particle energy. For neutron energies up to 20 MeV evaluated data files based on expert "evaluations" of available experimental data can be used; it should be noted that there are no real alternative below 20 MeV. They can be accessed by standard formats/processing tools. An advantage is that they need little CPU time but are rather "memory consuming". Unfortunately this approach shows some drawbacks: no correlations, the update when new data are available is slow and complex, sometimes these libraries are incomplete or inconsistent. Evaluated nuclear data files typically provide neutron cross-sections and secondary particles inclusive distributions for energies below 20 MeV for all channels. Recent evaluations include data up to 150/200 MeV for a few isotopes. For energies above 20 MeV up to TeV's MC nuclear models aim at the description of particle production spectra by whichever projectile. A large variety of models is available but not necessarily are all good. However, they produce fully correlated physical events (e.g. the conservation laws are fulfilled) and are easy to update. These models are as good as the physics inside, which sometimes is good for most of the applications, and cannot really be used below 10-20 MeV.

In neutron transport codes in general two approaches are used: point-wise (continuous cross-sections) and group-wise transport. Point-wise transport follows cross-section precisely but it can be time and memory consuming. Instead, the group approach is widely used in neutron transport codes because it is fast and gives good results for most application (e.g. shielding, reactor criticality) and it is suitable for discrete ordinates codes and adjoint calculations.

2.2 Monte Carlo codes for particle transport

The main MC codes used for particle transport are listed in this section together with their main features. The list is not exhaustive and detailed code descriptions can be found in the respective manuals. It is worth noting that all the listed code are almost equivalent for the MC studies performed for the calibration facility (Sections 4.2 and 4.3), except for the residual radioactivity calculations where FLUKA shows to be the more suitable for its great capabilities. For the CERF study the physical models employed/chosen in the codes can produce significant differences; however, FLUKA was chosen since already benchmarked in the CERF radiation field. For this work, another advantage of FLUKA was that, being developed at CERN, a quick support was always available during the several MC studies performed.

2.2.1 GEANT4 [9, 10]

GEANT4 is an object-oriented toolkit (written in C++) for simulating the transport of particles through matter. It has been used in applications in particle physics, nuclear physics, accelerator design, space engineering and medical physics. Its functionalities include tracking, geometry description, material specifications, management of events and interfaces to external graphics systems. The system also provides interfaces to models for physics processes. The flexibility of GEANT4 is unique since the user can freely select the physics models that best fit the particular application needs [11]. GEANT4 can simulate the transport of 68 particle types and for low-energy neutrons it uses a point-wise approach. Furthermore, heavy-ion interactions can also be simulated linking the appropriate packages. To facilitate the use of variance reduction techniques, general-purpose biasing methods such as importance biasing, weight windows, and a weight cut-off method have been introduced directly into the toolkit. Other variance reduction methods, such as leading particle biasing for hadronic processes, come with the respective physics packages [11].

2.2.2 MCNPX [12]

MCNPX stands for Monte Carlo N-Particle eXtended and originates from the Monte Carlo N-Partilce transport (MCNP) family of neutron interaction and transport codes. The code is written in Fortran90/C. The area of application covers neutronics-related to accelerator shielding design, medical physics, space radiation, nuclear safeguards, homeland security, nuclear criticality and much more. The neutron interaction and transport modules use standard evaluated data files mixed with physics models where such libraries are not available. The transport includes all features necessary for reactor simulations, e.g. burn-up, transmutation. The code transports 34 particle types. Concerning variance reduction techniques, the spherical mesh weight windows can be created by a generator in order to focus the simulation time on specific spatial region of interest [11]

2.2.3 PHITS [13]

PHITS (Particle and Heavy Ion Transport code System) is a MC code, written in Fortran 95/C, developed under collaboration between JAEA, RIST, KEK and several other institutes. It transports 38 particle types. The transport of low-energy neutrons employs cross-sections from evaluated data files (ENDF and JENDL below 20 MeV and LA150 up to 150 MeV). Several variance reduction techniques are available in PHITS, such as weight windows and region importance biasing. It is especially used in the fields of accelerator technology, radiotherapy

and space radiation.

2.2.4 FLUKA [14, 15]

FLUKA (FLUktuierende KAskade) is a general-purpose particle interaction and transport code with origin in radiation protection studies at high energy accelerators; it includes all features needed in this field of application (e.g. detailed hadronic and nuclear interaction models). It is written in Fortran 77. The module for hadronic interactions is called PEANUT and consists of: a phenomenological description (Dual Parton Model-based Glauber Gribov cascade) of high energy interactions (up to 20 TeV); a generalized intranuclear cascade; and pre-equilibrium emission models as well as models for evaporation, fragmentation, fission and de-excitation by gamma emission. Neutrons with energy below 20 MeV are transported with a multi-group approach based on evaluated cross-section data binned into 260 energy groups, 31 of which in the thermal energy region. Point-wise cross-sections can be optionally used for certain isotopes (H-1, Li-6, B-10 and N-14). Many variance reduction techniques are available in FLUKA. The capabilities of FLUKA are unique for studies of induced radioactivity especially with regard to nuclide production, decay, and transport of residual radiation. In particular, particle cascades by prompt and residual radiation are simulated in parallel based on the microscopic models for nuclide production and a solution of the Bateman equations for activity build-up and decay [11].

Chapter 3

Instrumentation

This chapter describes the instrumentation, together with its working principle, used for the radiation measurements perfomed in this work:

- neutron background measurements at the calibration laboratory location (Section 4.1.1) and neutron measurements at the CERF facility (Section 5.3.3): WENDI-2;
- neutron radiation protection measurements around the calibration facility (Section 4.2.7): LB6411;
- characterization of the neutron field of the calibration laboratory (Section 4.4.1: SmartREM;
- characterization of the photon field of the calibration laboratory (Sections 4.4.2 and 4.4.3) and monitoring of the CERF beam (Section 5.2): air-filled ionization chambers.

3.1 Rem-counters

Neutrons have not electric charge and therefore they do not directly ionize the matter but are detected through the products of the reactions that they may generate. Among the reactions for detecting neutrons, the following are commonly employed in rem-counters.

1. ^{10}B(n,α)^{7}Li. The Q-value, i.e. the amount of energy released by the reaction, is 2.79 MeV and causes the emission of sufficiently energetic charged hadrons, also with thermal neutrons. The reaction cross-section at thermal neutron energies is 3837 barn. B-10 constitutes about 20% of the natural Boron but can be enriched up to 95%; Boron is used as gas in form of BF_3.

2. $^{3}He(n,p)^{3}H$. The main disadvantage of the He-3 gas is that it is scarce in nature (it is a product of the natural tritium decay) and it is very difficult to be produced. The Q-value is 764 keV and the cross-section for thermal neutrons is about 5400 barns.

The three detectors used to perform the measurements of this work are the WENDI-2, the SmartREM and the LB6411. They use He-3 as filling gas. This detection system is the one employed by the proportional counters since the collected charge is proportional to the primary ionization via a multiplication factor $M>1$. The electrons generated by the primary ionization drift toward the central anode, to which a positive voltage is applied; in proximity of the central anode the multiplication process occurs. The internal multiplication allows high impulses to be produced even though the deposited energy is small, i.e a few keV. Neutron radiation is usually accompanied by a gamma contribution, which must be subtracted from the reading. The neutron/gamma discrimination is performed by setting a voltage threshold that accept/reject the incoming signal; this allows the gamma signal, whose amplitude is smaller than the neutron one, to be discarded.

The inherently low-detection efficiency for fast neutrons of any slow neutron detector can be improved by surrounding the detector with a few centimetres of hydrogen-containing moderating material. The incident fast neutron then loses a fraction of its initial kinetic energy in the moderator before reaching the detector as a lower-energy neutron, for which the detector efficiency is generally higher. However, the probability that an incident fast neutron ever reaches the detector will decrease as the moderator is made thicker. By carefully choosing the diameter and composition of the moderator-detector system, its overall efficiency versus energy curve can often be shaped and tailored to suit a specific application [16]. This is the case of a rem-counter, the aim of which is measuring the neutron ambient dose equivalent, H*(10). Rem-counter response per unit of fluence must approximate the fluence-to-dose conversion function indicated by ref. [17].

3.1.1 WENDI-2

The WENDI-2 (Wide Energy Neutron Detection Instrument, Figure 3.1) is an extended range neutron rem-counter of the Anderson-Braun (A-B) type, i.e. a neutron rem-counter with a cylindrical polyethylene moderator employing a cylindrical BF_3 or He-3 tube. Its response per unit fluence approximates an appropriate fluence-to-dose conversion function. For classical A-B type rem meters this range usually starts at thermal energies going up to approximately 10 MeV. At higher energies the moderator shell does not moderate anymore the neutron field appropriately to lower neutron energies. Since in the proximity of large accelerators, e.g. at the CERF facility (Chapter 5), much higher neutron energies than 10 MeV

Table 3.1: *WENDI-2 technical specification [20].*

Diameter	32 cm
Height	23.0 cm
Weight	13.5 kg
Energy range	25 meV to 5 GeV
Measuring range	0.01 μSv/h to 100 mSv/h for Cf-252
Neutron sensitivity	0.84 cps/(μSv/h) for Cf-252
Gamma sensitivity	1 to 5 μSv/h at 100 mSv/h of Cs-137

are encountered, extended range neutron rem-counters were developed. The moderator shell of the WENDI-2 is made of polyethylene, which includes a layer of tungsten powder with a density of 10.71 g/cm^3. The tungsten extends the range of the detector to higher energies, since high energetic neutrons interacting with the tungsten layer produce neutrons of lower energies via spallation reactions [18]. The proportional counter tube is a cylindrical He-3 neutron detector. This proportional counter has its working point at a voltage of approximately 1200 volts and is filled with 2 bar of He-3, which is surrounded by a stainless steel shell of 0.5 mm thickness. On top of the rem counter there is a borated rubber patch which covers the opening for insertion of the counter tube during the manufacturing process. This is also where the cable for signal and high voltage is fed through. The signals coming from the counter tube are amplified and discriminated by the FHT-642 preamplifier and then passed on to the FH40G dose rate measuring unit. The FH40G includes a proportional counter tube for gamma measurements, an LCD display to show dose rates in real time and a serial infrared connection to transmit the data to a computer. The preamplifier FHT-642 introduces an energy threshold of 50 keV of deposited energy in the active volume of the detector, which means that only events that are depositing more than 50 keV of energy inside the counter tube are producing a count. The threshold is introduced to make the detector insensitive for photons which are depositing energy mainly in this low energy region. Table 3.1 lists the specification of the WENDI-2. Figure 3.2 shows the WENDI-2 response function as calculated in ref. [19] together with the ICRP74 fluence-to-ambient-dose-equivalent conversion coefficients [17]. The WENDI-2 overestimates the H*(10) at energies between few eV and 0.1 MeV and above 100 MeV.

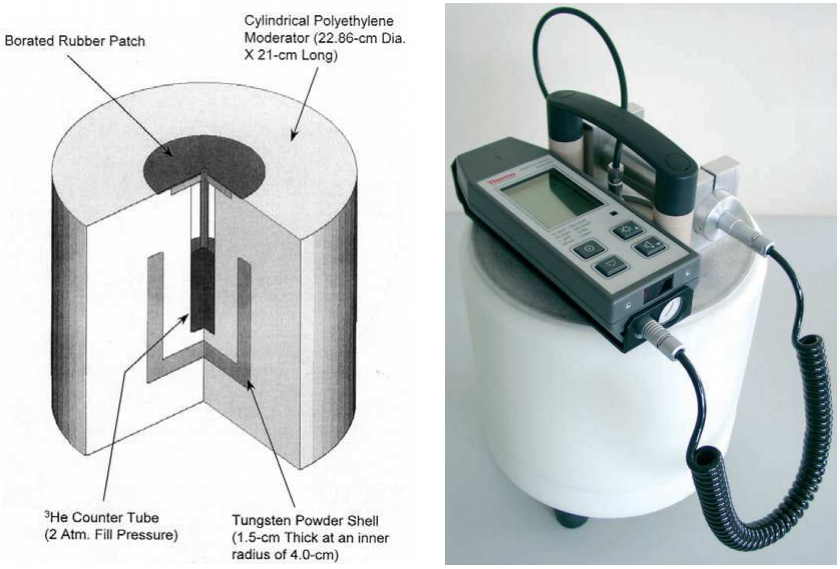

(a) *Cross-sectional view* (b) *WENDI-2*

Figure 3.1: *The WENDI-2 extended range rem-counter [21].*

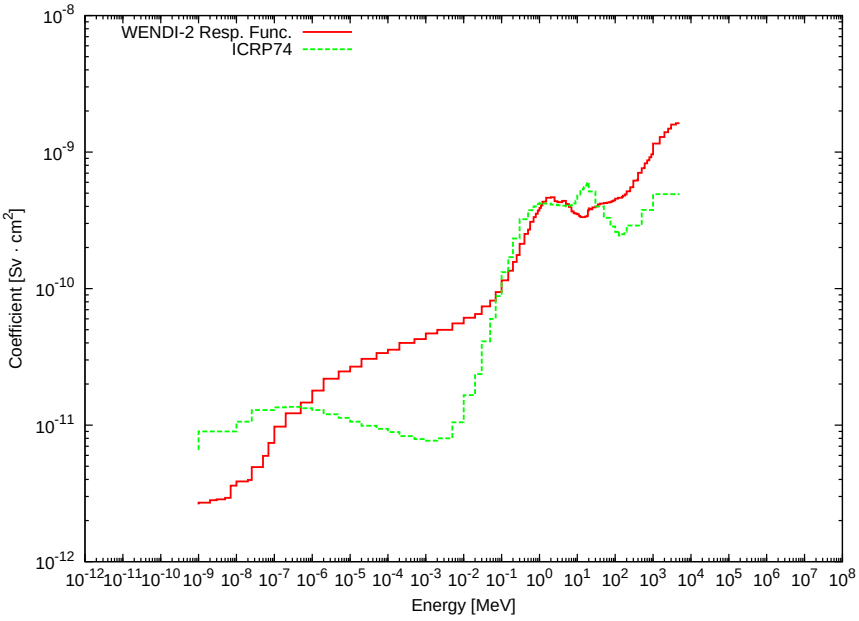

Figure 3.2: *Plot of the WENDI-2 response function [19] and the ICRP74 fluence-to-ambient-dose-equivalent conversion coefficients [17].*

Figure 3.3: *The LB6411 rem-counter [22].*

Table 3.2: *LB6411 technical specification [22].*

Diameter	25.0 cm
Weight	9.2 kg
Energy range	Thermal to 20 MeV
Measuring range	30 nSv/h to 100 mSv/h
Neutron sensitivity	0.79 cps/(μSv/h) for Cf-252
Gamma sensitivity	<40 μSv/h to 10 mSv/h of Cs-137
Fluence response	1.09 cm^2 for Cf-252

3.1.2 LB6411

The LB6411 rem-counter (Figure 3.3) consists of a polyethyene moderator sphere with a diameter of 25 cm, a central cylindrical He-3 proportional counter and internal Cd-absorbers and perforations. The instrument has an integrated high-voltage supply and signal processing and is connected to a microprocessor-controlled portable datalogger. Table 3.2 lists the specification of the LB6411. The LB6411 is not an extended range rem-counter as the WENDI-2 as can be observed from its response function (Figure 3.4); it is generally used in radiation environment where high energy neutrons are not expected and is well-suited for RP monitoring.

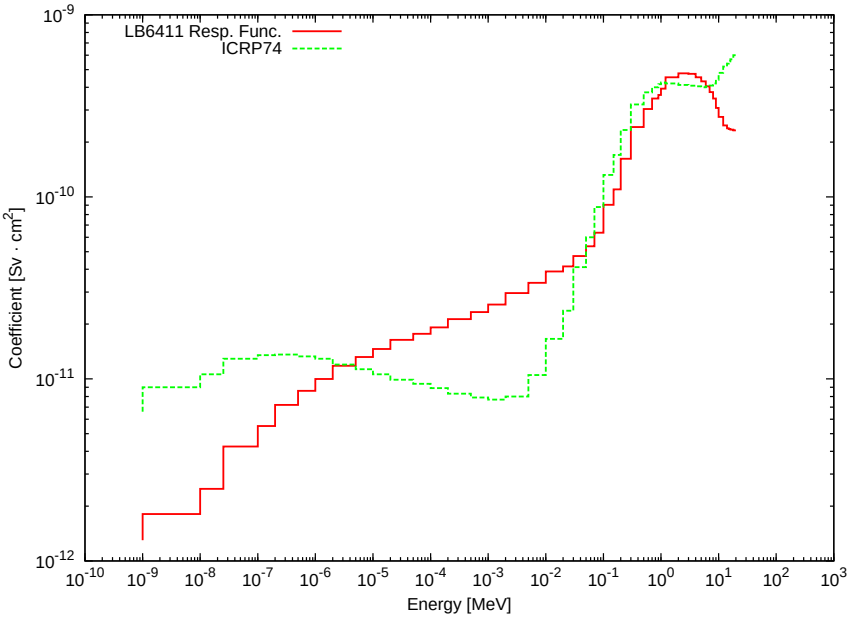

Figure 3.4: *Plot of the LB6411 response function [23] and the ICRP74 fluence-to-ambient-dose-equivalent conversion coefficients [17].*

3.1.3 SmartREM

The SmartREM rem-counter (Figure 3.5) consists of a boron loaded polyethylene moderator sphere with a diameter of 20.8 cm and a central spherical He-3 proportional counter [24]. The instrument has an integrated high-voltage supply and a multi-channel analyser with 2048 channels. The measured values can be stored on a MicroSD card. Table 3.3 lists the specification of the SmartREM. Unlike the WENDI-2, the SmartREM is not an extended range rem-counter as can be observed from its response function, which does not extend to high energies. The SmartREM is generally employed in radiation environment where high energy neutrons are not expected and is well-suited as secondary standard device for calibration facilities, employing radioactive neutron sources such as Cf-252 and/or ^{241}Am-Be.

3.2 Ionization chambers

Ionization chambers are the simplest of all gas-filled detectors. Their normal operation is based on collection of all the charges created by direct particle ionization within the gas through the application of an electric field. If a fast charged particle passes through a gas, a neutral molecule can be ionized; the resulting

Figure 3.5: *The SmartREM rem-counter [25].*

Table 3.3: *SmartREM technical specification [25].*

Diameter	20.8 cm
Weight	6.5 kg
Energy range	Thermal to 14 MeV
Neutron sensitivity	0.74 cps/(μSv/h) at 1 MeV

positive ion and free electron are called an ion pair and it serves as the basic constituent of the electrical signal of the ionization chamber. The quantity of interest is the total number of ion pairs created along the tracks of the radiation. In order to initiate the ionization process, the particle must transfer at least an amount of energy equal to the ionization energy of the gas molecule. However, the particle may lose its energy in non-ionizing ways, e.g. excitation process in which an electron may be elevated to a higher bound state in the molecule without being completely removed. The average energy lost by incident particle per ion pair formed, the so-called *W-value*, is always greater than the ionization energy (for air the W-Value is about 33.8 eV per ion pair for fast electrons). Assuming that W is constant for a given type of radiation, the deposited energy will be proportional to the number of ion pairs formed and is evaluated if the number of ion pairs can be measured. Several mechanisms may happen after the formation of the ion pair, that prevent the complete charge collection:

- charge transfer collisions: a positive ion encounters another neutral gas molecule and an electron of the neutral molecule is transferred to the ion, reversing the respective charges;
- electron attachment: a free electron may contribute to form a negative ion

by joining a neutral gas molecule (e.g. Oxygen readily attaches electrons);

- recombination: if a positive ion and a free electron collide, the electron may be captured by the positive ion and returns it in a neutral charge state;
- diffusion: the free electrons, as well as the positive ions, take part in the random thermal motion and diffuse away from high density regions.

No net current should flow in the absence of an applied voltage because there is no electric field within the gas; the ions and electrons disappear either by recombination or by diffusion from the active volume. As the voltage is increased, the resulting electric field starts to separate the ion pairs more rapidly and the recombination is diminished. The measured current increases with the applied voltage, which reduces the amount of the original charge that is lost. At a sufficiently high voltage, the electric field is large enough to suppress recombination, and all the original charges created are collected. This is the region of ion saturation, in which the ion chambers are conventionally operated. The presence of an electric field causes the drift of the positive and negative charges (ions and electrons) and the generation of an electric current. If a given volume of gas is undergoing steady-state irradiation, the rate of formation of ion pairs is constant. Therefore, if the recombination is negligible, i.e. the intensity of the electric field is enough and all the charges are efficiently collected, the steady-state current produced is an accurate measure of the rate at which ion pairs are formed within the volume.

Air is the most common fill gas for ionization chambers and is one in which negative ions are readily formed. Air is required in those chambers designed for measurement of gamma-ray exposure. Some sort of supporting insulator must be provided between the two electrodes. Because typical ionization currents in most applications are extremely low (in the order of 10^{-12} A or less), the leakage current through these insulators must be kept very small. In order to reduce the effect of insulator leakage, guard ring is often employed.

Since the magnitude of the ionization current under typical conditions is too small to be measured using standard galvanometer techniques, an active amplification of the current must be performed. An electrometer indirectly measures the current by sensing the voltage drop across a series resistance placed in the measuring circuit. The voltage developed across the resistor can be amplified and serves as the basis for the measured signal. Since any small drift results in a corresponding change in the measured output current, circuits of this type must frequently be balanced by shorting the input and resetting the scale to zero.

One of the most important applications of ion chambers is the measurement of gamma-ray exposures. Since the exposure is defined in terms of the amount of the ionization charge created in air, air-filled ionization chambers are the ideal instruments for this porpuse. To measure the exposure, one would theoretically

need to follow each of the secondary electrons over its entire range, i.e. several metres, and measure all the ionization created along its track. Since designing such an instrument would be difficult, the principle of compensation is used. If the test volume of air is surrounded by an infinite sea of equivalent air that is also subject to the same exposure during the measurement, an exact compensation will occur. In other word, all the ionization charges created outside the test volume from secondary electrons that were formed within the volume is exactly balanced by charge created within the test volume from secondary electrons formed in the surrounding air. Gamma-ray exposure measurements at energies higher than 150 keV are carried out in cavity chambers, in which a small volume of air is surrounded by a solid *air-equivalent* material, which acts as a compensator to the test volume. For an air-equivalent ion chamber, the exposure rate R in C/kg·s is given by Eq. 3.1:

$$R = \frac{I_s}{M} \tag{3.1}$$

where I_s is the saturated ionization current and M is the mass of the gas contained in the active volume, which depends on the volume, temperature and pressure of the chamber. The ion chambers can also be used indirectly to measure the absorbed dose D; the technique is based on the application of the Bragg-Gray principle, which states that the absorbed dose in a given material is obtained from the ionization produced in a small gas-filled cavity within that material (Eq. 3.2):

$$D = WS_mP \tag{3.2}$$

where W is the average energy loss per ion pair formed in the gas, S_m the relative mass stopping power of the material to that of the gas and P is the number of ion pairs per unit mass formed in the gas. If the gas is air and the wall is air-equivalent, the factor S_m is unity [16].

Chapter 4

Design and commissioning of the new CERN RP calibration facility

This chapter describes the design and commissioning of the new RP calibration facility; it highlights the key-points of the design and construction phases of the laboratory. It also reports the radiation measurements carried out to commission the facility. Before entering into details, one should take into consideration some essential aspects of the project.

- Providing CERN with a state-of-the-art RP calibration facility: the new facility was conceived to replace the previous ageing facility (see also Section 1.1) and to set up a new high-standard and reliable service at CERN for the calibration of dosimeters, environmental detectors as well as all radiation monitoring devices. The facility is also aimed at carrying out research on prototype detectors and new radiation monitors available on the market.

- Innovation to answer the needs of the scientific community: the laboratory is not only a standard calibration facility, but has innovative features, such as the possibility to perform simultaneous neutron/gamma irradiation (Sections 4.1.2 and 4.1.4) and a dedicated irradiation room for studying and qualifying electronic components and systems (Sections 4.1.2, 4.1.4 and 4.4.3).

- Optimization of building design and radiation protection aspects (Sections 4.1.4 and 4.2): several building design options were studied to obtain the best compromise among economic constraints, radiation protection requirements and calibration needs. In addition, a dedicated study was performed to choose a facility location not influenced by other radiation sources (Section 4.1.1).

- Safety system implementation (Section 4.1.5): because of the presence of radioactive sources (Section 4.1.3), the safety systems were accurately defined

to meet CERN safety standards in collaboration with the irradiator commercial supplier to ensure the radiation protection and safety; redundancy was applied to improve the safe operation of the entire complex.

4.1 General description of the facility

This section describes the main features and innovative aspects of the facility, the radioactive sources and the irradiators that were installed. It covers as well the measurements carried out to choose the most suitable location for the laboratory and the MC simulations performed to define the best irradiator set-up in the calibration hall.

4.1.1 Facility location and neutron background measurements

The criteria to establish the proper location for a new RP calibration facility were defined and studied taking also into account CERN specificities that are here described. In order to decrease the overall cost due to the shielding constraints and improve radiation protection, the facility should be located sufficiently far away from populated buildings. In addition, according to CERN agreements with the Host States (France and Switzerland), the ambient dose equivalent rate, H*(10), caused by CERN activities outside its borders must be below 300 μSv/year [26]; therefore, placing the facility away from CERN fences contributed to respecting this limit. Another constraint is that a RP calibration facility should be located in a place not being influenced by other radiation sources, e.g. particle accelerators.

After having considered several options, a suitable site complying with the first two criteria was found on the CERN Prévessin site. Since this location was close to the extraction line of the 400 GeV/c Super Proton Synchrotron (SPS) and its experimental areas (Figure 4.1), the third criterion had to be verified. It is known that the main secondary radiation at hadron accelerators is the neutron field; this is generated by the interaction of the beam particles with the accelerator components [27], beam line collimators, targets, and beam dumps. Neutron background measurements were performed to evaluate the possible influence that the SPS extraction lines would have on the radiation field in the area of the laboratory [28].

These measurements were carried out with the WENDI-2 neutron rem-counter (for the detailed description see Section 3.1.1). The neutron H*(10) was assessed during the following two beam conditions:

1. SPS extracting 400 GeV/c protons to an underground target area (the reference targets are called T2, T4 and T6);

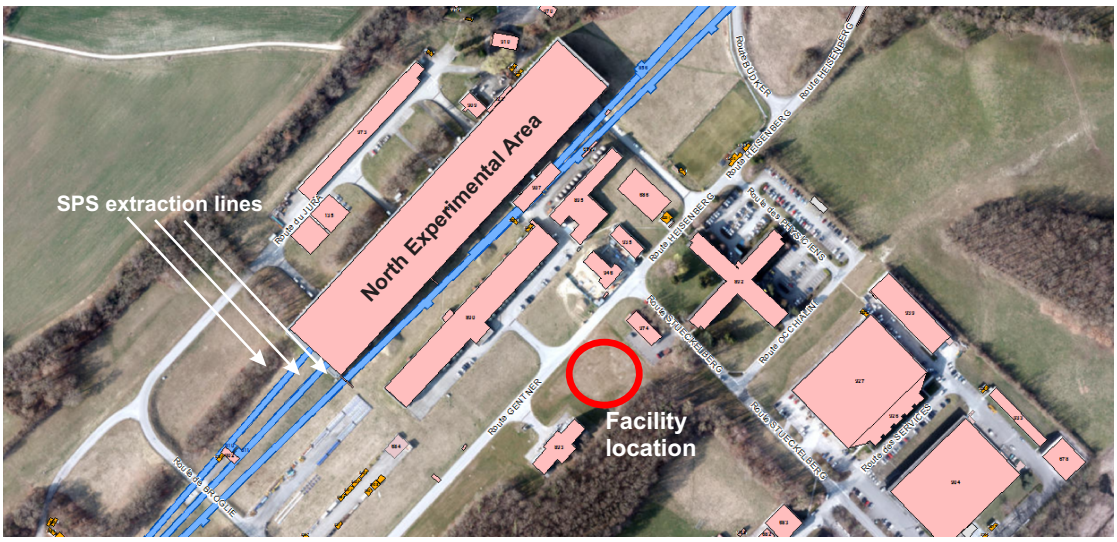

Figure 4.1: *The area dedicated to the RP calibration facility in the Prévessin site. The light blue lines correspond to the extraction lines of the SPS accelerator.*

2. SPS accelerating lead ions with a momentum below 100 GeV/c per nucleon to the same above-mentioned target area.

These two situations represented the possible SPS beam configurations. Normally, one does not expect a noticeable influence on the natural neutron background from accelerating lead ions if compared with a proton beam. However, this condition was taken into account to provide a complete data-set. The values were compared with the natural background, which was measured in May 2013 during the Long Shutdown 1 of the CERN accelerator complex, when all the CERN accelerators were turned off.

Assessing the neutron H*(10), especially at hundreds metres from the beam lines, implies distinguishing between the neutron background and the accelerator induced neutron radiation; therefore, dose rates with an accuracy in the nSv/h range have to be measured. This can only be achieved by performing long time measurements with detectors also reliable at very high neutron energies, i.e. up to GeV range, and accurately correlating the neutron H*(10) with the beam time and intensity.

The WENDI-2 was connected to a portable computer to register the count rates. The entire system was placed inside a car in order to protect it from bad weather conditions and the computer was kept plugged to the electric network supply to guarantee long time measurements, i.e. good statistics. The beam intensity was monitored via the TIMBER software (Figure 4.2), which provides information and parameters for each CERN beam and target position.

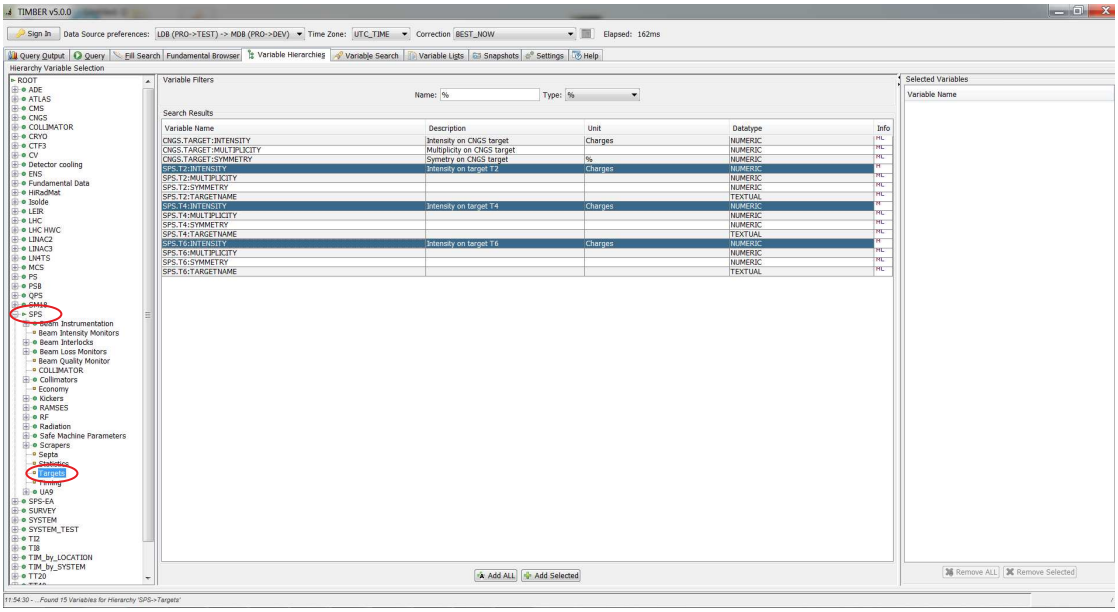

Figure 4.2: *A screen-shot of the TIMBER interface. In the red circles the chosen parameters and in the blue lines the reference variables for the measurements (in this case, the intensity on the T2, T4 and T6 targets).*

Figure 4.3 shows an example of the correlation between the neutron measurements and the beam. The red line represents the beam intensity (expressed in terms of charges) as a function of time; the green line corresponds to the neutron H*(10) in μSv/h. From the plots it was not directly possible to assess if the neutron background was correlated to the beam intensity; only an accurate data analysis with integration over long periods could show the variation of the neutron background as a function of the beam intensity. Hence, raw-data from the WENDI-2 were analyzed off-line and correlated to the SPS beam intensity. The latter was chosen as the sum of the beam intensity on the T2, T4 and T6 targets. The counts were summed up to obtain the integrated counts over a given beam period. The related uncertainty was calculated as the statistical uncertainty of the integrated counts and the WENDI-2 calibration uncertainty (8% systematic error). The average count value over the beam period was multiplied by the counts-to-dose calibration factor. Finally the average dose rate and the associated standard deviation were calculated.

Table 4.1 shows the results of the neutron measurements; no noticeable influence from neutrons originating from the accelerator or the experimental areas at the planned location of the calibration facility was found. The H*(10) values during the proton beam and lead ion beam are comparable with natural background

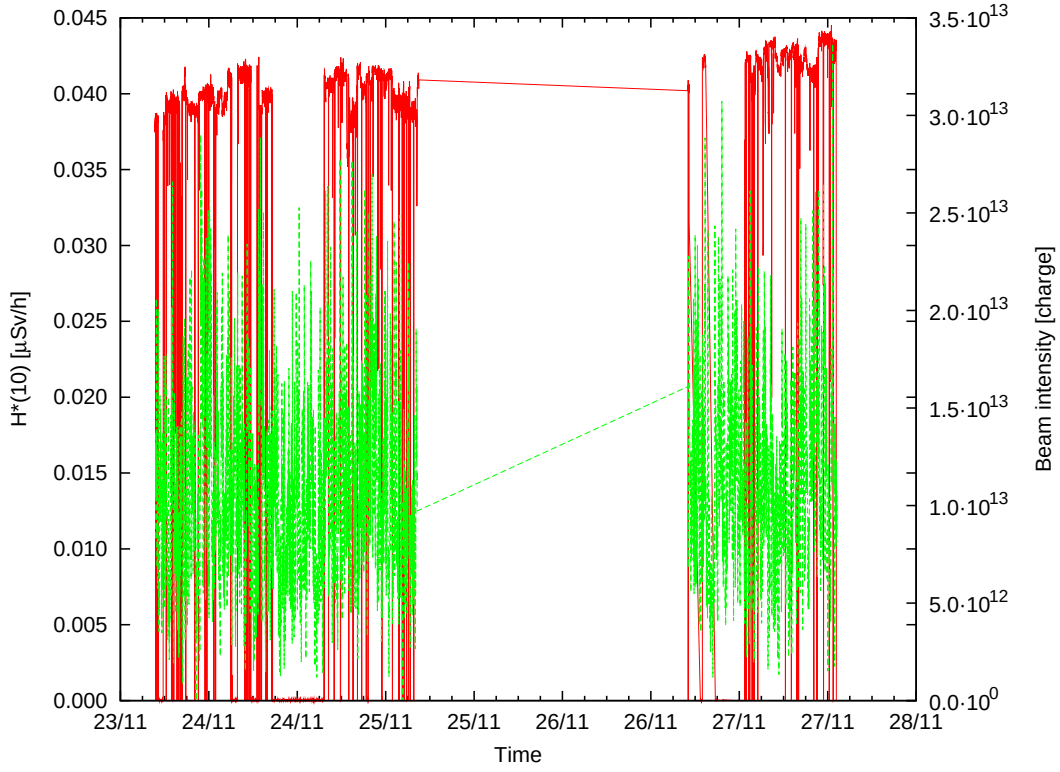

Figure 4.3: *Plot of the SPS beam intensity (red line) and of the neutron H*(10) (green line) as a function of time. Note that the red and green straight lines are plot artifacts due to a beam-off period.*

Table 4.1: *Neutron H*(10) in the location of the calibration facility for each beam condition.*

	Proton beam	**Lead ion beam**	**Natural background**
H*(10) [nSv/h]	15.9±1.7	15.6±1.8	14.5±1.7
t_{meas} [h]	40	16	72

within 1σ. Hence, the place was validated to host the facility.

4.1.2 Laboratory features

Since about 8000 dosimeters and hundreds of portable and fixed detectors are calibrated at CERN every year, a high-standard calibration facility is essential. Taking into account the reasons to replace the previous facility explained in Section 1.1, a new calibration facility was designed, built and commissioned. An extensive study was performed during the design phase to provide not only a state-of-the-art calibration facility but also an innovative facility that could answer the needs of the scientific community.

At the early stage of the project it was foreseen to install a neutron and a gamma source irradiators in two separate rooms; neutron and gamma sources are the most common calibration fields employed at CERN. Since mixed stray radiation fields are also very common at high-energy accelerators, it is fundamental to test the gamma sensitivity of neutron monitors and vice-versa. These detectors are usually calibrated in the operational quantity ambient dose equivalent, H*(10), using standard source-generated photon and neutron fields, separately. Even though this configuration can be considered as a good approximation, it is better to test the detectors under real mixed field conditions. It should be noted that a source-based calibration is not generally applicable to every mixed high-energy radiation field, because the calibration source does not fully account for the energy range encountered at high energy accelerators [29]. Chapter 5 describes in detail the CERF facility where mixed fields at higher energies are available and can be used for the calibrations of active monitors and passive dosimeters. However, the availability of a reference mixed source radiation field was judged to be an important tool to be added to the facility. Hence, the gamma and neutron irradiators were located in the same room and one calibration bench (called Track1) was shared by the two irradiators providing a mixed field. In addition, placing the irradiators in the same room resulted in a shielding optimization (see Section 4.2) and decreased the overall cost of the facility. A second calibration bench (Track2) is available

only for the neutron calibrations.

The radiation field of the facility is completed with an X-ray irradiator and a beta source irradiator. The X-ray irradiator is extensively used for calibration of several devices, e.g. MEDIPIX detector, and is employed for RP studies related to radioactive waste. The beta irradiator, which will be installed in the near future, will provide a beta field for the calibration of contamination monitors and personal dose equivalent, $H_P(0.07)$, measuring devices.

The efficient operation of the CERN accelerators also requires reliable functioning of its control and monitoring systems; many of these are exposed to accelerator radiation and therefore require radiation damage quality assurance. In particular, for the long-term operation of equipment, detailed studies are often required in order to judge whether equipment design life-times can be reached, and if further mitigation measures are required. In this context radiation tests are performed at different stages: during the component selection process, the quality control of purchased batches, and the prototype and production testing. Therefore, an additional irradiation room housing a high intensity Co-60 source (Section 4.1.3) was included in the facility to be used for the above mentioned qualification of electronic components and systems, as well as low-dose, i.e. a few mGy/h, material tests.

Considering that the CERN dosimeter calibration absorbs about 50% of the working time of the facility, a third room was added to install a self-shielded irradiator dedicated exclusively to this task (note that the irradiator is not available yet and will be the scope of a future project). The installation of this irradiator will result in a larger availability of the calibration hall for research and test.

Given all these considerations the laboratory (Figure 4.4) consists of the following rooms (for the letters refer to Figure 4.5):

(a) The calibration hall (Figure 4.6) is the main part of the facility and is used for the calibration of RP survey meters, fixed monitors and dosimeters but also for testing prototype detectors. Three irradiation fields are available: neutrons, photons, X-rays; in the future a beta radiation field will be available. The room is a 13x13x13 m^3 concrete vault, half of which is underground to take advantage of the natural shielding provided by the earth. A maze is located at the entrance of the room. The four side walls are made of 80 cm thick concrete and the concrete roof is 40 cm thick. The room was designed to comply with the radiation protection requirements in terms of radiological classification (refer to Section 4.2 for the RP studies that defined and optimized the layout of the facility). The floor is made of a stainless steel grid designed to support the weight of the different irradiators (see Section 4.1.4 for the description of the irradiators). This kind of floor was chosen to minimize the neutron scattering during neutron irradiation (this topic is extensively described in

Section 4.3).

(b) The irradiation room 1 (Figure 4.7) is used for the qualification of electronic components and systems; it is accessible via a maze facing the storage area; the maze walls are 40 cm thick. The room is 300x445 cm^2 wide and 300 cm high; the side walls are made of 80 cm thick concrete. The wall facing the irradiator is made of a sandwich composed of two layers of concrete and stainless steel slab 10 cm thick in-between for an overall thickness of 120 cm; the roof is made of concrete 40 cm thick (refer to Section 4.2 for the detailed RP study that led to the room layout). A high intensity Co-60 source is available in this room.

(c) The irradiation room 2 will be used for dosimeter calibration with a dedicated self-shielded irradiator and therefore no specific shielding was required. Except for the wall shared with the irradiation room 1, which is 80 cm thick, the other three walls are made of concrete 30 cm thick. The room has a surface of 335x495 cm^2.

(d) The storage area can directly be accessed from outside but the access door can only be opened from inside. The room has a surface of about 45 m^2 and gives access to the calibration hall and to the irradiation rooms 1 and 2. Another door gives access to the control room. This room was conceived for storing and preparing instrumentation before/after irradiation.

(e) The control room houses the irradiator control systems; its surface is about 24 m^2.

(f) The office room can house up to 6 people.

(g) The room dedicated to the computer cluster of the RP group houses three computer racks.

(h) The technical room houses the HVAC (Heat Ventilation Air Conditioning), electricity and water systems, and is accessible only from outside the facility.

(i) Two toilets equipped for disabled people.

Figure 4.4: *The RP calibration facility, building 772.*

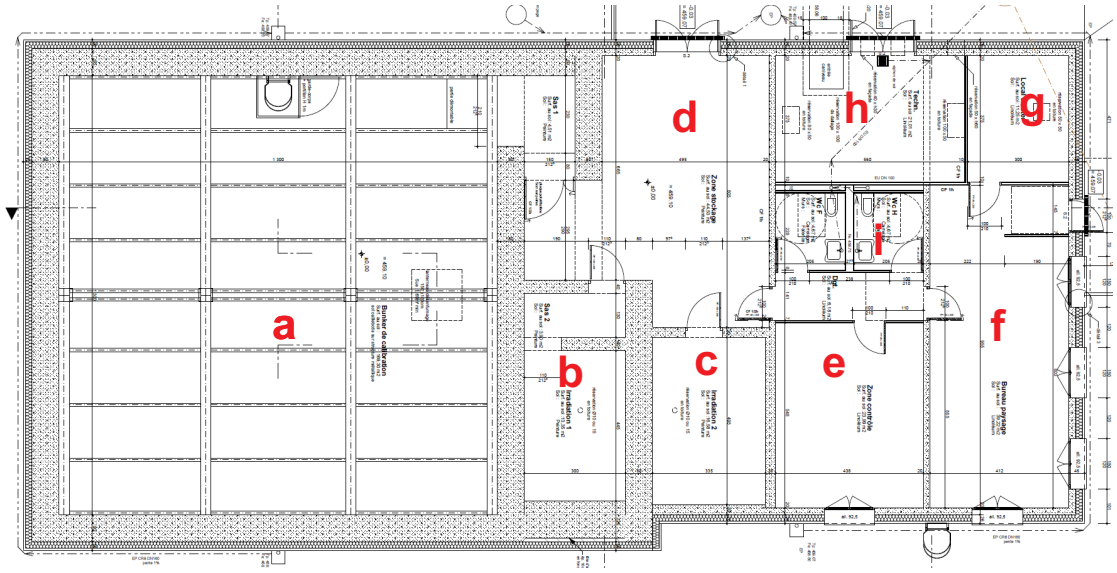

Figure 4.5: *Top cross-sectional view of the calibration facility. For the legend refer to the text.*

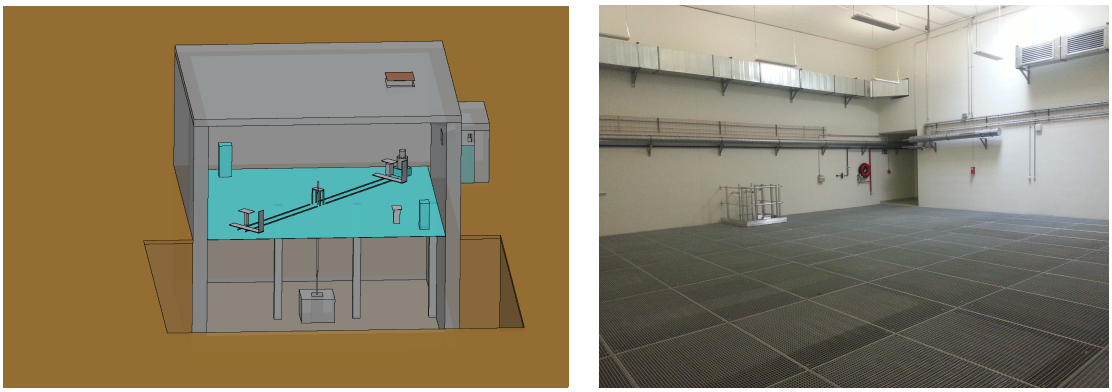

(a) *Simulated geometry* (b) *Status in January 2015*

Figure 4.6: *The calibration hall*

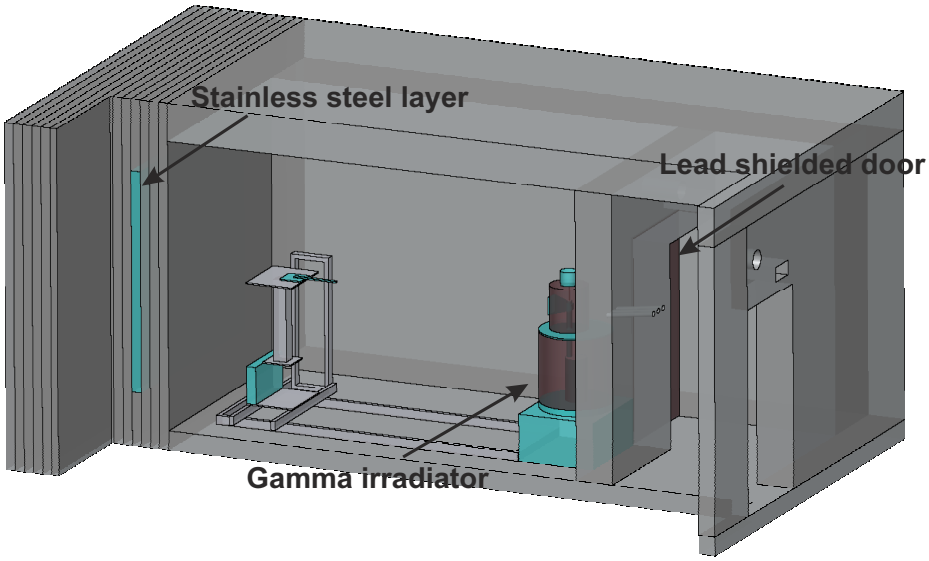

Figure 4.7: *The simulated geometry of the irradiation room 1.*

4.1.3 Radiation sources

The radiation sources were chosen to provide ISO standard calibration fields, meeting CERN requirements. The following radiation fields were provided: neutron, photon, X-ray and beta. Am-Be was selected as the reference neutron source. Ref. [30] recommends that a variation in the dose equivalent rate of more than three orders of magnitude may be required to perform a complete linearity check (e.g. from approximately a few μSv/h to approximately a few mSv/h). Since it is usually impractical to cover this range by varying only the distance, two (or more) sources, varying in strength by factors of 10 to 100, are required. Hence, four Am-Be sources were installed in the calibration hall having the following activities[1]: 888 GBq, 100 GBq, 10 GBq and 100 MBq. It should be noted that for the RP shielding study illustrated in Section 4.2 the highest activity considered was 1 TBq, which was the nominal activity stated in the technical specification of the market survey (a 20% deviation from that value was tolerated).

The photon sources are used in the calibration hall for routine calibrations and in the irradiation room 1 for radiation tests on electronic components. To provide dose equivalent rates from μSv/h to hundreds of mSv/h, five Cs-137 sources with the following activities[2] were installed: 3 TBq, 300 GBq, 30 GBq, 3 GBq and 300 MBq. Figure 4.8 shows the dose rate estimation as a function of the source-to-detector distance for each source (the maximum calibration distance is about 5 m). In addition, a 5 GBq[3] Co-60 source was also purchased to provide higher photon energies. An X-ray generator was installed to provide X-ray reference radiation, as described in Section 4.1.4.

A 11.8 TBq[4] Co-60 source was installed in the irradiation room 1 to provide a photon radiation field with dose rates high enough to perform radiation tests on electronic component and to allow for limited material studies if samples are placed close to the source location. Figure 4.9 shows the dose rate estimation for the Co-60 source of the irradiation room 1. It should be noted that for the RP shielding study of the irradiation room 1 (Section 4.2), the activity taken into account was 10 TBq as required in the technical specification of the market survey (a 20% deviation was also allowed).

Eventually, two beta sources will provide radiation fields for the calibration of beta measuring monitors: 1.85 GBq of Sr-90 and 4 GBq of Kr-85. Sr-90 has a half-life of 28.8 years and decays by β^--emission in Y-90 with an end-point energy of 0.546 MeV. Y-90 also decays by β^- with a half-life of 64 hours and end-point energy of 2.28 MeV. The ^{90}Sr/Y source is a quasi-pure β-source since the photon

[1] Activities in January 2015
[2] Activities in August 2014
[3] Activity in August 2014
[4] Activity in August 2014

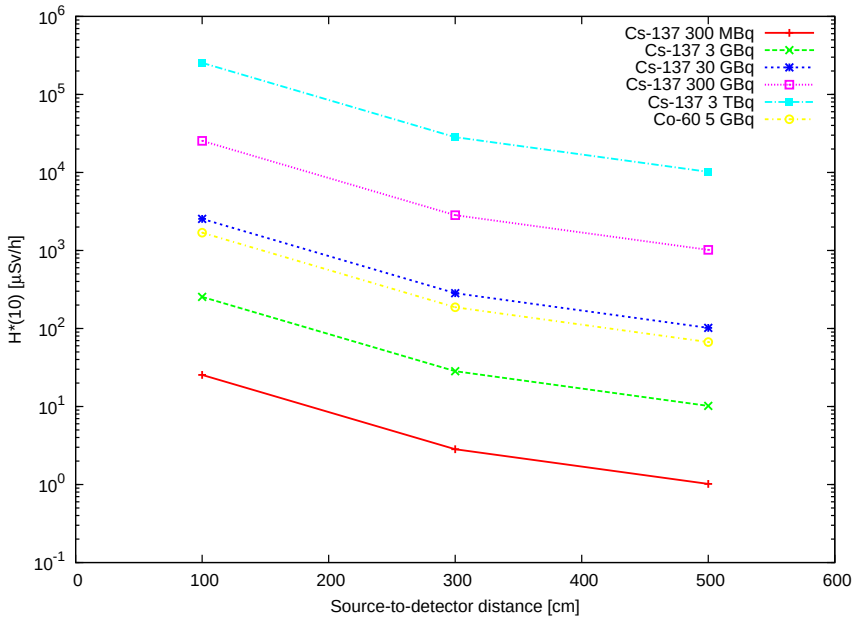

Figure 4.8: *Dose rate estimation for the Cs-137 and the Co-60 sources of the calibration hall as a function of the source-to-detector distance.*

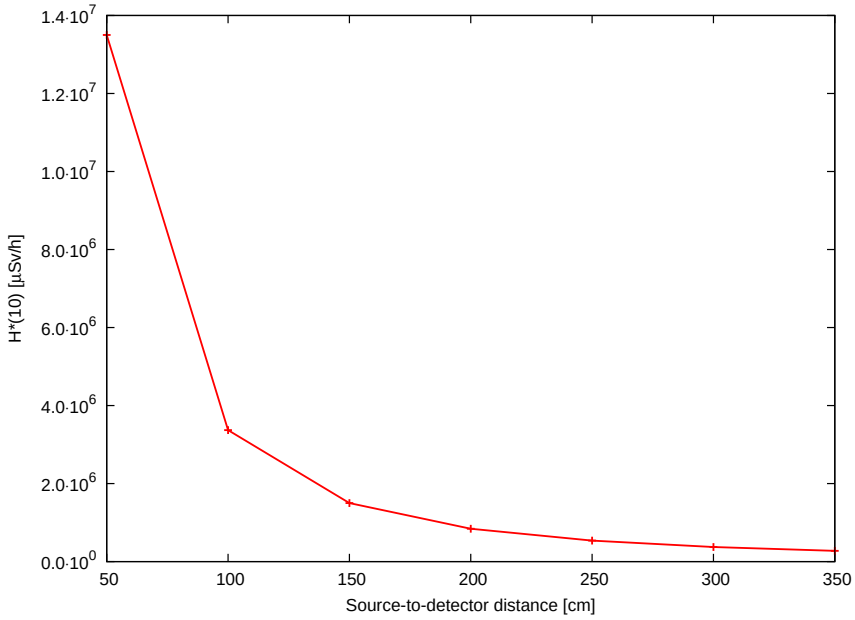

Figure 4.9: *Dose rate estimation for the Co-60 source of the irradiation room 1 as a function of the source-to-detector distance.*

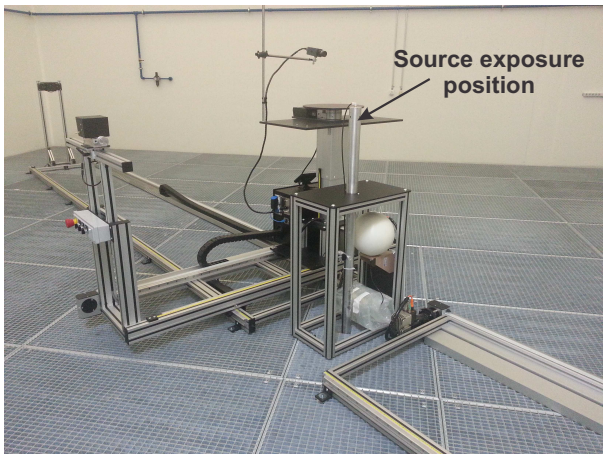

(a) *Exposure tube and calibration bench*

(b) *Source storage*

Figure 4.10: *The neutron source irradiator installed in the calibration hall.*

emission has a very low rate ($1.4 \cdot 10^{-8}$ over the total emission probability). Kr-85 has a half-life of 10.8 years and an end-point energy of 687 keV. Its most common decay (99.57%) is by β-emission. The second most common decay(0.43%) is by β-emission followed by gamma ray emission (with an energy of 514 keV).

4.1.4 Irradiators and layout optimization

Taking into account the source selection of Section 4.1.3, the following irradiators were installed in the facility.

- A neutron source irradiator (Figure 4.10). It is located in the calibration hall and provides a uniform panoramic beam of neutron radiation. The sources are stored in a rectangular shielding consisting of borated polyethylene in a polyester matrix and steel skin, surrounded by 80 cm thick concrete blocks. The storage is located in the underground level of the calibration hall. From its garage position on the bottom of the vault, the neutron source is raised to the irradiation position by a pneumatic system along a pipe 6 m long. The tube is a thin walled aluminum cylinder with a suction cup on its top that holds the source in its irradiation position.

- A gamma source irradiator (model GC60-10, Figure 4.11). It is located in the calibration hall and provides a collimated photon beam. The irradiator consists of a shielded body housing the sources, a beam port and a pneumatic transfer tube that moves the sources between the shielded and exposure positions. The sources are located in the bottom part of the irradiator shielded

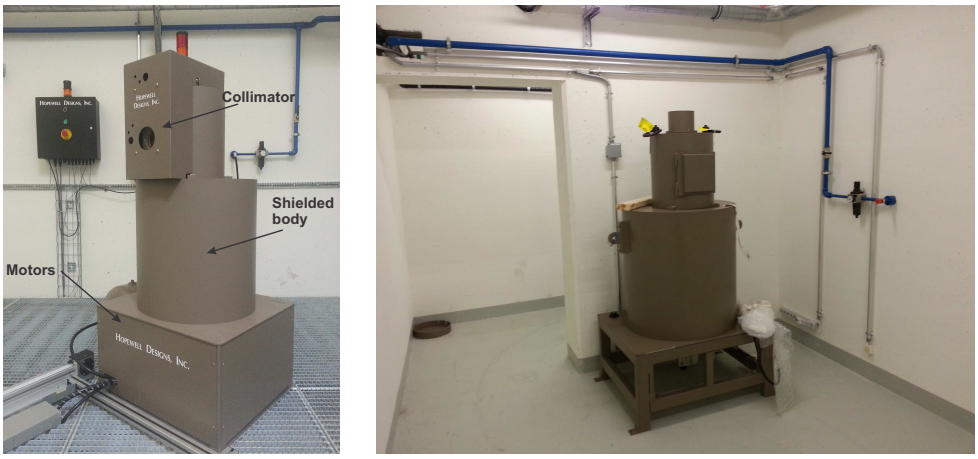

(a) *GC60-10 model* (b) *GC60-1000 model*

Figure 4.11: *The gamma source irradiators.*

on all sides by lead and tungsten. The sources are moved to the exposure position by compressed air and held in place by a suction cup. The different sources are arranged in a motorized carousel that rotates to align the selected source with the transport tube.

- A gamma source irradiator (model GC60-1000, Figure 4.11). It is located in the irradiation room 1 and house the 10 TBq Co-60 source. The irradiator consists of a 5 tons shielded body to limit radiation levels, a collimator, a pneumatic transfer tube that moves the source between the shielded and exposed positions. This gamma source irradiator has the same characteristics as the gamma source irradiator GC60-10 except as noted below:
  - the thickness of the radiation shielding is increased from 16 cm to 26 cm of lead;
  - the top radiation shielding thickness is increased from 11 cm to 17 cm of lead;
  - the collimator has a different design and provides a beam of 30 degrees horizontally and 30 degrees vertically;
  - the beam centreline from the floor is 1.5 m instead of 1.2 m;
  - due to the higher radiation, the source is held in the exposure position via pneumatically controlled rod.
- An X-ray beam irradiator (Figure 4.12). It is located in the calibration hall. The major sub-systems are the X-ray tube, the shielded enclosure, the beam

shutter and the collimator. The X-ray system consists of the tube head with 320 kV, 13 mA and a focal spot 1.5 - 4.0 mm nominal, the high voltage generator a range of 20-320 kV and 0 to 30 mA, the computer with control screen and the Automated Irradiator Software (AIS) and an oil cooler for dissipating the heat produced by the HV generator.

Figure 4.12: *The X-ray beam irradiator.*

- A beta source irradiator: the system is provided with safety interlocks and warning lights. It is controlled through a computer based control system. The system is operated by air pressure. A cover and shielding in front of the sources flips open and expose the source. There are holders installed for filters, which are used to provide a more uniform beam.

In order to define the best irradiator set-up to minimize neutron scattering, a dedicated MC study was performed (a more detailed study concerning the neutron scattering is reported in Section 4.3). It is worth mentioning that according to ref. [3] during a device calibration the room-scatter must not cause an increase in instrument reading of more than 40% at the calibration point.

The study took into account three scenarios (Figure 4.13).

- 1^{st} scenario: the neutron source was placed in the geometrical centre of the hall and the gamma irradiator on the entrance corner. Two opposite irradiation benches were available and the scoring was performed up to 5 m from the source.

- 2^{nd} scenario: the neutron source was displaced by 3 m from the centre along the hall diagonal in order to increase the length of the irradiation bench up to 9 m. A second irradiation bench 3 m long was present.

- 3^{rd} scenario: the neutron source was placed close to one wall of the calibration facility and only one scoring direction 10 m long was available. The contribution of neutrons scattered by the rear wall was removed assigning to this wall the "BLACKHOLE" material;[5] this approximation was taken to reproduce a collimated source.

The results were compared with the ones obtained from a simulation (hereafter named "no scattering") where the scattered neutron contribution was not included; in the latter the neutron source was placed in a sphere 12 m in radius made of "VACUUM[6]" and the neutron fluence and H*(10) were scored from 1 m up to 10 m from the source. The following parameters were in common to each scenario:

- geometry: a simplified geometry of the calibration hall was reproduced according to the description given in Section 4.1.2;
- beta irradiator and X-ray tube locations (Figure 4.13);
- neutron source: an isotropic Am-Be source was reproduced using the FLUKA source routine and the ISO spectrum (Figure 4.14);
- scoring: USRTRACK cards scored the neutron fluence and H*(10) in a sphere 19 cm in radius at several distances from the Am-Be source.

Figure 4.15 and Table 4.2 show the H*(10) as a function of the source-to-detector distance for the four cases. For the three scenarios the contribution of the room-scattered neutrons over the net H*(10) is given. The 1^{st} and 2^{nd} scenarios are fairly similar since the room-scattered neutron contribution is the same up to 4 m from the source. However, the negative direction in the 2^{nd} scenario is more affected by scattered neutrons than that of the 1^{st} scenario, since in the 2^{nd} scenario the source is closer to the corner. In addition, the 2^{nd} scenario provides a maximum negative calibration distance of 3 m rather than 5 m.

The 3^{rd} scenario is the one that mostly minimizes the room-scatter; this is mainly due to the collimation of the neutron source and to the fact that it allows the measuring positions to be sufficiently far from the walls. A disadvantage of this configuration is that a simultaneous calibration of two detectors would not be possible because only one calibration bench would be available.

Figures 4.16 and 4.17 show the neutron spectral fluence at 1 m and 4 m from the source, respectively. If compared with the "no scattering" simulation, the three scenarios show a thermal peak ($\sim$0.04 eV) and a noticeable epithermal part;

[5] "BLACKHOLE" is a fictitious material used to terminate particle trajectories: any particle is discarded when reaching a blackhole boundary.

[6] Particle entering region made of "VACUUM" are transported without interacting.

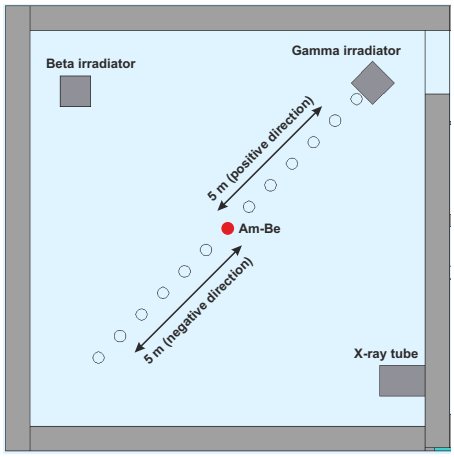

(a) *1st scenario*

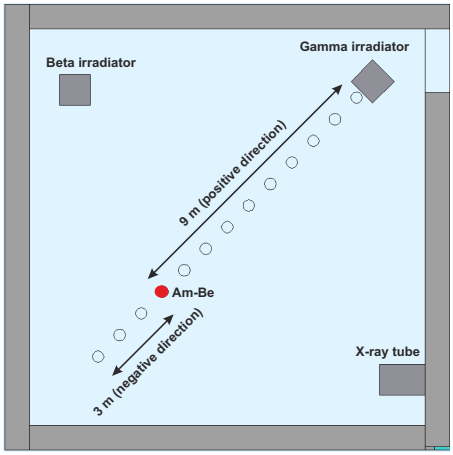

(b) *2nd scenario*

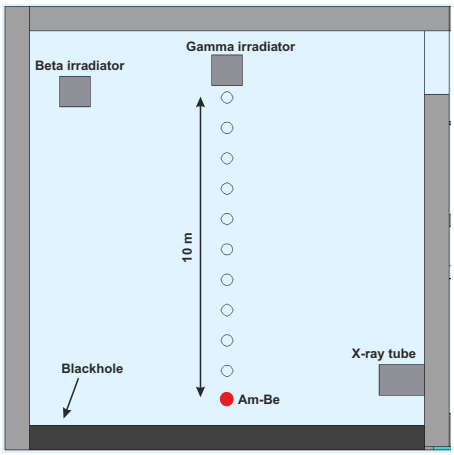

(c) *3rd scenario*

Figure 4.13: *Top view of the calibration hall for each scenario of the MC study for neutron scattering minimization.*

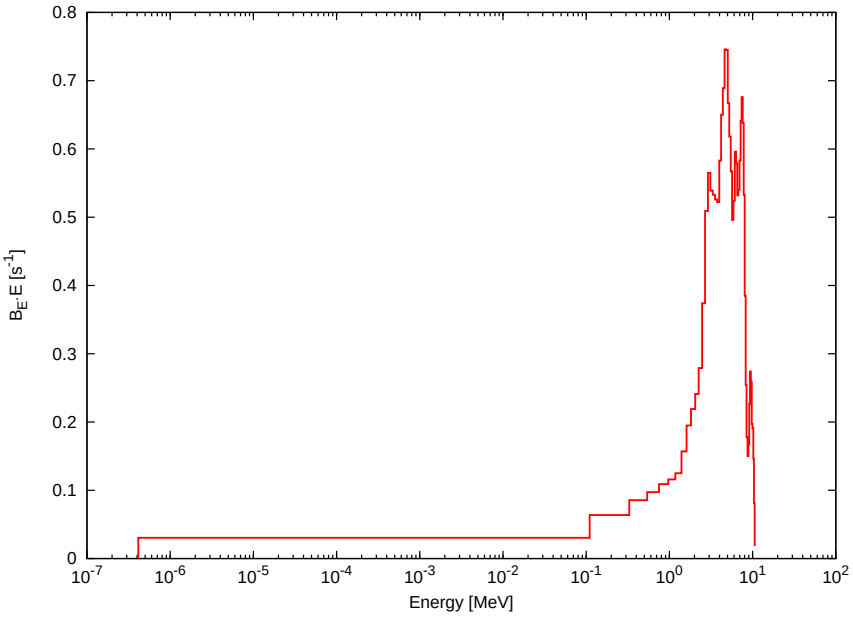

Figure 4.14: *The Am-Be source spectrum employed in the FLUKA source routine [3].*

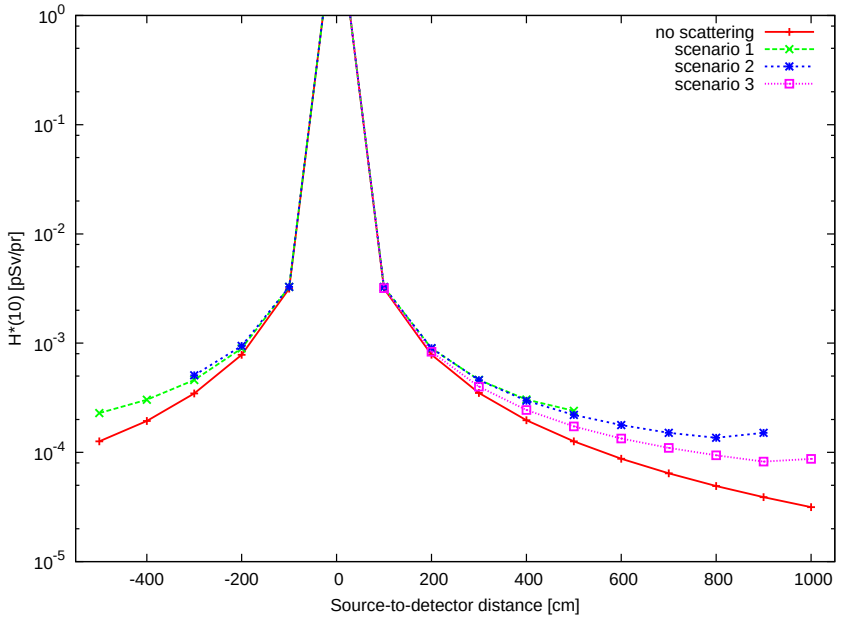

Figure 4.15: *H*(10) in pSv per primary particle as a function of the source-to-detector distance for the four cases studied.*

Table 4.2: *H*(10) in pSv per primary particle as a function of the source-to-detector distance and contribution of the room-scattered neutrons over the net H*(10). The standard deviation is not given since it is always < 1%. na = not available.*

Source-to-detector distance cm	**No scattering** H*(10) pSv/pr	**Scenario 1** H*(10) pSv/pr	Scat %	**Scenario 2** H*(10) pSv/pr	Scat %	**Scenario 3** H*(10) pSv/pr	Scat %
-500	1.26E-04	2.29E-04	82	na	na	na	na
-400	1.94E-04	3.03E-04	57	na	na	na	na
-300	3.46E-04	4.60E-04	33	5.07E-04	47	na	na
-200	7.82E-04	8.94E-04	14	9.43E-04	21	na	na
-100	3.15E-03	3.27E-03	4	3.27E-03	4	na	na
100	3.15E-03	3.26E-03	3	3.26E-03	4	3.19E-03	1
200	7.84E-04	8.94E-04	14	8.99E-04	15	8.34E-04	6
300	3.50E-04	4.61E-04	32	4.59E-04	31	3.99E-04	14
400	1.97E-04	3.05E-04	55	2.97E-04	51	2.44E-04	24
500	1.26E-04	2.40E-04	91	2.20E-04	74	1.73E-04	37
600	8.75E-05	na	na	1.78E-04	103	1.34E-04	53
700	6.43E-05	na	na	1.51E-04	134	1.10E-04	72
800	4.92E-05	na	na	1.36E-04	177	9.39E-05	91
900	3.89E-05	na	na	1.51E-04	287	8.24E-05	112
1000	3.15E-05	na	na	na	na	8.72E-05	177

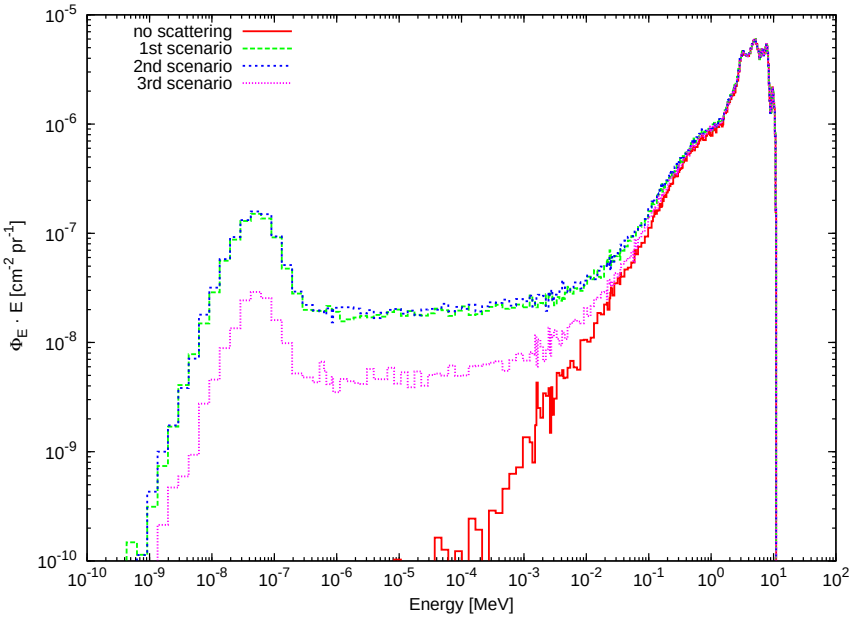

Figure 4.16: *Neutron spectral fluence at 1 m from the neutron source in double log-scale for the four cases studied. The values are normalized per incident particle.*

this is due to neutrons scattered from the walls to the exposure position. The 3^{rd} scenario is less affected by this effect at 1 m. Although the 3^{rd} scenario is preferable to the other two at 4 m, the spectrum is still considerably affected by scattered neutrons.

The following considerations were drawn from this study:

1. Two calibration benches are preferred in order to perform two simultaneous neutron calibrations; the 3^{rd} scenario does not offer this possibility.

2. A dedicated collimator can be designed to decrease the room-scatter effect in the 1^{st} and 2^{nd} scenarios.

3. Neutron calibrations at more than 3 m from the source are possible only in the 3^{rd} scenario; this means that dose rates lower than those of the 1^{st} and 2^{nd} scenarios can be obtained. However, low-dose rates can also be achieved using low-activity neutron sources and measuring at distances less affected by the room-scatter (such as at 1 or 2 m from the source);

4. In all cases, measurements performed too close to the gamma source irradiator are not recommended, because this device would be a source of neutron scattering;

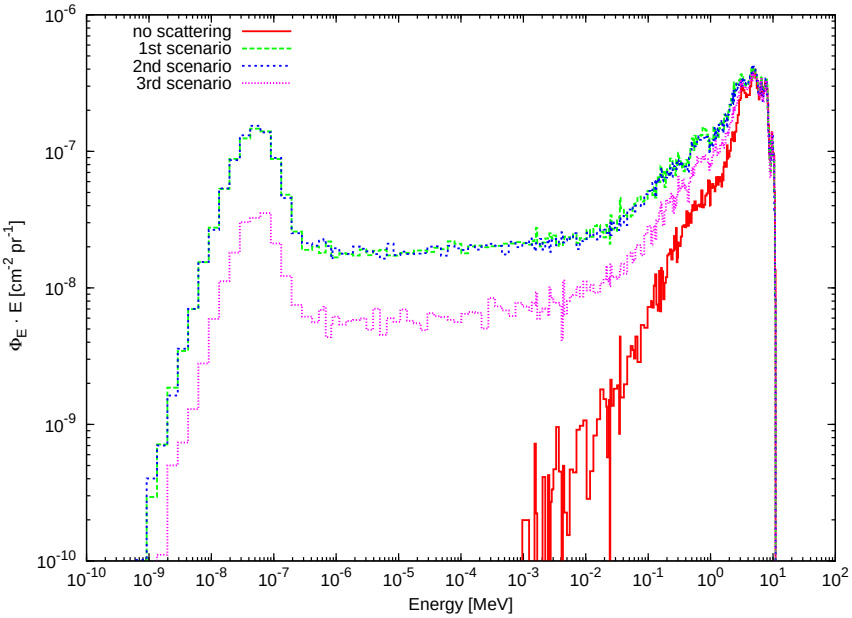

Figure 4.17: *Neutron spectral fluence at 4 m from the neutron source in double log-scale for the four cases studied. The values are normalized per incident particle.*

5. The room-scatter contribution can be evaluated via various techniques, e.g. the shadow cones, and subtracted form the measurements; Monte Carlo study can help in this evaluation.

In conclusion, the 1^{st} scenario was judged to be a satisfactory compromise between low neutron scattering and calibration needs. Beyond 3 m from the source the H*(10) is affected by the room-scatter for more than 40% and therefore these distances should not be used for calibrations. Such distances are useful to obtain lower dose rates but these can also be obtained by employing low-activity neutron sources at distances less affected by the room-scatter.

4.1.5 Safety systems

The safety systems should meet CERN requirements and stay effective to operate. Installing too many and complicated safety systems not always results in a safer operation but can lead to accidents because of their complexity. Keeping them simple but effective is the best solution to protect the personnel from accidental exposure and to facilitate its daily work.

The calibration hall safety systems are the following:

- Door interlock. It is installed at each irradiation room entrance door. When the door is open, the power to the source actuator or shutter is cut, preventing

the source to be moved to its exposure position. Two redundant micro switches monitor the door position. When this interlock is open, the last man out (LMO) operation must be completed before an exposure can begin (see below). If the door is opened during an irradiation the source immediately drops in the shielded position.

- Door photo-eye. Two photo-eyes are mounted in the door frame to serve as a redundant door interlock. They stop an exposure any time an object crosses one of the beams. One is located at waist height, the other at knee level.

- EMergency Off (EMO) switch. When any EMO button is pressed, the irradiator system is forced to its non-exposure state. The EMO buttons latch when pushed and must be manually reset before operation can resume. Each EMO button is clearly labeled. EMO buttons are located on one wall of the exposure room, on one wall in the basement, on each linear positioning system (LPS), on the control panels and on each control unit in the control room.

- Warning lights. A red flashing warning light is on whenever the source is exposed or shutter open. It is located inside the irradiation room so that it is readily visible from the entrance door. In addition, a second warning light is mounted outside the door.

- Last-Man-Out (LMO) switch. The LMO condition confirms that all personnel have left the room. As the last person exiting the room presses the LMO switch, a warning light and horn turn on; the operator must exit the room and close the door within the allotted time (30 seconds). The LMO operation must be successfully completed before an exposure can begin.

- System enable switch. The irradiator control rack has a turn-key system with two positions: "safe" and "enable". In order to start an irradiation it must be turned on the "enable" position. Moreover, the irradiator control system is password protected.

The control screen shows the status of the interlock systems and has indicators for: the door interlock, LMO, photo-eyes, calibration bench position, system enable key and general safety status. If errors occur in the safety system, these are displayed on the computer screen. The software constantly checks multiple parameters. If any error occurs, the source is returned to the safe, shielded position (or shutter closed). The pneumatic systems driving the sources are designed so that any failure will bring back the sources to the shielded position. Low pressure in the pneumatic system will activate the low pressure switch, preventing operation. All

solenoid valves must be energized to operate. Power loss to individual components or the entire system will set it to safe state. The electrical system is designed to be fail-safe and independent of any computer software or programming. The power to the solenoid magnets that expose the source or keep it in the exposed position is hardwired through the safety interlock system. If the door is opened, if an EMO switch is pressed, or if the system enable key is turned off, power to the solenoids is lost and the source will return to the shielded position (or the shutter closed on the X-ray system). Three radiation monitors (two for gamma and neutron radiation of the calibration hall and one for gamma radiation of room 1) provide information on the irradiator exposure state. The displays are located at the control panel and show the exposure rates in μSv/h. An audible and visual alarm circuit is actuated in the event that the room door is open and there is an elevated exposure rate. A camera with zoom lens is mounted to a pan/tilt unit. A control system allows the camera to be moved and the lens zoomed to be able to view the entire room. Two TV screens showing all cameras are provided in the control room. The same safety system above-described is provided for the irradiation room 1. Since this room has two doors (a lead shielded one and a standard one), interlocks are provided for each door to ensure that the irradiation can start only if both doors are closed.

4.2 Radiation Protection studies

This section describes the RP optimization studies performed during the laboratory design phase: shielding definition, skyshine effect, air and concrete activation and ozone production. A verification of the shielding calculations was also performed after the source installation and is illustrated at the end of this Section.

4.2.1 RP area classification

H*(10) limits were assigned to each room of the facility to establish the objectives for the RP shielding study. These values were defined according to the CERN RP regulation on radiological area classification (Table 4.3) [26]. However, before defining the limits several considerations were taken into account. The rooms where the personnel permanently works, i.e. 8 h/day, and where radiation sources are not present, shall be classified as non-designated areas. Zones where radiation sources are present shall be classified at least as supervised areas. During irradiation the access to the irradiation room shall not be permitted; this is ensured by the safety systems (Section 4.1.5). Moreover, following the specifications given by the irradiator manufacturer, the H*(10) at the surface of the irradiators is < 50 μSv/h when the sources are in the shielded position. Therefore, the irradiation rooms

Table 4.3: *CERN radiological area classification.*

Area	**Dose limit** [mSv/year]	**Ambient dose equivalent rate** Permanent occupancy 8 h/day	Low-occupancy < 8 h/week
Non-designated	1	0.5 μSv/h	2.5 μSv/h
Supervised	6	3 μSv/h	15 μSv/h
Simple controlled	20	10 μSv/h	50 μSv/h
Limited stay	20	/	2 mSv/h
High radiation	20	/	100 mSv/h
Prohibited	20	/	>100 mSv/h

were classified as simple-controlled areas. To decrease the shielding constraints, the area located between the irradiation rooms and the offices, was classified as supervised-area. Eventually, the following RP classification was implemented:

- non designated areas: offices, the control room, the technical room, the cluster room, the toilets and the area outside the facility;
- supervised areas: the storage room;
- simple controlled areas: the calibration hall, irradiation rooms 1 and 2;
- the roof area was not classified since not accessible during irradiation; however, the ALARA (As Low As Reasonably Achievable) was taken into account.

4.2.2 Shielding optimization study for the calibration hall

A MC study was carried out via the FLUKA [14, 15] code to fulfill both radiation protection and civil engineering requirements. Several building designs were considered and compared. This section discusses the results for two configurations and the detailed study for the final design. The latter profited from the results of the other options and was the outcome of an accurate optimization work. Because of structural changes in the laboratory design, additional calculations were performed during the construction phase to validate the modifications.

The sources providing the highest dose rates were considered in the study; the 1 TBq Am-Be source was considered as the largest contributor among the neutron sources. The results given by FLUKA were normalized via source neutron emission rate, i.e. $8.2{\cdot}10^{7}$ s^{-1}. This was obtained using the *calculated* neutron yield of the

Am-Be source, i.e. 82 neutrons per 10^6 alpha particles [16]; this is about 17% higher than the *experimental* one, which is equal to 70 neutrons per 10^6 alpha particles. The highest dose rate among the gamma sources is provided by the 3 TBq Cs-137. The calculations performed for these two sources are conservative estimates for the other sources of lower activities and as well for the X-rays generated by the X-ray beam irradiator.

In the 1^{st} configuration (Figure 4.18) a 13x13x13 m^3 concrete vault was modeled; this size was chosen to minimize the scattered neutron contribution. The walls and the roof were made of concrete 40 cm and 20 cm thick, respectively. Since concrete is efficient in shielding neutrons and photons, it is a suitable shielding material and is also a standard structural material for building constructions widely available. The Am-Be source was placed in the geometrical centre of the room. In the DEFAULTS card, option PRECISIOn [14] was chosen as default; this sets the transport of neutrons down to thermal energies[7]. Scoring of the ambient dose equivalent rate was performed via the USRBIN card every 15 cm in a cube of 30x30x30 m^3 volume around the radiation source. Figure 4.19 shows that the H*(10) generated by the Am-Be source outside the shielding walls is about 5 μSv/h; this value is not compliant with the requirements for non-designated areas. The H*(10) is about 10 μSv/h on the roof; even though the RP requirement on the roof was less strict since it was decided to fence it avoiding unauthorized access, the thickness of 20 cm was not judged sufficient. This decision was based on the fact that neutrons emerging from the roof can scatter with the air to the ground increasing the H*(10) in the area around the laboratory (this is effect, called skyshine, is explained in Section 4.2.4).

In the 2^{nd} configuration (Figure 4.20) the lower half of the hall was located underground and the floor at the ground level. This choice simplified the civil engineering construction and took advantage of the natural shielding provided by the soil. Moreover, the soil coming from the hole excavation was added as shielding to the concrete walls; in fact, soil is appropriate to shielding neutrons and photons. The soil shielding was triangular prism shaped (the prism section had two sides and the hypotenuse 5 m and 7.07 m long, respectively). The walls remained 40 cm thick, except one wall, the thickness of which was increased up to 80 cm; the last one was designed to shield more efficiently the side of the control room. The same parameters of the 1^{st} configuration were employed. Figure 4.21 shows that the H*(10) generated by the Am-Be source is below 0.2 μSv/h outside the soil shielding and the wall 80 cm thick. The H*(10) is about 4.5 μSv/h on the roof. The soil shielding achieves the requirement for non-designated areas and is fairly equivalent to a concrete wall 80 cm thick.

[7]PRECISIOn sets also the tracking of electromagnetic particles down to 33 keV for photons and 100 keV for electrons and positrons

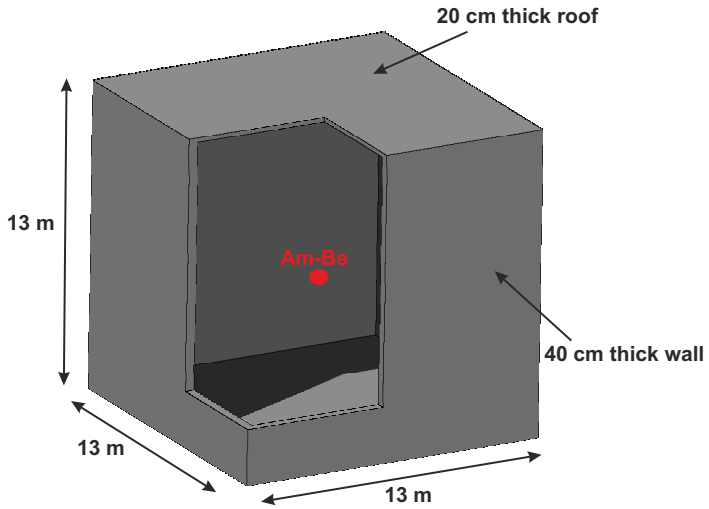

Figure 4.18: *1st configuration: cross-sectional view of the geometry. Colour legend: grey = concrete.*

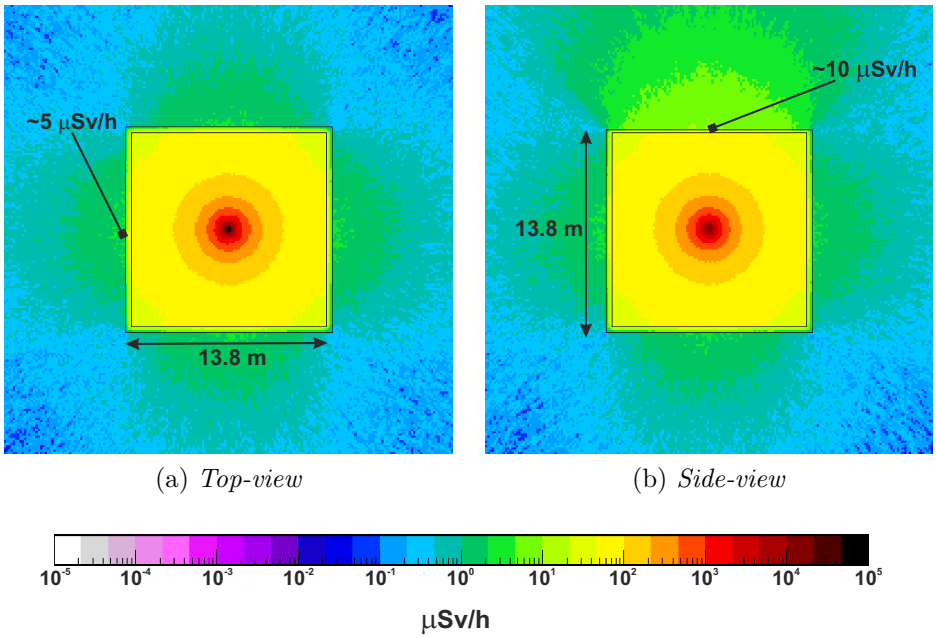

(a) *Top-view* (b) *Side-view*

Figure 4.19: *1st configuration: ambient dose equivalent rate caused by the Am-Be source. The projecting planes cut at the source level.*

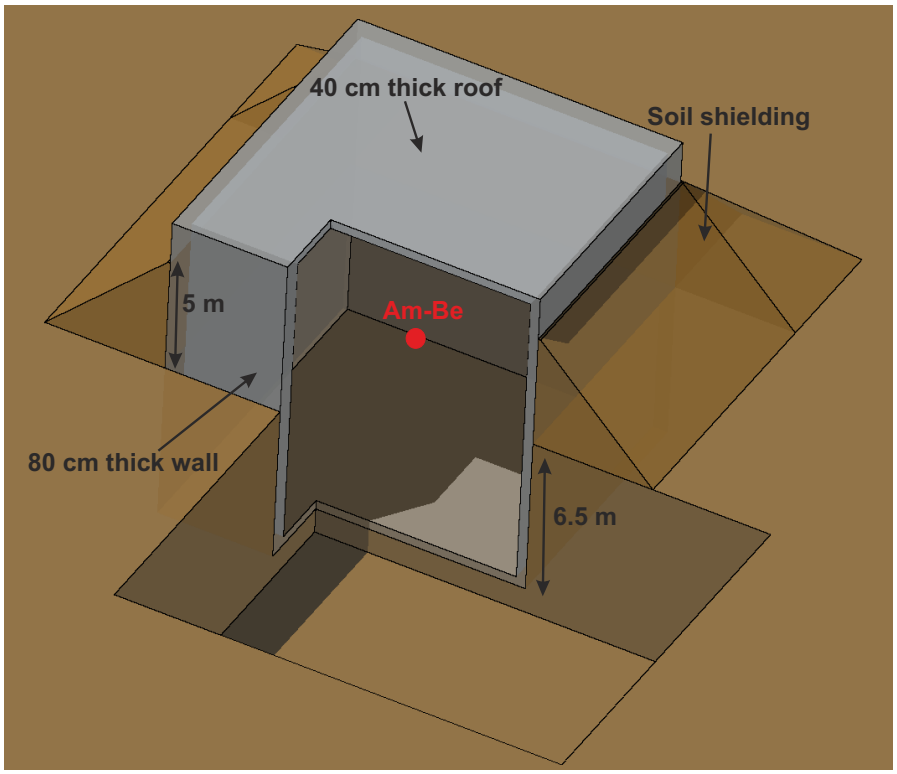

Figure 4.20: *2nd configuration: cross-sectional view of the geometry. Colour legend: grey = concrete; brown = soil.*

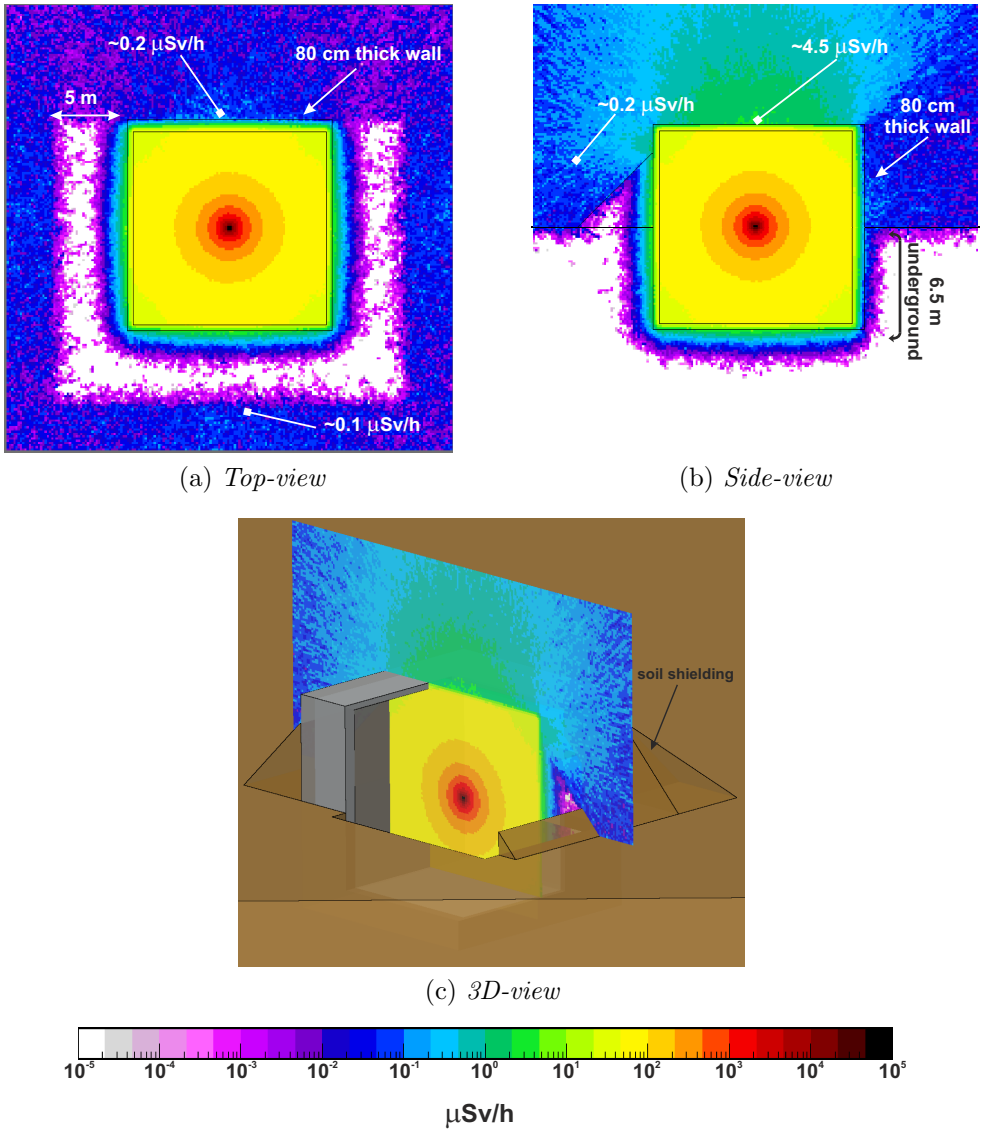

(a) *Top-view* (b) *Side-view*

(c) *3D-view*

Figure 4.21: *2nd configuration: ambient dose equivalent rate caused by the Am-Be source. The projecting planes cut at the source level.*

Taking into account the results of these and other studies, which are not illustrated here, and the recommendations given by the civil engineers, the following considerations were drawn.

- Radiation shielding. Since concrete walls 80 cm thick are equivalent to the soil shielding, the former complies with radiation protection criteria. However, soil shielding shows two main issues: firstly, its cost is not cheaper than that of concrete walls 80 cm thick; secondly, in the long term the soil prism shaped shielding would be less stable and could lose its radiation protection effectiveness whereas concrete is not affected by this problem.

- Roof. The roof thickness was a critical issue for the civil engineering. If the roof was too thick, its construction would not be simple. On the other side, if it was too thin, it would result in increasing the skyshine. A roof 40 cm thick was judged to be a good compromise between radiation protection and civil engineering constraints.

- Calibration hall installation. The choice of locating the lower half of the building underground facilitated radiation protection and the building construction.

- Access to the calibration hall. To avoid radiation streaming through the entrance door, the construction of a maze was foreseen. Calculations showed that a neutron shielding on the entrance door was necessary to decrease the H*(10) below the limit of a supervised area; hence, the door was shielded with a polyethylene slab 5 cm thick since polyethylene is an effective material in shielding neutrons with energies below a few MeV.

The above-mentioned choices were verified via a detailed simulation study (hereafter called "final study"). Figure 4.22 shows the geometry, which reproduced accurately the calibration hall according to the technical drawings shown in Figures 4.5 and 4.6. The soil composition and density were chosen to be the equal to the soil in Prévessin according to ref. [31]. The entrance is a maze closed by a 5 cm thick polyethylene shielded door; the facility walls were made of standard FLUKA concrete [14]. The source was placed in the centre of the room, 120 cm above the grid floor. The building was located inside a sphere sufficiently large (3 km in diameter) to reproduce the skyshine effect. In addition, a 150x150 cm^2 wide aperture was made in the roof because of fire protection requirements. This aperture was a legal obligation for a building of that size in order to provide smoke extraction in case of fire. It should be noted that the fire load is very limited in the calibration hall.

Figure 4.23 shows that the H*(10) generated by the Am-Be source just outside the concrete walls is below 0.2 μSv/h; this value is fully compliant with CERN RP requirement for non designated areas. The H*(10) stays below 2 μSv/h outside the entrance door, i.e. in the storage area, which was classified as supervised area; hence, the strictest limit (3 μSv/h for permanent occupancy) is fully respected. On the roof the H*(10) is below 5 μSv/h, except in correspondence with the smoke extraction aperture, where it reaches about 45 μSv/h. The aperture is closed by a polycarbonate window 1 cm thick. It is foreseen to design and place a polyethylene slab to significantly reduce the H*(10). For general safety and radiation protection reasons the roof is fenced and accessible via a locked ladder only under special conditions. Figure 4.22 shows two ventilation ducts; the simulation results showed that the H*(10) in correspondence of the ducts is about 5 μSv/h; this fairly low value is the result of having tilted them by 45 degrees to avoid the direct radiation streaming. Considering the presence of additional concrete walls and a door, the H*(10) is expected to be below 10 nSv/h in the control room and below 5 nSv/h in the office space.

The final study was completed by simulating the operation of 3 TBq Cs-137 source. The geometry employed was the same as for Figure 4.22. The gamma beam emitted by the Cs-137 source was reproduced in FLUKA via a dedicated source routine, the irradiation angle was 30 degrees. The source was placed in the corner close to the maze, 100 cm above the grid floor. The results given by the USRBIN card, expressed in pSv per primary particle, were then normalized via the source activity to obtain the dose rate in μSv/h.

Figure 4.24 shows that the H*(10) generated by the Cs-137 source is everywhere well below the limits for non-designated areas outside the walls and reaches its maximum, i.e. 0.4 μSv/h just outside the entrance door. The H*(10) is below 0.1 μSv/h on the roof, except in correspondence of the smoke extraction aperture where it reaches the maximum of 10 μSv/h. An additional estimation was carried out with an online calculator available on the Nucleonica website [32]; it allows the photon H*(10) to be calculated for a specific source-to-detector distance (a shielding can also be added in the calculation). The following parameters were implemented to calculated the H*(10) produced by the Cs-137 source just outside the walls of the facility:

- isotope and activity: 3 TBq of Cs-137;
- source-to-detector distance: 16.1 m;
- shielding material and thickness: concrete 80 cm thick;
- build-up factors included in the calculation.

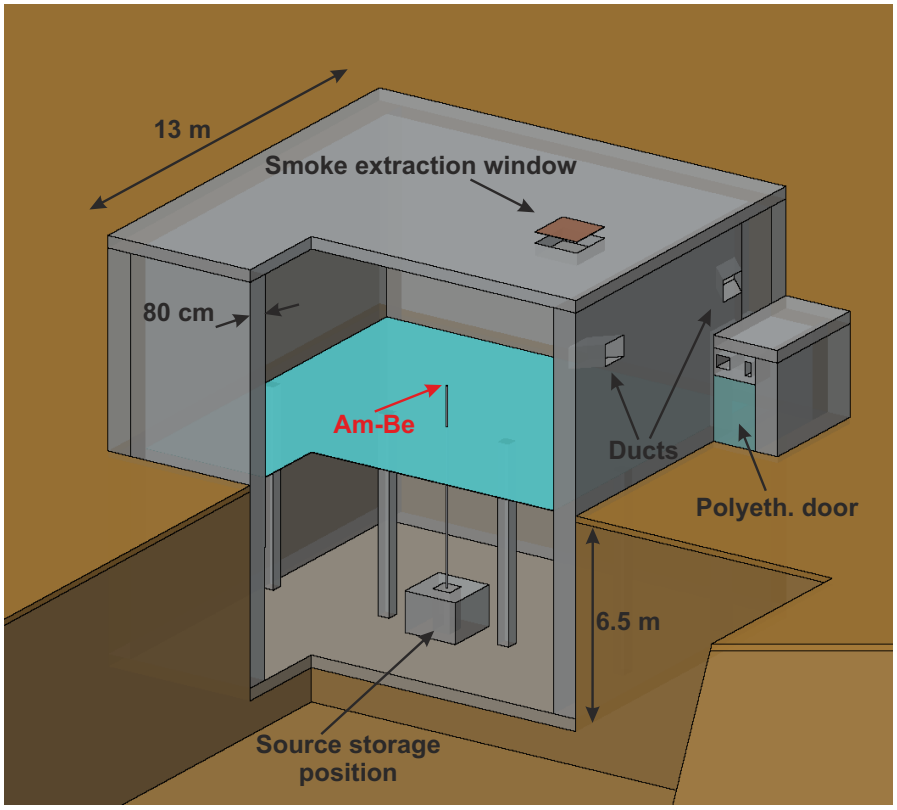

Figure 4.22: *Cross-sectional view of the geometry employed in the final study. Colour legend: brown = soil; grey = concrete; turquoise = stainless steel.*

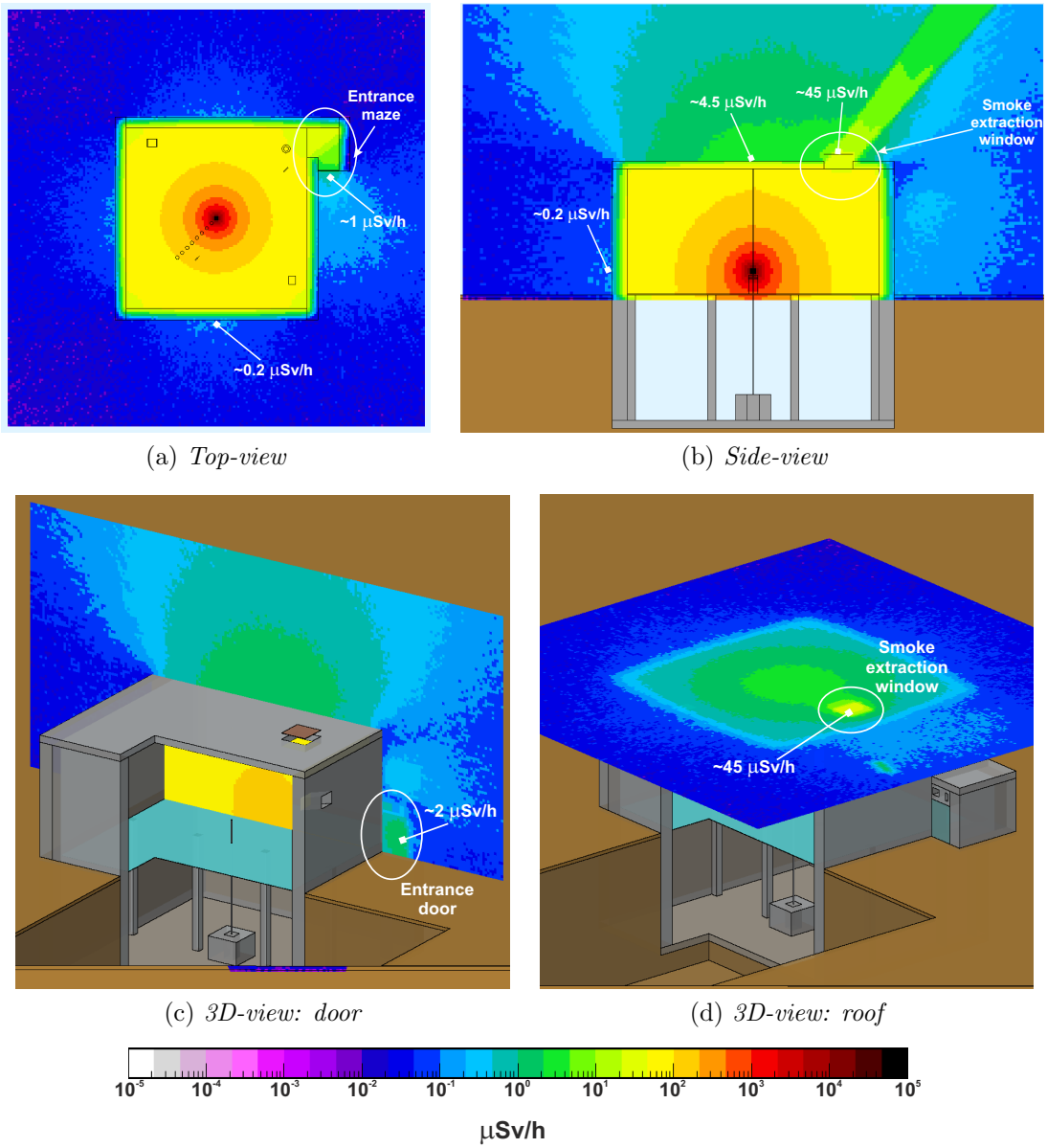

(a) *Top-view* (b) *Side-view*

(c) *3D-view: door* (d) *3D-view: roof*

Figure 4.23: *Ambient dose equivalent rate caused by the Am-Be source for the final study. The projecting planes cut at the source level in (a) and (b), at the door level (c) and at the roof level (d).*

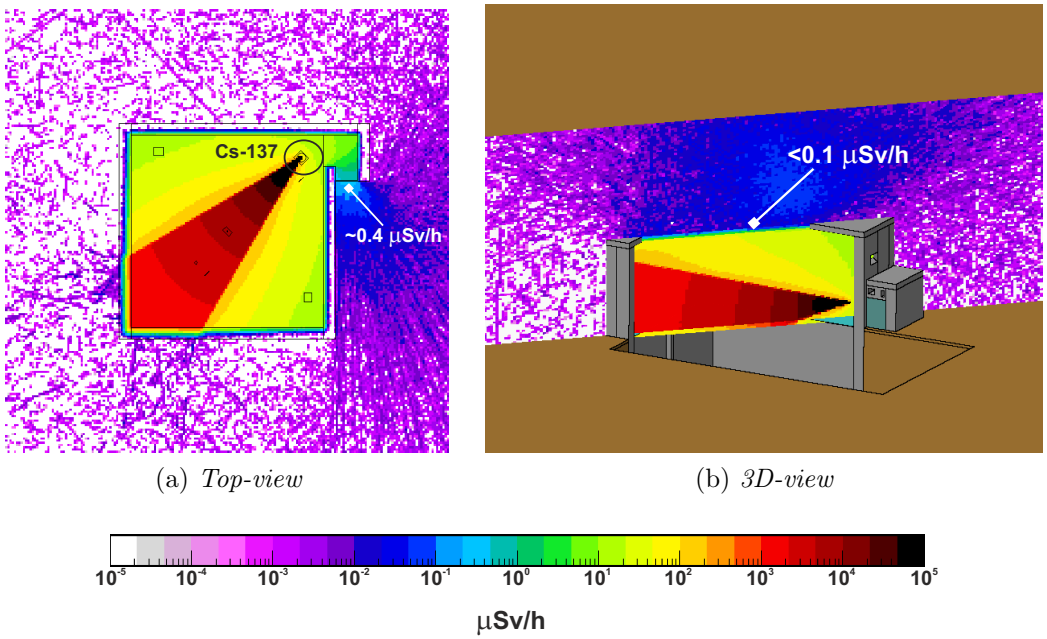

(a) *Top-view* (b) *3D-view*

Figure 4.24: *Ambient dose equivalent rate caused by the Cs-137 source for the final study. The projecting planes cut at the source level.*

The results of the Nucleonica calculation gave a value of 20 nSv/h; this was a conservative evaluation and confirms the prediction of the MC method. The same calculation was performed for the 5 GBq Co-60 source; the resulting H*(10) was 2 nSv/h. Therefore the simulations for the Cs-137 source were assumed to be a conservative estimate also for the Co-60 source. If a simultaneous gamma/neutron irradiation is performed in the calibration hall using the 1 TBq Am-Be and the 3 TBq Cs-137 sources, the H*(10) outside the entrance door does not exceed 2.5 μSv/h, which is lower than the strictest limit for supervised areas.

4.2.3 Shielding study for the room 1

Several configurations were evaluated for the irradiation room 1; one among these (indicated as "early study" from now-on) is illustrated in this section as well as the results for the final radiation protection study. Due to its purpose, the room 1 is smaller than the calibration hall and the calibration bench was required to be about 3 m long. The room width and length, i.e. 3 m and 4.5 m respectively, were established in order to make the gamma beam approximately covering the entire wall facing the irradiator, hence 3 m and 4.5 m, respectively. The room access was made via a maze to mitigate the radiation streaming. In the early study (see Figure 4.25) the wall facing the irradiator was made of concrete 100 cm

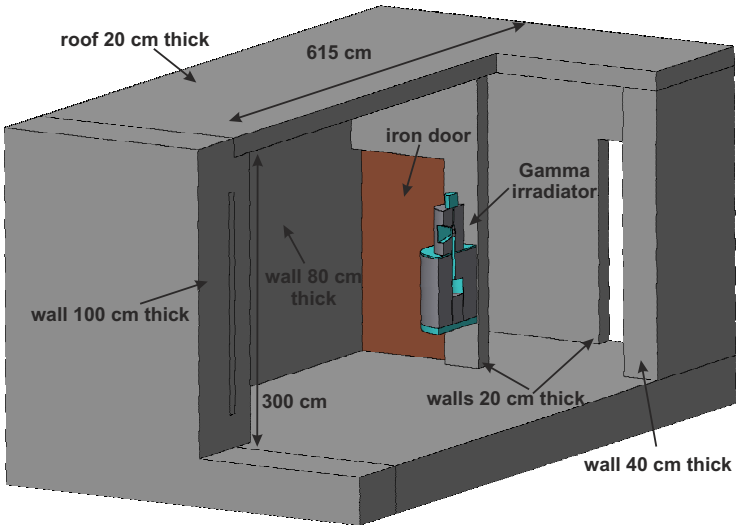

Figure 4.25: *Early study: cross-sectional view of the geometry. Colour legend: brown = iron; turquoise = stainless steel.*

thick; the two side walls were made of concrete 40 and 80 cm thick, respectively. The 80 cm thick wall was the one in common with the calibration hall. The maze was composed of two walls 20 cm thick each and the roof was 20 cm thick. An iron door 2 cm thick was located after the maze. The irradiator was modeled according to the technical drawing provided by the manufacturer. The Co-60 source was reproduced by setting in the BEAM card the SDUM to ISOTOPE and then adding the HI-PROPErties card with Z=27 and A=60. These options allow an isotope to be defined as an isotropic source. Scoring of the H*(10) was performed with the card USRBIN every 15 cm around the room. The results were then normalized via the source activity, i.e. 10 TBq.

Figure 4.26 shows that the H*(10) outside the wall facing the irradiator is about 4 μSv/h. It reaches 20 μSv/h outside the wall 40 cm thick and 40 μSv/h at the entrance. The H*(10) on the roof is about 5 mSv/h, which does not meet the RP requirements and is therefore not acceptable. Moreover, the H*(10) outside the entrance door is 40 μSv/h, which is too high if compared with the limit for a supervised area. The 2 cm iron thick door was not a sufficient shielding as well as the thickness of the two maze walls.

Taking into account the considerations coming from the early study, several modifications were implemented:

- the wall 40 cm thick was enlarged to 80 cm;

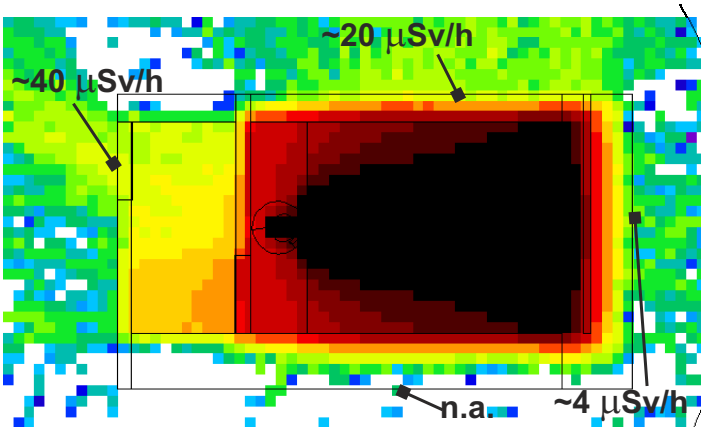

(a) *Top-view*

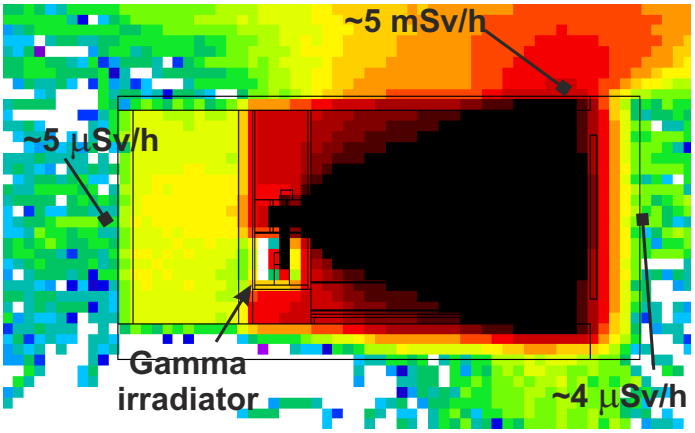

(b) *Side-view*

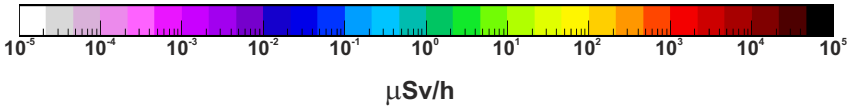

Figure 4.26: *Ambient dose equivalent rate caused by the Co-60 source for the early study. The projecting planes cut at the source level.*

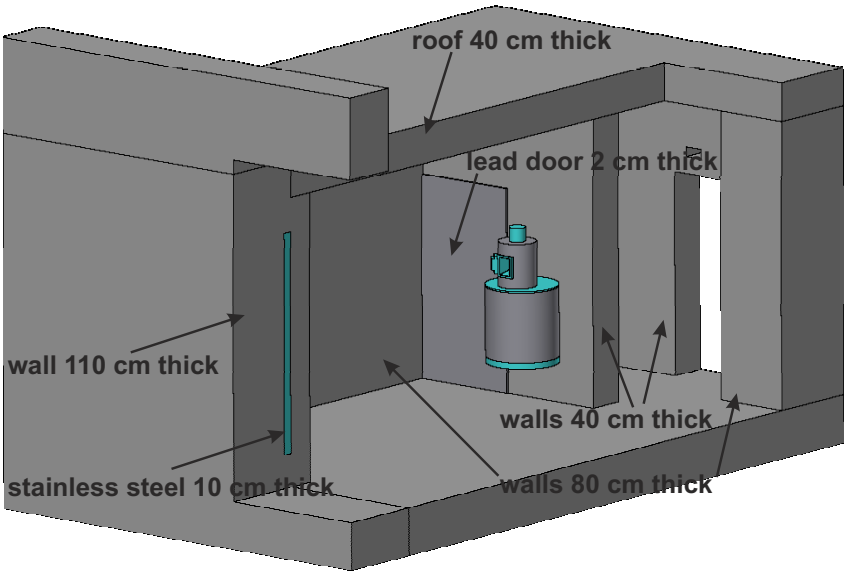

Figure 4.27: *Final study: cross-sectional view of the geometry.*

- the wall facing the irradiator was increased to 110 cm and a stainless steel slab 10 cm thick was added;
- the roof thickness was increased to 40 cm;
- the entrance door was made of lead 2 cm thick, which is equivalent to an iron door 4 cm thick;
- the walls of the maze were enlarged to 40 cm.

Figure 4.27 shows the geometry employed in the final study, where the parameters were the same as the one used in the early study. Figure 4.28 shows that the H*(10) is around 2 μSv/h outside the maze and below 0.1 μSv/h outside the wall located in front of the irradiator. The H*(10) produced in the nearby calibration hall and irradiation room 2 is negligible. The H*(10) generated on the roof stays below 150 μSv/h; even though this value is very high if compared with the limit for a non-designated area, instead of increasing the roof thickness, it was decided to measure the H*(10) once the source will be installed. If needed, an appropriate stainless steel slab could be installed only in the "hot spot" area to reduce the H*(10) (see Section 4.2.7 for the measurement of the H*(10) on the roof of room 1).

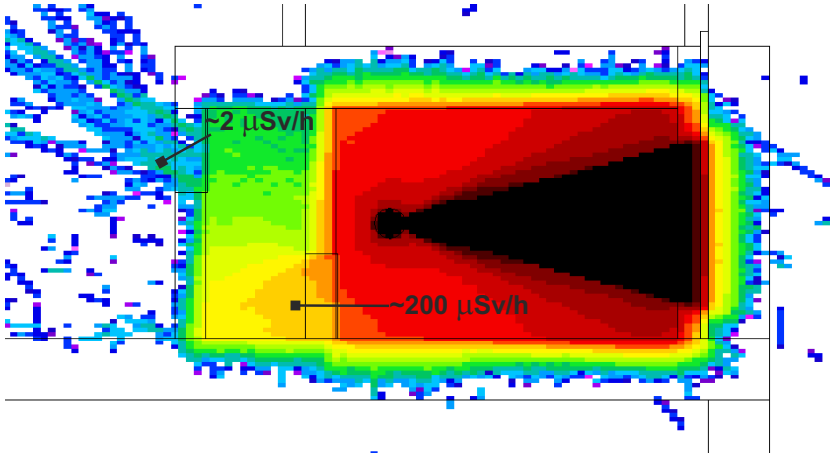

(a) *Top-view*

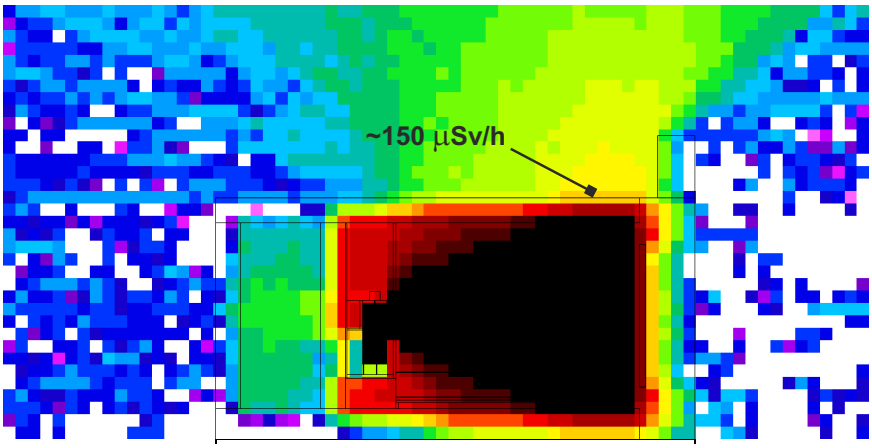

(b) *Side-view*

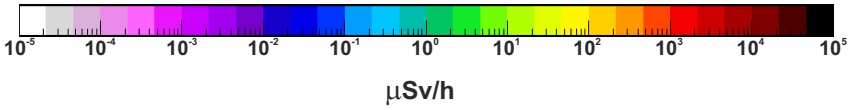

Figure 4.28: *Ambient dose equivalent rate caused by the Co-60 source for the final study. The projecting planes cut at the source level.*

4.2.4 Study of the skyshine effect

Radiation may extend out to large distances from a source, as well as radiation coming directly through the shield and in a straight line, radiation may also indirectly reach points at large distances by mean of air scatter. This latter type of radiation is named skyshine and is critical in terms of dose rate especially around high-energy hadron accelerators. It is usually due to relatively high levels of neutrons escaping upwards through holes or thin parts of an accelerator shielding in areas that are normally inaccessible during accelerator operation [33]. However, skyshine could also be important nearby neutron calibration facilities, since neutrons emerging from the roof could scatter with the air being redirected to the ground increasing the H*(10). The shielding results of Section 4.2.2 already included this effect since the air sphere surrounding the facility was 3 km in diameter; this thickness was sufficient to reproduce skyshine effect. FLUKA simulations were performed to provide an estimation of the importance of skyshine. The parameters used in these simulations were the equal to the ones employed for the final shielding study (Section 4.2.2), except for the air surrounding the facility that was substituted with vacuum. This set-up allowed the skyshine to be switched off. The results were compared with the ones of the final study, where the skyshine was included.

Figures 4.29 and 4.30 show the H*(10) inside and outside the facility generated by the operation of the Am-Be source with and without skyshine. It is evident that the skyshine increases the ambient equivalent dose rate outside the facility, in particular its effect becomes significant at greater distances from the facility. For instance, the H*(10) at 6.5 m from the walls of the facility with the skyshine is about 40 nSv/h and without the skyshine is 20 nSv/h.

These results show that skyshine has a fairly importance also for RP calibration facility where panoramic neutron sources are employed. This effect has to be included in MC studies in order to plan, if needed, adequate shielding.

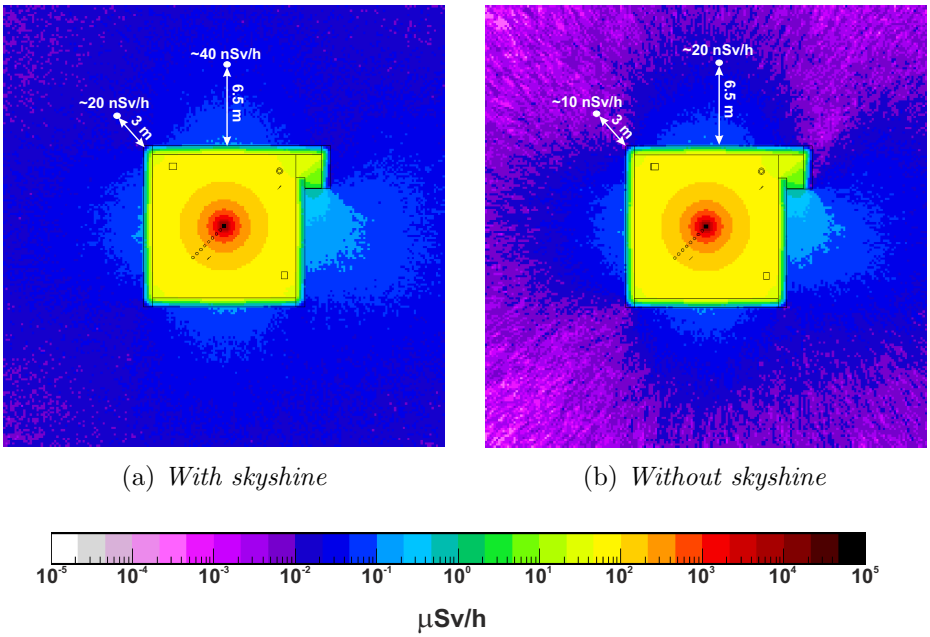

(a) *With skyshine* (b) *Without skyshine*

Figure 4.29: *Top view of the ambient dose equivalent rate caused by the Am-Be source. On the left side the results for the final shielding study (skyshine included), on the right side the results without skyshine.*

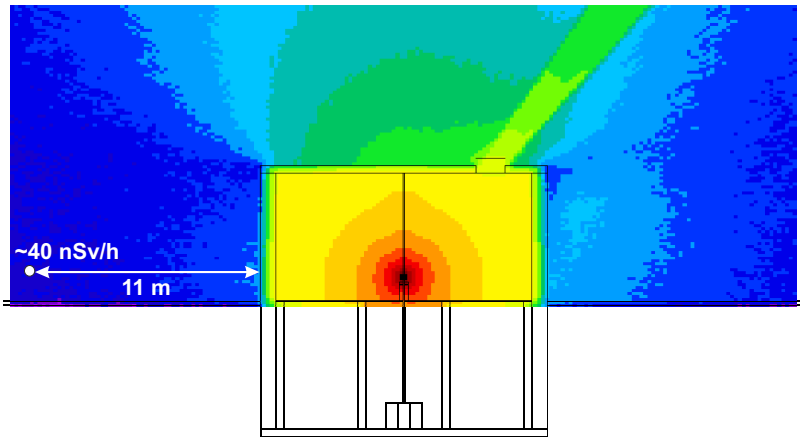

(a) *With skyshine*

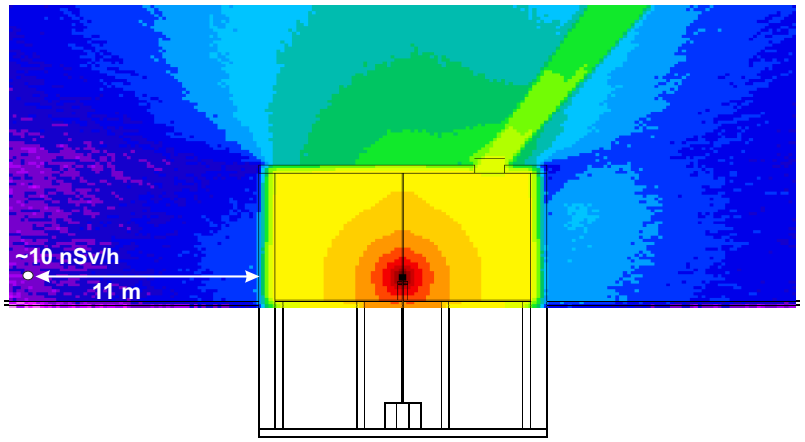

(b) *Without skyshine*

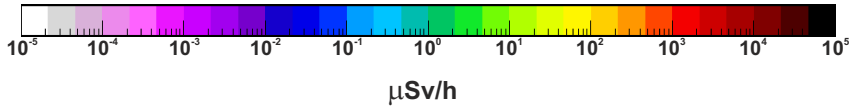

Figure 4.30: *Side view of the ambient dose equivalent rate caused by the Am-Be source. On the top the results for the final shielding study (skyshine included), on the bottom the results without skyshine.*

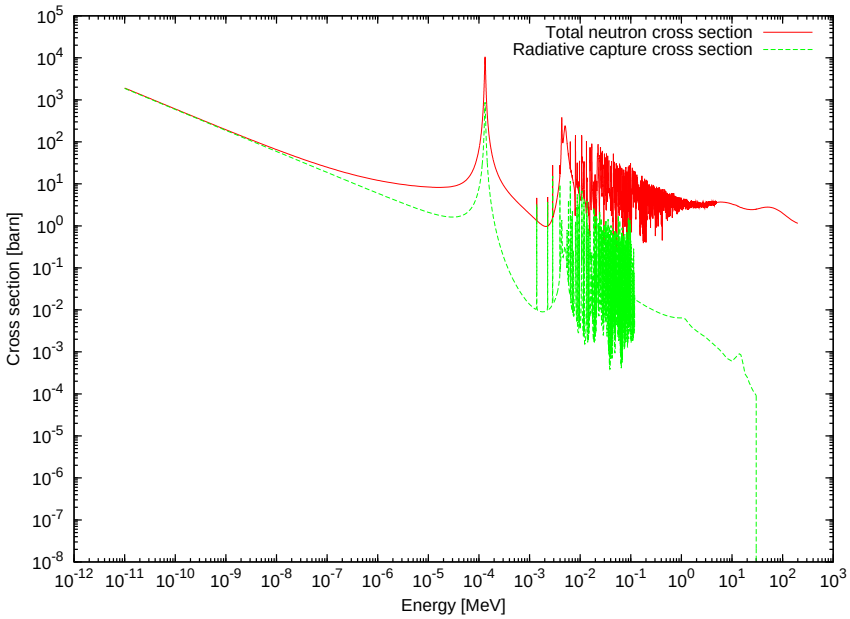

Figure 4.31: *Total and radiative capture neutron cross section for Co-59 [34].*

4.2.5 Concrete and air activation calculation

Neutron interaction with target material can lead to the production of unstable isotopes; the production rate depends on the neutron energy and flux. In the case of a neutron calibration source, such as the Am-Be source, the activation process is generally a negligible phenomenon since the spallation and radiative-capture cross-sections around 4 MeV are generally very low and the source emission rate is fairly small (less than 10^8 s^{-1}). For instance, Figure 4.31 shows the total and radiative capture neutron cross-sections for Co-59 isotope; the radiative capture on Co-59 leads to the production of Co-60. The cross-section value for 4 MeV neutrons is about 6 order of magnitude lower than that for thermal neutrons. Another example is given by Figure 4.32, which shows the total and spallation neutron cross-section for Al-27; the threshold of the reaction that leads to the production of Na-22 is above the maximum neutron energy of an Am-Be source.

Radiative capture is important on stable Europium, Cobalt and Cesium, which are present in concrete in concentrations of a few parts per million or less by weight. There are many other elements in concrete that become activated when irradiated by neutrons, but only a few of the resulting radioisotopes are long-lived, i.e. with an half-life more than 10 days. Even if the Am-Be neutron spectrum should not significantly activate the concrete and the air, a dedicated set of simulations was carried out to demonstrate that no specific measure in terms of radioactive

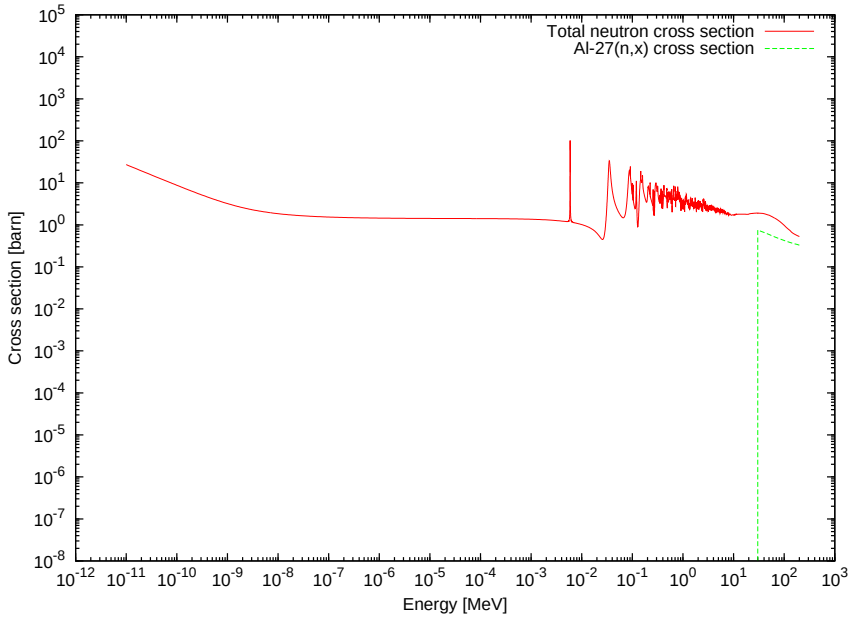

Figure 4.32: *Total Al-27 neutron cross section and Al-27(n,x) cross-section [34].*

waste or air filters have to be taken. The activity of the produced radionuclides was compared with the Swiss radiological exemption limits given in ref. [35]; any preventive measure shall not be taken if the ratio between the simulated activity and the relative limit (Exemption Limit or Air Contamination limit) is below 1.

The exemption limit (LE) applies to specific activities of solids and liquids; below the exemption limit, the ordinance is no longer applicable. The LE is defined as the specific activity of a certain object that, in case of ingestion of 1 kg of the substance, leads to a committed effective dose of 10 μSv. The air contamination (AC) limit is calculated so that one person, working the entire year (40 hours per week and 50 weeks per year, breathing 1.2 m^3 per hour) in air contaminated, receives a committed effective dose equal to the annual occupational dose limit, i.e. 20 mSv [35].

A FLUKA study was conducted by irradiating a sample of concrete 100x100 cm^2x 80 cm thick in order to evaluate the activation of concrete and the metal rods contained in the walls; three metal rods were inserted in the concrete according to Figure 4.33. The concrete chemical composition (Table 4.4) was not exactly the real one since an accurate analysis was too expensive and unjustified for the aim of this study. Therefore, a typical chemical composition of CERN concrete was considered. The chemical composition of the metal rods was provided by chemical measurements performed for other radioactive waste studies [36]. The real operation profile could not be defined *a priori* since it varies with the calibration needs

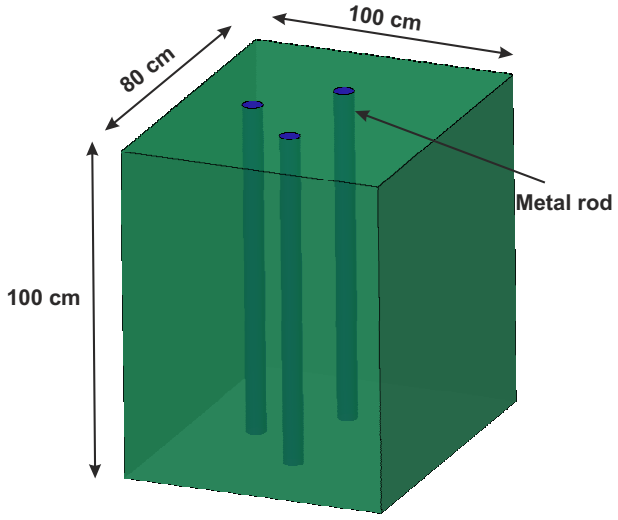

Figure 4.33: *Configuration of the concrete sample with the metal rods as simulated.*

and the user requests. However, it was conservatively assumed that the worst, but also unlikely, scenario is 20 years of continuous irradiation with the 1 TBq Am-Be source. The residual nuclei were scored after one month of cooling. EVAPORA-Tion and COALESCEnce options were activated in the PHYSICS card [37]. The H*(10) around the concrete sample was scored as well.

Figure 4.34 shows the ambient dose equivalent rate around the concrete sample after the 20 years of irradiation (cooling time = 0 seconds); the maximum of the H*(10) is found in the first 30 cm of concrete and it is below 0.5 μSv/h. At 10 cm from the surface of the sample the H*(10) is below 0.1 μSv/h, which is the dose limit indicated in ref. [35] for the disposal of a waste as non-radioactive. Tables 4.5 and 4.6 list the radionuclides produced after 20 years of irradiation and 1 month of cooling time, which was judged a reasonable waiting time before starting the facility decommissioning (only the radionuclides with an activity higher than 1 Bq are listed). The specific activity of each radionuclide (A_i) was compared with the respective exemption limit (LE_i) and the ratio is listed in each table. All the ratios are below 1, and therefore no specific measure has to be taken in order to avoid the production of radioactive waste for the calibration hall.

The simulations for the air activation were carried out assuming as the worst scenario an irradiation profile of one week since the air activation could have an impact in the short term. For this scenario, the H*(10) was scored after 0 s and 1 hour of cooling times. The residual nuclei were scored nearby the source after a cooling time of 0 s. It should be noted that the simulations did not take into account the routine air ventilation, which contributes to reducing the specific

Table 4.4: *Chemical compositions of the concrete sample and metallic rods. Data are in percentage of the total mass. Concrete density = 2.4 g/cm^3. Metallic rod density = 8.0 g/cm^3.*

Element	Concrete	Metallic rod
Mo	-	0.01702
Zr	-	0.005
Pb	-	0.01364
W	-	0.04432
Cu	-	0.3466
Ni	-	0.08426
Co	0.0001	0.00252
Fe	1.26	98.0
Mn	-	0.8944
Cr	-	0.1278
V	-	0.002
Ti	0.173	0.003
Ca	23.9	-
K	0.833	-
S	0.414	-
Ba	0.025	-
Cs	0.0001	-
O	48.2	-
Si	16.2	0.2392
H	10.0	-
C	4.38	0.2116
Al	2.11	0.002
Nb	-	0.003
Eu	0.0003	-
Mg	1.51	-
Na	0.446	-

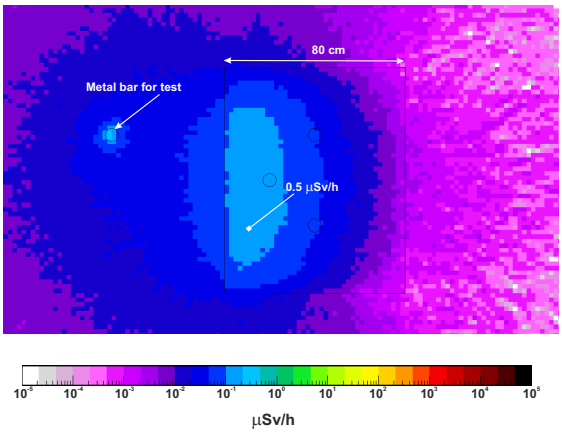

Figure 4.34: *Ambient dose equivalent rate around the concrete sample after 20 years of irradiation by the 1 TBq Am-Be source and 0 seconds of cooling. An additional metal rod close to the concrete sample was added to the simulations for testing.*

Table 4.5: *Residual activity in the concrete sample after 20 years of irradiation: M = 1900 kg, cooling time = 1 month. The error column represents the statistical uncertainty of the simulations results.*

Radionuclide			**Half-life**	$\mathbf{A}_i$	**Error**	$\mathbf{LE}_i$	$\mathbf{A}_i/\mathbf{LE}_i$
	A	Z		[Bq/kg]	%	[Bq/kg]	
Eu	154	63	4.96 y	$1.60{\cdot}10^{-1}$	1.4	$5.00{\cdot}10^{3}$	$3.20{\cdot}10^{-5}$
Eu	152	63	13.33 y	$2.34{\cdot}10^{0}$	0.3	$7.00{\cdot}10^{3}$	$3.35{\cdot}10^{-4}$
Cs	134	55	2.062 y	$2.12{\cdot}10^{-2}$	4.5	$5.00{\cdot}10^{2}$	$4.24{\cdot}10^{-5}$
Ba	133	56	10.74 y	$6.28{\cdot}10^{-4}$	23.6	$1.00{\cdot}10^{4}$	$6.28{\cdot}10^{-8}$
Cs	131	55	9.69 d	$1.00{\cdot}10^{-3}$	14.8	$2.00{\cdot}10^{5}$	$5.02{\cdot}10^{-9}$
Co	60	27	5.271 y	$3.11{\cdot}10^{-2}$	3.6	$1.00{\cdot}10^{3}$	$3.11{\cdot}10^{-5}$
Fe	59	26	44.529 d	$2.31{\cdot}10^{-2}$	3.1	$6.00{\cdot}10^{3}$	$3.84{\cdot}10^{-6}$
Fe	55	26	2.7 y	$1.33{\cdot}10^{0}$	0.6	$3.00{\cdot}10^{4}$	$4.44{\cdot}10^{-5}$
Mn	54	25	312.5 d	$1.99{\cdot}10^{-1}$	1.5	$1.00{\cdot}10^{4}$	$1.99{\cdot}10^{-5}$
Cr	51	24	27.704 d	$2.42{\cdot}10^{-3}$	8.5	$3.00{\cdot}10^{5}$	$8.06{\cdot}10^{-9}$
Sc	46	21	83.83 d	$8.45{\cdot}10^{-3}$	5.1	$7.00{\cdot}10^{3}$	$1.21{\cdot}10^{-6}$
Ca	45	20	163 d	$4.47{\cdot}10^{0}$	0.3	$1.00{\cdot}10^{4}$	$4.47{\cdot}10^{-4}$
Ca	41	20	1.4e5 y	$1.49{\cdot}10^{-2}$	0.1	$3.00{\cdot}10^{4}$	$4.97{\cdot}10^{-7}$
S	35	16	87.44 d	$4.40{\cdot}10^{-2}$	2.9	$1.00{\cdot}10^{4}$	$4.40{\cdot}10^{-6}$
P	33	15	25.4 d	$3.10{\cdot}10^{-3}$	8.8	$4.00{\cdot}10^{4}$	$7.75{\cdot}10^{-8}$
P	32	15	14.29 d	$3.53{\cdot}10^{-1}$	0.5	$4.00{\cdot}10^{3}$	$8.83{\cdot}10^{-5}$

Table 4.6: *Residual activity in one metal rod after 20 years of irradiation: M = 23 kg, cooling time = 1 month. The error column represents the statistical uncertainty of the simulations results.*

Radionuclide A	Z	**Half-life**	$\mathbf{A}_i$ [Bq/kg]	**Error** %	$\mathbf{LE}_i$ [Bq/kg]	$\mathbf{A}_i/\mathbf{LE}_i$
W 185	74	75.1 d	$1.59{\cdot}10^{-1}$	12.5	$2.00{\cdot}10^{4}$	$7.94{\cdot}10^{-6}$
Ni 63	28	96 y	$6.26{\cdot}10^{-2}$	7.7	$7.00{\cdot}10^{4}$	$8.94{\cdot}10^{-7}$
Co 60	27	5.271 y	$9.42{\cdot}10^{-1}$	3.6	$1.00{\cdot}10^{3}$	$9.42{\cdot}10^{-4}$
Fe 59	26	44.529 d	$1.99{\cdot}10^{0}$	3.1	$6.00{\cdot}10^{3}$	$3.31{\cdot}10^{-4}$
Co 58	27	70.80 d	$2.10{\cdot}10^{-1}$	11.5	$1.00{\cdot}10^{4}$	$2.10{\cdot}10^{-5}$
Fe 55	26	2.7 y	$1.03{\cdot}10^{2}$	0.6	$3.00{\cdot}10^{4}$	$3.43{\cdot}10^{-3}$
Mn 54	25	312.5 d	$1.96{\cdot}10^{1}$	1.5	$1.00{\cdot}10^{4}$	$1.96{\cdot}10^{-3}$
Cr 51	24	27.704 d	$6.19{\cdot}10^{-1}$	8.5	$3.00{\cdot}10^{5}$	$2.06{\cdot}10^{-6}$

Table 4.7: *Residual activity in the air of the calibration hall after 1 week of irradiation. Cooling time = 0 second. The error column represents the statistical uncertainty of the simulations results.*

Radionuclide A	Z	**Half-life**	$\mathbf{AC}_i$ Bq/m^3	$\mathbf{A}_i$ Bq/m^3	**Error** %	$\mathbf{A}_i/\mathbf{AC}_i$
Ar 41	18	109 min	$5{\cdot}10^{4}$	$4.46{\cdot}10^{0}$	26.0	$8.91{\cdot}10^{-5}$
C 14	6	5730 y	$1{\cdot}10^{6}$	$1.93{\cdot}10^{-2}$	0.6	$1.93{\cdot}10^{-8}$
H 1	3	12 y	$5{\cdot}10^{9}$	$1.25{\cdot}10^{0}$	1.5	$2.50{\cdot}10^{-10}$

activity in the hall. The same parameters used for the concrete activation study were employed.

Figure 4.35 shows the ambient dose equivalent rate maps for the two cooling times; the H*(10) generated by the air activation is completely negligible even immediately after one week of irradiation. Table 4.7 lists the produced radionuclides (cooling time of 0 s). The specific activity of each radionuclide was compared with the respective Swiss Air Contamination limit (AC). All the ratios are below 1, and therefore no specific measure has to be taken in terms of air release.

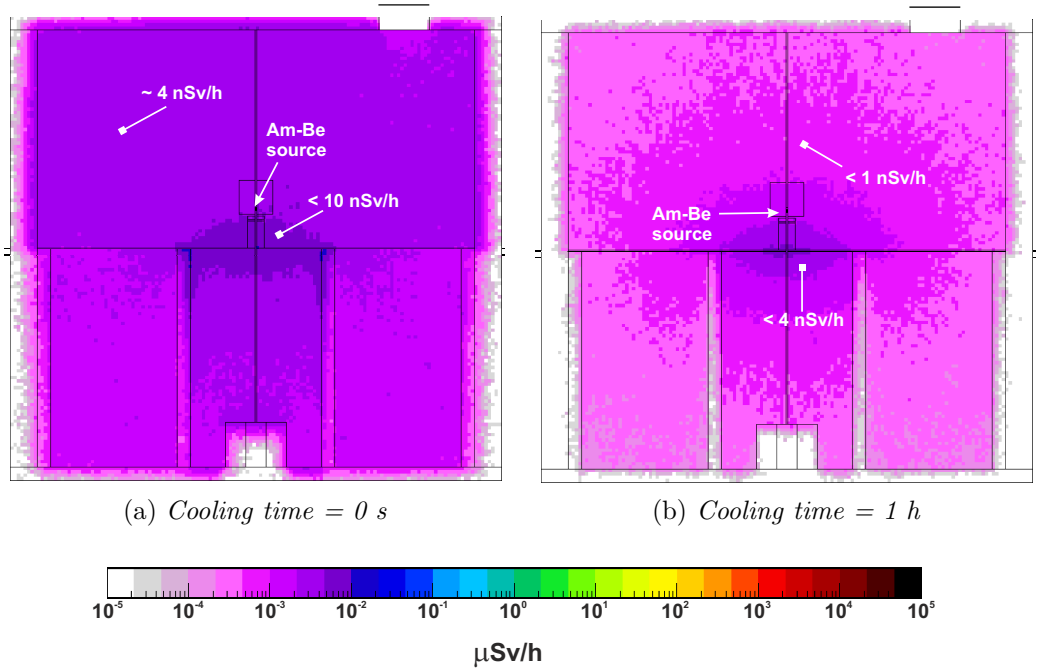

(a) *Cooling time = 0 s* (b) *Cooling time = 1 h*

Figure 4.35: *Side view of the ambient dose equivalent rate caused by the air activation for two cooling times. The planes are cutting at the source level.*

Table 4.8: *Ozone tolerance for humans based on 8 hours average concentrations [39].*

Concentration range	**Air quality descriptors**	**Cautionary statements for ozone**
0-0.059 ppm	Good	No health impacts are expected when air quality is in this range
0.060-0.075 ppm	Moderate	Unusually sensitive people should consider limiting prolonged outdoor exertion
0.076-0.095 ppm	Unhealthy for Sensitive Groups	Active children and adults, and people with respiratory disease, such as asthma, should limit prolonged outdoor exertion
0.096-0.115 ppm	Unhealthy	Active children and adults, and people with respiratory disease, such as asthma, should avoid prolonged outdoor exertion, everyone else, especially children should limit prolonged outdoor exertion
0.116-0.374 ppm	Very Unhealthy	Active children and adults, and people with respiratory disease, such as asthma, should avoid all outdoor exertion; everyone else, especially children, should limit outdoor exertion

4.2.6 Study of the ozone production in room 1

Ozone is an unstable, poisonous allotrope of oxygen, O_3, which is formed by an electrical discharge in oxygen. In the atmosphere ozone has a very low concentration; its concentration varies between 0.025 and 0.054 ppm in volume over the range 100-3500 m amsl[8] [38]. Table 4.8 provides information about ozone tolerance for humans based on 8 hours average concentration.

Ozone production in the atmosphere is given by Eq. 4.1, where $h\nu$ is a light quantum of wavelength between 170 and 210 nm [37].

$$O_2 + h\nu \rightarrow O_2^* \tag{4.1}$$

After the interaction, the oxygen molecule is in an excited state, O_2^*. Then the following chemical reactions occur:

$$O_2^* + O_2 \rightarrow O_3 + O; O + O_2 + M \rightarrow O_3 + (M) \tag{4.2}$$

where M is a third molecular type, e.g. N_2, which absorbs a part of the energy

[8]amsl = above mean sea level.

released by the reaction and stabilizes produced ozone. The ozone decomposition in oxygen is fairly slow at the ambient temperature. This process is faster if the temperature increases. Most of the metals, except gold and platinum, are damaged by ozone. Stainless steel and aluminium can however resist its corrosive action. Ozone can also be produced by ionizing radiation and therefore its production by the Co-60 source of room 1 was investigated. At the ambient temperature the ozone decomposition via chemical reactions occurs together with the production induced by ionizing radiation. If the room is ventilated, ozone is removed proportionally to the ventilation rate. The production and dissociation of ozone is given by Eq. 4.3 [37]:

$$\frac{dN}{dt} = IG - \alpha N - kIN - \frac{Q}{V}N \tag{4.3}$$

where:

- $\frac{dN}{dt}$ is the production or dissociation rate in cm^{-3} s^{-1};
- I is the ionizing energy density deposited in air per time unit in eV cm^{-3} s^{-1};
- G is the number of produced ozone molecules in eV^{-1};
- α is the ozone dissociation constant in s^{-1};
- N is the ozone concentration at time t in cm^{-3};
- K is the decomposition constant in eV^{-1} cm^{-3} due to the photon interaction with ozone;
- Q is the ventilation rate in cm^{-3} s^{-1};
- V is the irradiated volume in cm^{-3}.

The integration of Eq. 4.3 gives:

$$N(t) = \frac{IG}{\alpha + kI + \frac{Q}{V}}(1 - e^{-[\alpha + kI + \frac{Q}{V}]t}) \tag{4.4}$$

The G value, which is generally expressed in number of molecules produced per 100 eV of deposited energy, for the ozone production in the air strongly varies in the literature. In most of the investigations where high dose rates were employed, there was usually a period when ozone formation was directly proportional to absorbed radiation; hence, secondary reactions, such as thermal and radiation-induced decomposition reactions or reactions between ozone and other gases, had a negligible effect, and the ozone concentration-dose curve was linear. For total

dose below 10^4 Sv ref. [40] concluded that the minimum G was 9; the latest was assumed in this study. The dissociation constant was measured for closed systems and lies between $4.1{\cdot}10^{-4}$ and $6.3{\cdot}10^{-4}$ s^{-1}, which correspond to a dissociation time between 26 and 41 minutes. The constant is strongly influenced by the ambient conditions, such as the temperature, humidity and the characteristics of the surface with which ozone can interact. An extreme value of 50 minutes was measured in an electron linear accelerator. Therefore, it was conservatively assumed a value of $2.3{\cdot}10^{-4}$ s^{-1} according to ref. [37]. The decomposition constant was assumed to be $1.4{\cdot}10^{-16}$ eV^{-1} cm^{-3} from ref. [37]. The ionizing energy density deposited in air by the photons of the Co-60 source can be estimated via MC simulations and included in Eq.4.4 to obtain the ozone concentration.

In order to validate the above-described methodology, the data obtained from ref. [41] were compared with results from MC simulations. Kertesz and Parsons [41] measured the amount of ozone formed in air exposed to a 148 TBq Co-60 source in various exposure conditions. The first set of measurements was performed at 1 m from the source, where the H*(10) was 31.83 Sv/h. It is worth noting that an analytical calculation performed with Nucleonica [32] gives an H*(10) at 1 m of 49.80 Sv/h for the same source; this is about 56% higher than that reported in the article. At 1 m distance they measured an ozone concentration of 0.093 ppm after 2 hours of irradiation and 0.116 ppm after 18 hours. Subsequent determinations during the following 6 hours showed no further increase in the ozone content. The second set of measurements was carried out by irradiating glass containers 330 ml in volume at different dose rates for several exposure times. The values are summarized in Table 4.9 and in Figure 4.36.

To obtain the energy density deposited in air and thus the ozone concentration, a Co-60 source was simulated with FLUKA in an air sphere 300 cm in diameter; the energy deposition was scored at several distances from the source according to ref. [41], i.e. 7, 12, 50, 70 and 100 cm. Electrons and photons were both tracked down to 1 keV. It was conservatively assumed that all energy loss in air was ionizing; the air density was assumed equal to 0.0012 g/cm^{-3} giving a concentration of $2.50{\cdot}10^{19}$ atoms per cm^3.

Table 4.9 and Figure 4.36 show the comparison of the results from ref. [41] and the simulated ones. MC predictions generally overestimate the ozone concentration. The simulation results at 100 cm from the source overestimates of about a factor 30 the measurements. This is partially explained by the fact that the scoring volume was not known from ref. [41]; in the simulations, the volume was assumed to be 330 ml, according to the subsequent measurements. The overestimation is between a factor 2 and 4 for the other measurements for which the scoring volume was known. This difference is due to factors that cannot take into account in this methodology:

Table 4.9: *Comparison of the ozone concentration from ref. [41] and FLUKA simulations.*

Dose rate [Sv/h]	**Source-detector distance [cm]**	**Irradiation time [h]**	**Ozone concentration [ppm]** Kertesz	FLUKA
31.83	100	2	0.093	2.67±0.20
31.83	100	18	0.116	3.15±0.24
100	70	1	1.60	3.03±0.17
200	50	2	4.85	17.60±0.41
3460	12	5	11.13	25.70±0.26
10000	7	19	7.75	25.70±0.26

- temperature strongly influences the radiation yield of ozone since secondary reactions are temperature-dependent;
- the ozone concentration is function of the dose rate and the relationship is well marked at temperatures lower than ambient temperature;
- the presence of NO_2 strongly influences the the ozone concentration;
- the size, composition and surface of the walls of the container used for the ozone measurement can reduce the final ozone concentration.

Even though this methodology does not estimate the ozone concentration with high accuracy, it provides an early conservative evaluation. Therefore, this evaluation was performed during the preliminary study to understand if ozone could be a safety issue for the room 1. The energy deposition of the photons emitted by the 10 TBq Co-60 source was calculated via FLUKA simulations; for simplicity, the ventilation was not included in Eq. 4.4, even though it is present in the room. The same parameters of the previous set of simulations were employed, except the source activity, which was set to 10 TBq. The energy density deposited in air was scored in the entire room 1 and in cubes of 8000 cm^3 in volume at 1, 2 and 3 m from the source.

Table 4.10 lists the ozone concentration at saturation, i.e. at 96.9% of the maximum concentration, which is reached after 251 minutes. As expected, the ozone concentration is higher next to the source, i.e. at 100 cm. In order to understand if any specific measure had to be taken, the ozone concentration in the entire room was considered. This is 0.006 ppm, which is about one order of magnitude less than the values for the ozone concentration at ground level. Hence, it was concluded that no measures concerning ozone had to be foreseen for room 1.

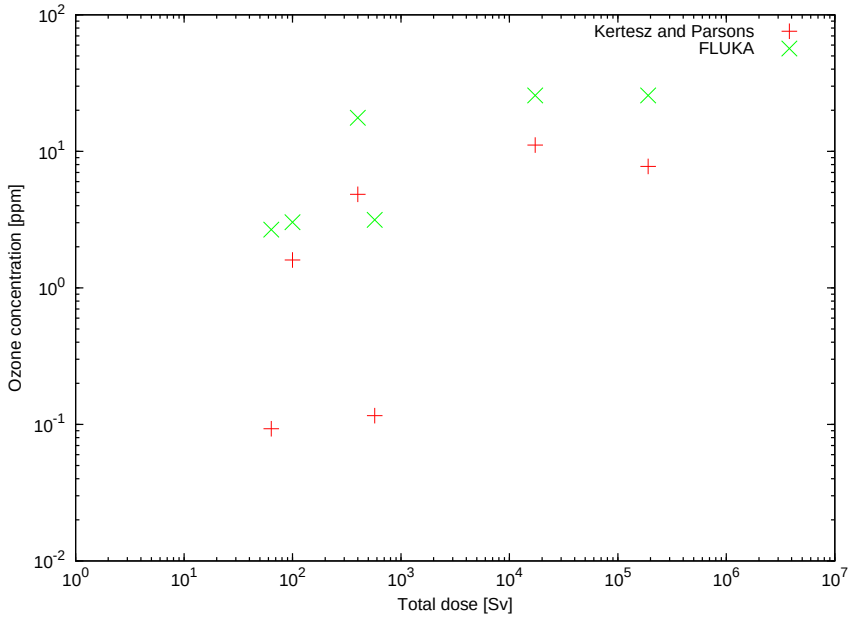

Figure 4.36: *Ozone concentration as a function of the total dose for Kertesz [41] and FLUKA simulations.*

It should be noted that the ventilation significantly reduces the estimated value, which is already a conservative estimate.

Table 4.10: *Ozone concentration for the irradiation room 1 at different locations.*

Position	**Ozone concentration [ppm]**
Room	0.006±0.00006
100 cm	0.064±0.00173
200 cm	0.016±0.00082
300 cm	0.008±0.00062

4.2.7 Radiation protection measurements

After the source installation several measurements were performed to verify the compliance with the RP area classification (Section 4.2.1) and to validate the FLUKA results shown in Sections 4.2.2 and 4.2.3. The H*(10) was measured in several laboratory positions:

- entrance door: H*(10) measured just outside the 5 cm polyethylene door (the complete door surface was checked);
- outdoor: H*(10) measured in the proximity of the laboratory walls;
- roof: H*(10) measured on the roof of the calibration hall/the irradiation room 1 (depending on the source);
- window: H*(10) measured above the smoke extraction aperture of the calibration hall.

It is worth remembering that for the roof area the RP limits were not defined since this area is not accessible during irradiation; however, the ALARA (As Low As Reasonably Achievable) recommendation was taken into account.

Table 4.11 shows the comparison between the FLUKA calculations and the RP measurements performed for the 888 GBq Am-Be source. The calculations of Section 4.2.2 were corrected for the real source activity, i.e. 888 GBq, and therefore for the neutron emission rate provided by the source manufacturer, i.e. $5.03 \cdot 10^7$ s^{-1}. The neutron measurements were performed only for the source of highest activity with the LB6411 rem-counter. It should be noted that instead of taking the average value over the measurements, it was conservatively assumed that the maximum measured H*(10) was adequate for this purpose; therefore, the standard deviation is not provided.

Table 4.12 shows the comparison between the FLUKA calculations and RP measurements for the 3 TBq Cs-137 source carried out with the Automess AD-6 detector (a standard survey instrument used at CERN).

Table 4.13 shows the comparison between the FLUKA calculations and the RP measurements for the 11.8 TBq Co-60 source of irradiation room 1. The calculations of Section 4.2.3 were corrected for the real source activity. The measurements were carried out with an Automess AD-6 detector.

All the measurements are confirming that the RP area classification was fully respected. FLUKA generally overestimates the H*(10) between a factor 1.3 for the photon sources up to a factor 3 for the Am-Be. The overestimation can be mainly explained by the two following aspects.

Table 4.11: *Maximum neutron ambient dose equivalent rates for the 888 GBq Am-Be source at several locations (FLUKA calculations and in situ measurements). $FLUKA_{corr}$ = FLUKA calculations corrected for the real source activity; n.d. = not defined.*

Position	**RP limit** [μSv/h]	**FLUKA** [μSv/h]	**FLUKA$_{corr}$** [μSv/h]	**Experimental** [μSv/h]
Entrance door	3.0	2.0	1.2	0.4
Outdoor	0.5	0.2	0.1	0.1
Roof	n.d.	4.5	2.8	1.0
Window	n.d.	45.0	27.6	9.0

Table 4.12: *Maximum photon ambient dose equivalent rates for the 3 TBq Cs-137 source at several locations (FLUKA calculations and in situ measurements). Bg = background; n.d. = not defined.*

Position	**RP limit** [μSv/h]	**FLUKA** [μSv/h]	**Experimental** [μSv/h]
Entrance door	3.0	0.4	0.3
Outdoor	0.5	0.02	bg
Roof	n.d.	0.10	bg
Window	n.d.	10.0	3.0

Table 4.13: *Maximum photon ambient dose equivalent rates for the 11.8 TBq Co-60 source at several locations (FLUKA calculations and in situ measurements). Bg = background, $FLUKA_{corr}$ = FLUKA calculations corrected for the real source activity; n.d. = not defined.*

Position	**RP limit** [μSv/h]	**FLUKA** [μSv/h]	**FLUKA$_{corr}$** [μSv/h]	**Experimental** [μSv/h]
Entrance door	3.0	2.0	2.4	2.5
Outdoor	0.5	$<$ bg	$<$bg	0.2
Roof	n.d.	150.0	177.0	20

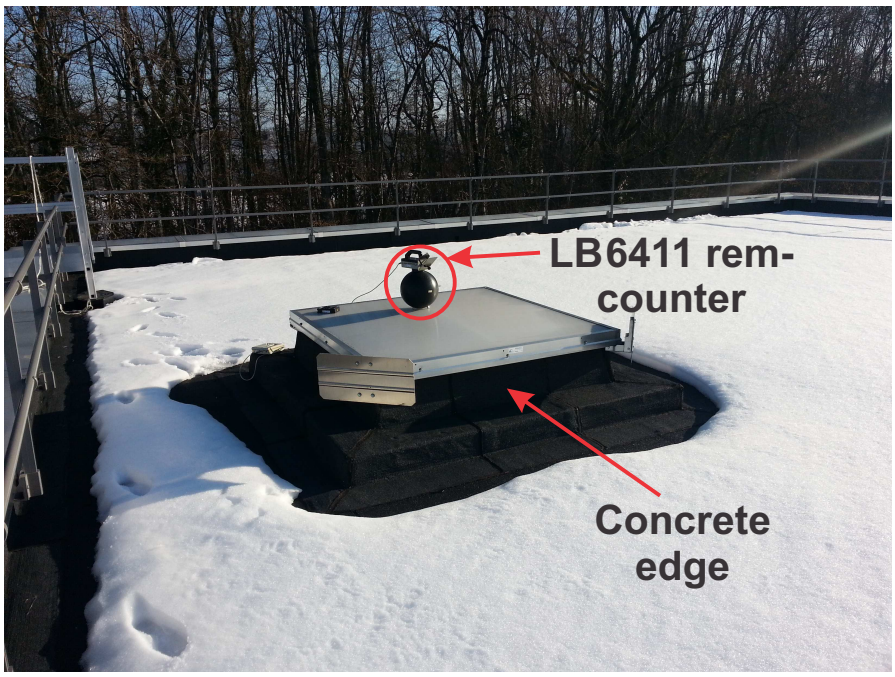

Figure 4.37: *The window on the roof of the calibration hall.*

- Geometry approximations: the window on the roof was modelled as an aperture, without taking into account its edges, which create an additional shielding (Figure 4.37). Then, the padding 20 cm thick all around the laboratory made by mineral wool and stainless steel was not simulated. Concerning the H*(10) on the roof of room 1, the difference could be due to the modelization of the irradiator collimator that included some uncertainties.

- Material chemical composition: for some materials, e.g. concrete, the chemical composition can be of a quite importance; this is particulary true for neutron shielding calculations. In the shielding simulations for simplicity the FLUKA standard concrete was considered.

4.3 Scattered neutron study

This section describes the MC studies performed to minimize the scattered neutron contribution and investigate its origin and weight. For the sake of simplicity, the following abbreviations are used:

- H*(10): total H*(10), which is the sum of the direct source contribution and the scattering one;
- $H^*(10)_{unscat}$: unscattered H*(10), which does not include the scattered neutron contribution;
- $H^*(10)_{scat}$: the scattered H*(10), which takes into account only the scattered neutron contribution.
- $H^*(10)_{obj}$: the H*(10) caused by a specific scattering object, e.g. walls.

4.3.1 Scattered neutron problem

The response or calibration factor of a device is a unique characteristic of the type of device, and may depend on the dose equivalent rate, the spectrum of the neutron source or the angle of incidence of the neutrons, but should not be a function of the characteristics of the calibration facility or experimental techniques employed [30]. To perform a calibration, the instrument has to be placed in a radiation field of known free-field fluence rate and the instrument reading is recorded. The reading should be corrected for all extraneous neutron scattering effects, including neutron scattering by the air and by the walls, floor, and ceiling of the calibration room. It may also have to be corrected for effects due to the source or detector size. The following scattering effects may occur.

- Room scatter: neutrons are scattered by the floor, walls and ceiling of the calibration room in a complex way. Their contribution to the reading of a device can be determined by MC codes or by measurements for specific laboratory conditions. Room scatter is likely to be the most important source of scattered neutrons.
- Air attenuation (air out-scatter): neutrons emitted by the source are attenuated by nuclear reactions with the air. The air attenuation increases approximately as a function of the source-to-detector distance.
- Air in-scatter: neutrons from outside the direct source-detector distance path are scattered by the air and may be detected by the device under test.

Table 4.14: *Minimum room lengths (in metres) for 40% room return (l_c = 75 cm).*

Source	**^{252}Cf+D_2O**	**^{252}Cf**	**Am-Be or Am-B**
Small sphere or albedo dosimeter	4.2	7.5	8.2
Large sphere or survey meter	3.0	3.0	3.0

The relative in-scatter also increases approximately linearly with source-to-detector distance. The relative magnitude of room scatter, air in-scatter and air out-scatter depends upon the size of the room and the separation distance between the neutron source and the device to be calibrated. In all cases, their effect in a calibration can be reduced by minimizing this distance.

- Scattering from support structures: support structures should be as light as is reasonably possible, with little or no hydrogenous materials. Special care should be taken to minimize the mass of support structure nearest the source or detector [30]. This contribution can be quite important for source-to-detector distances less than 100 cm.

For all scatter contributions, the spectral and angular distribution is different from that of the original source spectrum. Thus, the relative contribution of scattered radiation to the reading of the device is dependent upon the energy and angular dependence of the device response function. In addition, it should be noted that in any case the scatter contributions should not increase the instrument reading of more than 40% at the calibration point. The ISO 8529-2 [30] provides recommendations about the room size, which will give approximately 40% room return for each of the ISO-recommended radioactive neutron sources for a source-to-detector distance l_c = 75 cm. Values for two types of instruments are given: typical albedo dosimeters or small (5.1 cm or 7.6 cm) Bonner spheres, and typical neutron survey meters or large (20.3 cm or 25.4 cm) Bonner spheres. The values mentioned in Table 4.14 are valid for a cubical room [length (L) = width (W) = height (H)].

In order to evaluate the scattered neutron contribution, ref. [30] recommends four methods: the shadow cone method, the generalized fit method, the semi-empirical method and the reducing-fitting method. It also recommends checking the chosen method against one of the others. Taking into account the limitations of each method (see ref. [30] for the detailed explanation the methods) and the complexity of this problem, the radiation transport codes are very useful tools. These codes allow effects, which are impossible or too complicated to be evaluated during a real calibration, to be studied; for instance, the origin and the weight of

scattered neutrons can be assessed. Simulations can also help in designing and optimizing the required set of shadow-cones. Moreover, it is possible to evaluate the homogeneity of the radiation field at a specific source-to-detector distance. However, there are several parameters that can influence the accuracy of the simulated results:

- the geometry: it needs to be modeled as close as possible to the reality, even if some approximations can be done;
- the materials: each geometrical element has to be simulated with its real chemical composition;
- the source spectrum and homogeneity: they need to be known with precision;
- the physical models: they need to be appropriate for the considered problem.

It is essential to benchmark simulated results with real measurements since these parameters are not always known with high accuracy and therefore some approximations have to be taken.

4.3.2 Monte Carlo approximation

To minimize the scattered neutron component, the floor on which the calibration instrumentation lies, was located at the half-height of the room, i.e. at 6.5 m from the very bottom of the calibration hall. This choice was validated via MC simulations, evaluating the contribution of scattered neutrons when the floor was made of concrete or composed of a stainless steel grid (see next section). Before showing the results of this comparison, it is worth describing an approximation of the geometry assumed in the FLUKA calculations. The FLUKA code allows a mesh grid to be implemented via the use of the LATTICE card; this allows repetitive structures to be described not in all details. Only one single module has to be described and then can be repeated as many times as needed. This repetition does not occur at input stage but is hard-wired into the geometry package, namely repeated regions are not set up in memory, but the given symmetry is exploited at tracking time using the minimum amount of bodies/regions required [14]. Though this function is very powerful, the LATTICE implementation could be fairly time-consuming for the user and in terms of CPU memory. For instance, the LATTICE description is convenient when reproducing a particle accelerator, which is made by quite complex structures constantly repeated along a ring or a straight line.

Instead of reproducing in details the meshes of the grid along the 13 x 13 m^2 floor, it was evaluated the option of simulating a floor made by a 13 x 13 m^2 stainless steel layer having the thickness such that the weight of the slab was the

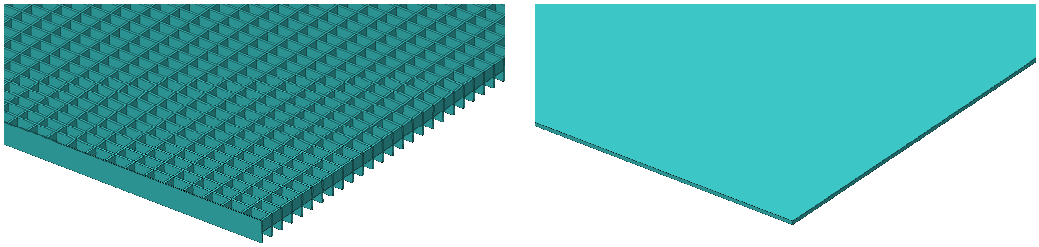

(a) *Grid floor* (b) *Layer floor*

Figure 4.38: *Detail of the two floors.*

same of the metal grid. For each floor an Am-Be source at 120 cm above the floor was simulated. The floor (Figure 4.38) sizes are the following:

1. stainless steel grid floor, from now on "grid floor", with a surface of 829.4 x 987 cm^2, similar to the one that was installed in the calibration hall;

2. stainless steel layer, from now-on "layer floor", 829.4 x 987 cm^2 x 0.62 cm.

The total weight of the structure in both cases was 4054 kg. The neutron H*(10) was scored via several USRTRACK cards from 10 cm up to 360 cm from the source.

Table 4.15 lists the results expressed in pSv per primary particle. Figure 4.39 shows the ratio of the H*(10) obtained with the grid floor and the layer floor. The ratio is always close to one; the statistical uncertainties are too high to conclude any trend. To validate the approximation, the neutron spectral fluences were compared. Figure 4.40 shows the neutron spectral fluence comparison for two source-to-detector distances, i.e. 60 and 180 cm. One can conclude that neither the H*(10) nor the neutron spectrum depend on the floor approximation and therefore the layer floor approximation was validated.

Table 4.15: *H*(10) as function of the source-to-detector distance for the grid and layer floor.*

Source-to-detector distance [cm]	**H*(10) [pSv/pr]** Grid floor	Layer floor
10	$3.04{\cdot}10^{-1}{\pm}6.74{\cdot}10^{-5}$	$3.04{\cdot}10^{-1}{\pm}7.05{\cdot}10^{-5}$
30	$3.47{\cdot}10^{-2}{\pm}2.43{\cdot}10^{-5}$	$3.47{\cdot}10^{-2}{\pm}2.37{\cdot}10^{-5}$
60	$8.75{\cdot}10^{-3}{\pm}1.17{\cdot}10^{-5}$	$8.74{\cdot}10^{-3}{\pm}1.05{\cdot}10^{-5}$
90	$3.95{\cdot}10^{-3}{\pm}7.88{\cdot}10^{-6}$	$3.94{\cdot}10^{-3}{\pm}7.49{\cdot}10^{-6}$
120	$2.24{\cdot}10^{-3}{\pm}5.73{\cdot}10^{-6}$	$2.24{\cdot}10^{-3}{\pm}5.37{\cdot}10^{-6}$
150	$1.45{\cdot}10^{-3}{\pm}4.47{\cdot}10^{-6}$	$1.44{\cdot}10^{-3}{\pm}4.32{\cdot}10^{-5}$
180	$1.01{\cdot}10^{-3}{\pm}3.96{\cdot}10^{-6}$	$1.00{\cdot}10^{-3}{\pm}4.02{\cdot}10^{-6}$
210	$7.46{\cdot}10^{-4}{\pm}3.44{\cdot}10^{-6}$	$7.42{\cdot}10^{-4}{\pm}3.19{\cdot}10^{-6}$
240	$5.80{\cdot}10^{-4}{\pm}3.15{\cdot}10^{-6}$	$5.81{\cdot}10^{-4}{\pm}2.79{\cdot}10^{-6}$
270	$4.66{\cdot}10^{-4}{\pm}2.81{\cdot}10^{-6}$	$4.64{\cdot}10^{-4}{\pm}2.51{\cdot}10^{-6}$
300	$3.80{\cdot}10^{-4}{\pm}2.43{\cdot}10^{-6}$	$3.79{\cdot}10^{-4}{\pm}2.43{\cdot}10^{-6}$
330	$3.15{\cdot}10^{-4}{\pm}2.18{\cdot}10^{-6}$	$3.15{\cdot}10^{-4}{\pm}2.18{\cdot}10^{-6}$
360	$2.64{\cdot}10^{-4}{\pm}2.02{\cdot}10^{-6}$	$2.67{\cdot}10^{-4}{\pm}2.06{\cdot}10^{-6}$

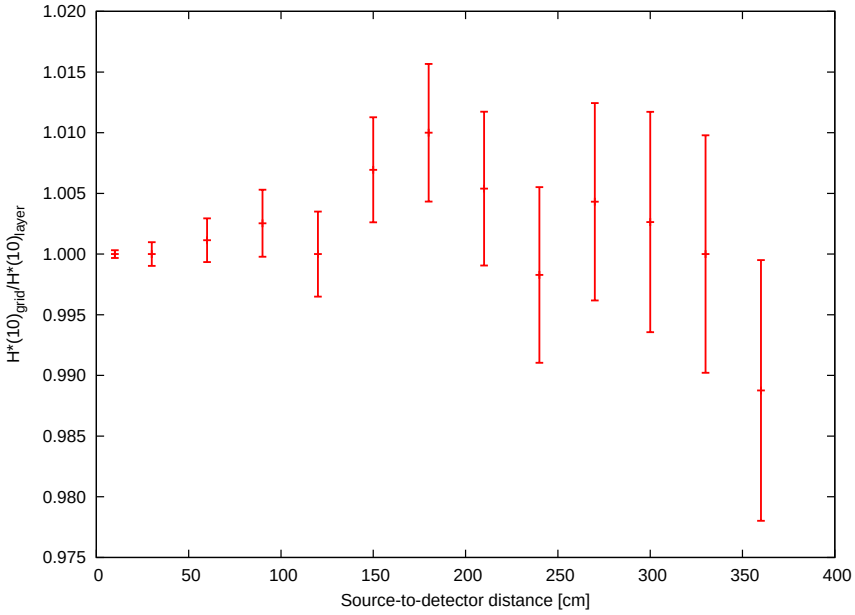

Figure 4.39: *Ratio of the H*(10) for the grid floor and the H*(10) for the layer floor as function of the source-to-detector distance.*

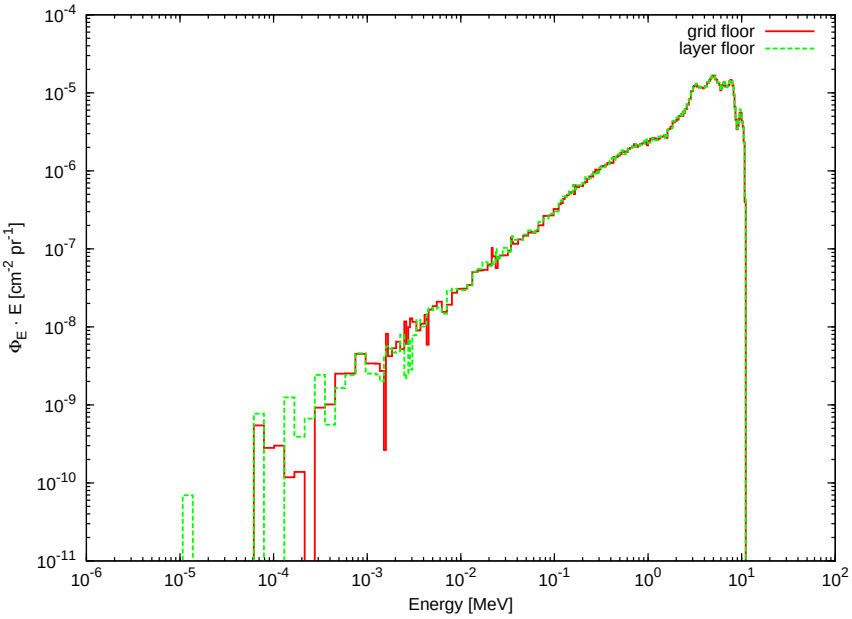

(a) *Source-to-detector: 60 cm*

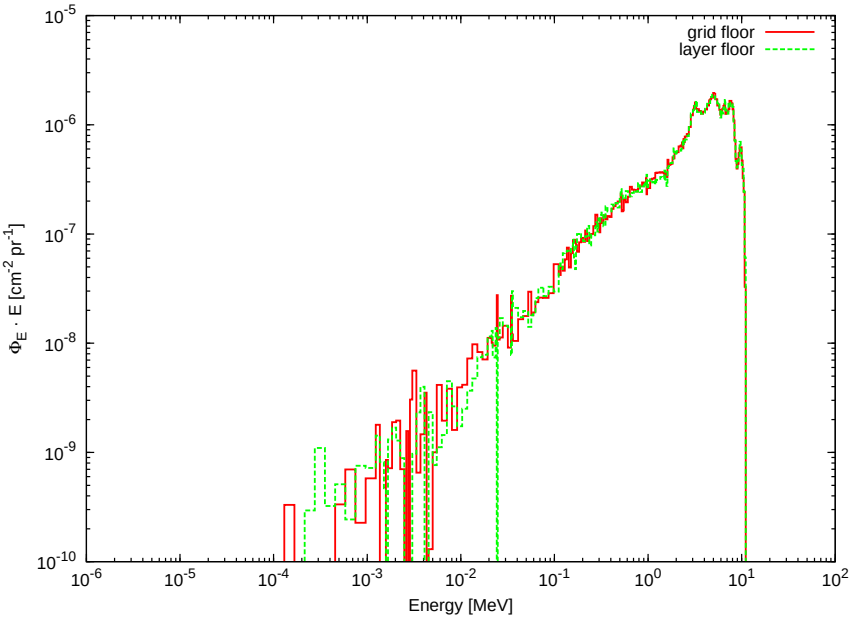

(b) *Source-to-detector: 180 cm*

Figure 4.40: *Neutron spectral fluence for the grid floor and layer floor simulations. The spikes at low neutron energies are due to poor statistics.*

Table 4.16: *H*(10) results for the concrete floor and for the stainless steel layer floor.*

	Source-to-detector distance [cm]	H*(10) [pSv/pr]
Layer floor	150	$1.82 \cdot 10^{-3} \pm 1.27 \cdot 10^{-5}$
Concrete floor	150	$1.96 \cdot 10^{-3} \pm 5.87 \cdot 10^{-6}$

4.3.3 Concrete or metal grid floor?

Since the floor of a calibration hall can be an important cause of neutron scattering, two kinds of floor were compared in order to choiche the configuration minimizing the scattered neutron contribution.

1. A 13 x 13 x 13 m^3 calibration hall (Figure 4.41) was simulated with the floor made of a stainless steel layer 0.62 cm thick, approximating the metal grid. The Am-Be source was located in the geometrical centre of the room at 120 cm above the layer.

2. A 13 x 13 x 6.5 m^3 calibration hall (Figure 4.41) was simulated with the floor made of concrete. The Am-Be source was located in the geometrical centre of the room at 120 cm above the floor.

The H*(10) at 150 cm from the source was assessed via the USRTRACK card as well as the neutron spectral fluence. Table 4.16 lists the H*(10) for the two geometries; the concrete floor causes a total H*(10) increase of about 7% at the calibration position. The comparison between the neutron spectral fluences (Figure 4.42) shows that the concrete floor results in an increase of the thermal and epithermal part of the neutron spectrum; this has a consequence that the 40% reading increase would be reached much closer to the source than the layer floor for detectors with response function peaking at low neutron energies and thus positions at larger distances could not be used. It is possible to conclude that a metal grid floor reduces sensitively the scattered neutron contribution and allows more calibration positions to be used than a concrete floor.

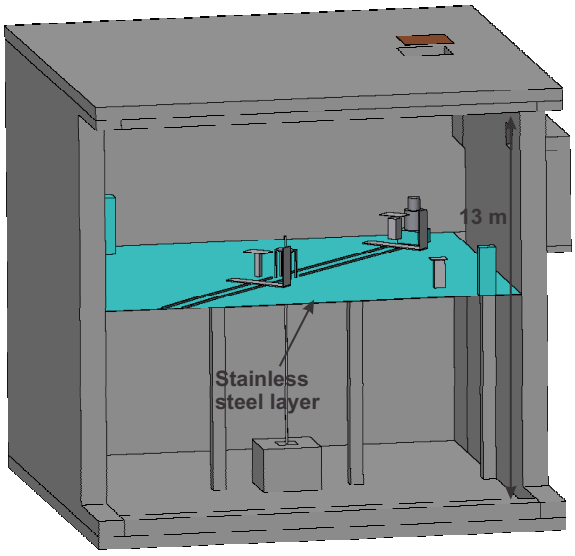

(a) *Layer floor*

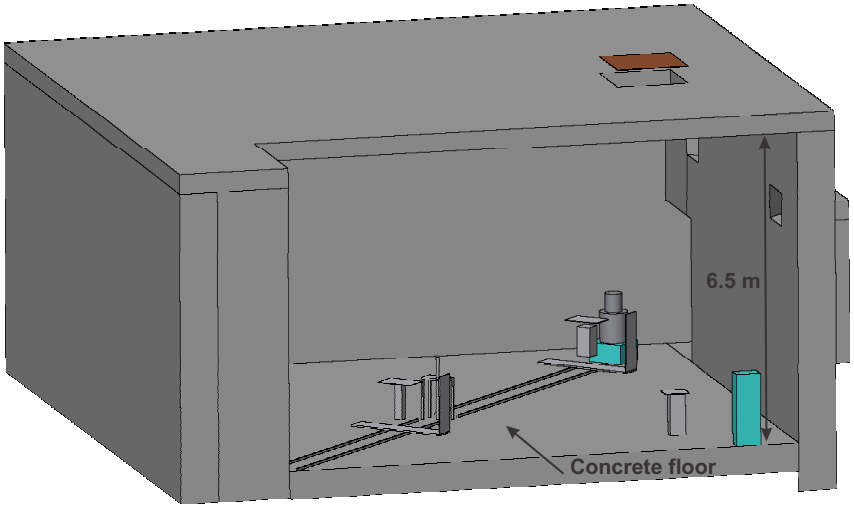

(b) *Concrete floor*

Figure 4.41: *Cross-sectional view of the calibration hall geometries.*

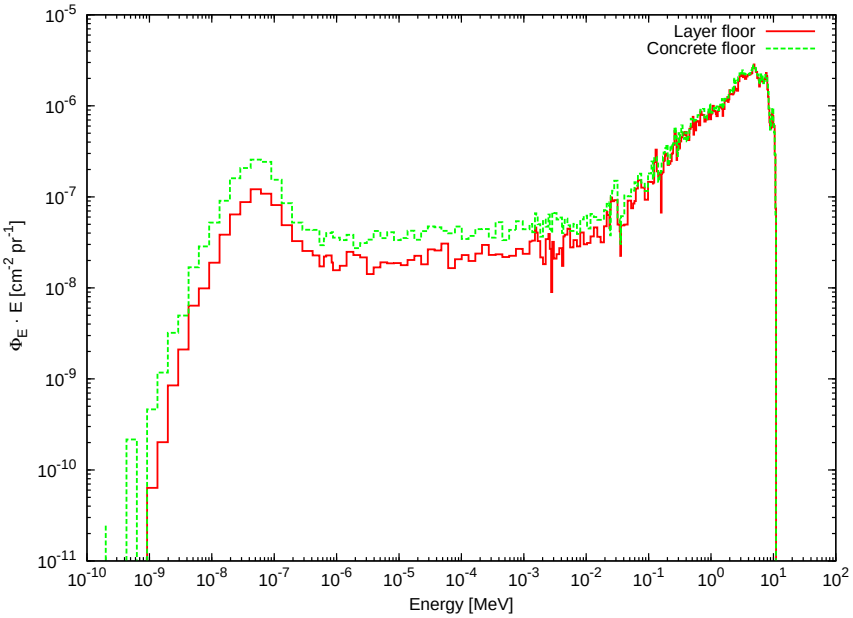

Figure 4.42: *Neutron spectral fluence at 150 cm from the Am-Be for the concrete floor and the layer floor.*

4.3.4 Scattered neutron weight and origin

As already mentioned, to perform accredited neutron calibrations, one has to define the positions for which the scattered neutron contribution does not increase more than 40% the instrument reading. For this purpose the following FLUKA studies were performed.

1. The H*(10)$_{unscat}$, the H*(10) and neutron spectral fluences from 40 to 300 cm from the Am-Be source were simulated. Then, the increase of the H*(10)$_{unscat}$, i.e. ΔH*(10) (Eq. 4.5), caused by scattered neutrons was determined at several calibration positions to define the appropriate distances (ISO approved) for H*(10) calibrations.

$$\Delta H^*(10) = \frac{H^*(10) - H^*(10)_{unscat}}{H^*(10)_{unscat}} \tag{4.5}$$

2. The increase of the reading caused by scattered neutrons was determined for the Bonner Sphere Spectrometer (BSS) at several calibration positions to define the appropriate calibration distances for testing the response matrix.

3. The scattered neutron contribution within the calibration hall was investigated.

Table 4.17: *H*(10)$_{unscat}$, H*(10) and ΔH*(10) as a function of the source-to-detector distance. The uncertainties are not listed since they are less than 1%.*

Source-to-detector distance [cm]	**H*(10)$_{unscat}$** pSv/pr	**H*(10)** pSv/pr	**ΔH*(10)**
40	$1.94 \cdot 10^{-2}$	$2.21 \cdot 10^{-2}$	14%
100	$3.11 \cdot 10^{-3}$	$3.71 \cdot 10^{-3}$	19%
150	$1.38 \cdot 10^{-3}$	$1.73 \cdot 10^{-3}$	25%
200	$7.78 \cdot 10^{-4}$	$1.04 \cdot 10^{-3}$	33%
250	$4.98 \cdot 10^{-4}$	$7.28 \cdot 10^{-4}$	46%
300	$3.46 \cdot 10^{-4}$	$5.43 \cdot 10^{-4}$	57%

One simulation was run for each calibration position to take into account the scattering of the calibration transport system, which was moved accordingly. Figure 4.43 shows the geometry of the calibration hall modelled in the simulations. The H*(10) and the neutron spectra were scored via the USTRACK cards.

Table 4.17 and Figure 4.44 show the H*(10)$_{unscat}$ and the H*(10) as a function of the source-to-detector distance. Scattered neutrons increase the H*(10)$_{unscat}$ more than 40% beyond about 230 cm from the source. Therefore, calibrations in H*(10) must be performed at source-to-detector distances less than 230 cm. Figure 4.45 shows the neutron spectral fluence for two source-to-detector distances. The contribution of thermal and epi-thermal neutrons, which are not present in the unscattered Am-Be spectrum, increases with the source-to-detector distance; for instance the thermal peak is about 2.5 order of magnitdue less than the 4 MeV peak at 40 cm and it is about 1 order of magnitude less at 300 cm.

If one wants to calibrate a BSS, monoenergetic neutron beams shall be employed; they allow the response matrix, which is calculated by means of MC codes, to be verified. However, since well-characterized monoenergetic neutron beams are rather rare and the use of them is fairly expensive, early tests can also be carried out with radionuclide neutron sources, e.g. the Am-Be source; hence, MC information regarding the neutron spectral fluences are fundamental. In the second study the neutron spectral fluences for some positions, i.e. 40, 100, 150 cm from the Am-Be source, were convoluted with the BSS response functions [42] to obtain the total[9] counts per primary particle for each sphere. The same procedure was carried out to calculate the unscattered counts by means of the unscattered spectral fluences. This set of data will be used for real test of the BSS response

[9]scattered + unscattered

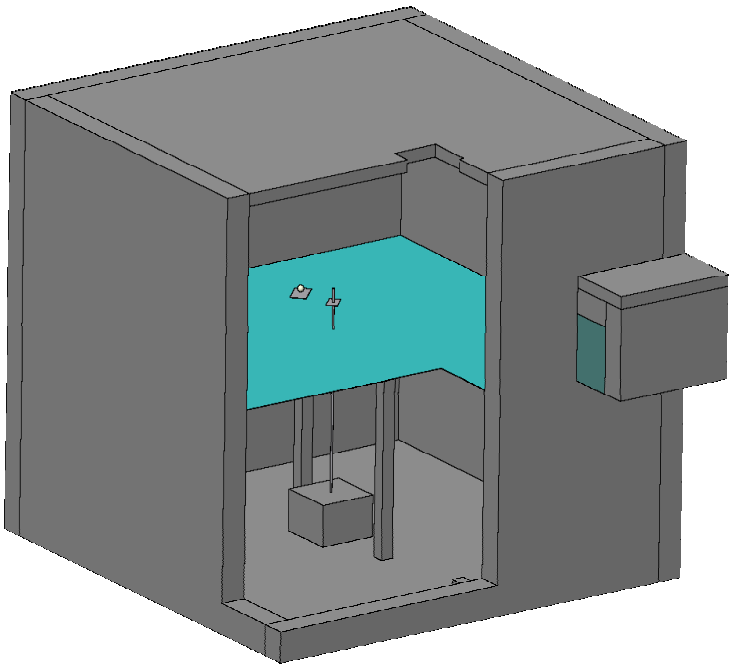

(a) *Calibration hall*

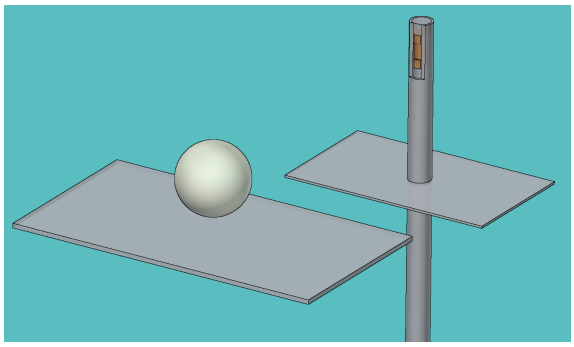

(b) *Detector and Am-Be source (in orange)*

Figure 4.43: *3D cross-sectional view of the geometry of the calibration hall used in the simulations.*

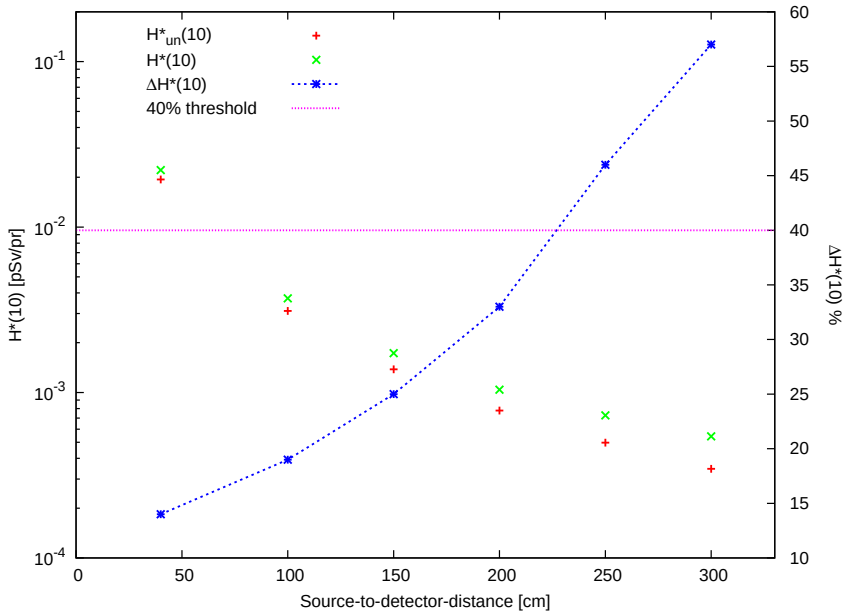

Figure 4.44: *H*(10), H*(10)$_{unscat}$ and ΔH*(10) for the Am-Be sources of the calibration hall.*

matrix. The comparison also led to the determination of the reading increase due to scattered neutron as a function of the source-to-detector distance.

Tables 4.18-4.20 and Figure 4.46 show the convolution results together with the reading increase caused by the scattered neutrons. The spheres with a response function peaking at high energies, such as Ollio, 233 mm and 178 mm, are less affected by scattered neutrons than the spheres with a response function peaking at low energies, such as 81 mm, 108 mm, 133 mm and Stanlio. This is due to the spectrum of scattered neutrons, which is peaked at thermal and epithermal energies (see Figure 4.45). For instance, Ollio shows a limited increase due to scattered neutrons, while the 81 mm sphere is very sensitive to the scattering contribution.

The third study was conducted to investigate the contribution of the following scattering objects to the overall H*(10):

i *concrete*: concrete structures, such as walls, roof, ceiling, neutron source container and pillars;

ii *support*: source support materials made of aluminum, i.e. the source holder and the N40 tube;

iii *floor*: stainless steel floor;

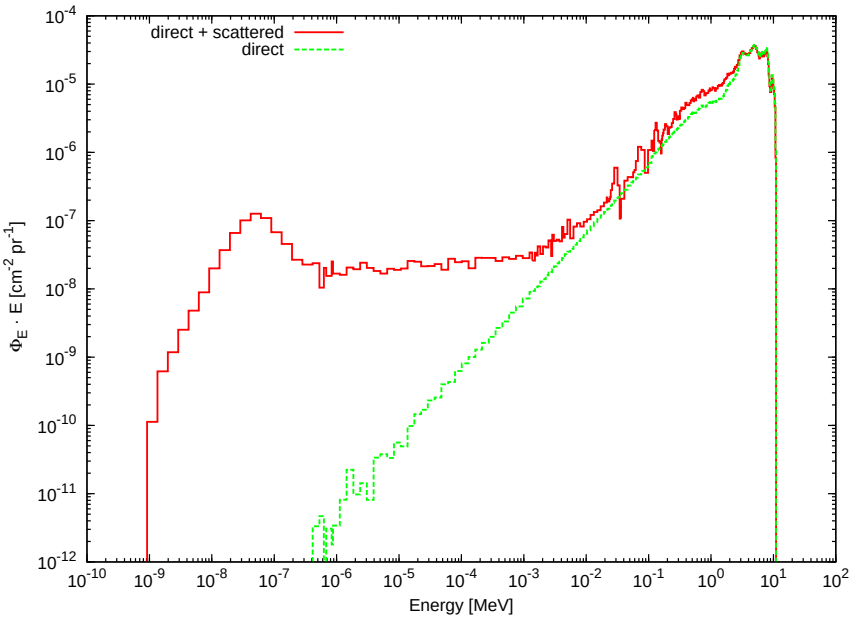

(a) *Source-to-detector distance: 40 cm*

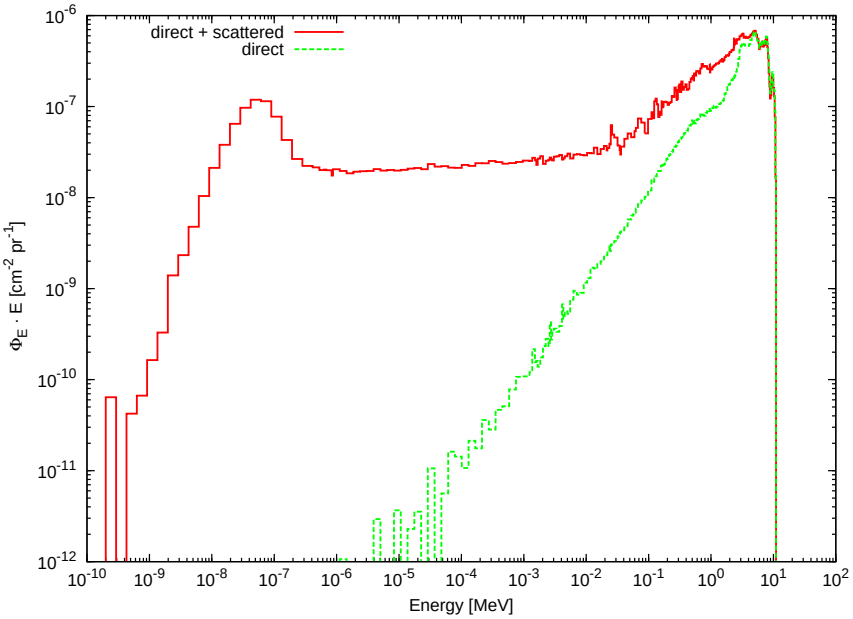

(b) *Source-to-detector distance: 300 cm*

Figure 4.45: *Total (direct+scattered) and unscattered (direct) neutron spectral fluence from the Am-Be source.*

Table 4.18: *Total and unscattered BSS counts at 40 cm from the Am-Be source. The counts are expressed in counts per primary particle.*

Sphere	**Total counts** Cts/pr	**Unscattered counts** Cts/pr	**Reading increase due to scattering**
81mm	$1.90 \cdot 10^{-5} \pm 4.37 \cdot 10^{-8}$	$1.34 \cdot 10^{-5} \pm 1.50 \cdot 10^{-8}$	42%
108mm	$5.88 \cdot 10^{-5} \pm 1.27 \cdot 10^{-7}$	$4.46 \cdot 10^{-5} \pm 6.72 \cdot 10^{-8}$	32%
133mm	$9.55 \cdot 10^{-5} \pm 1.74 \cdot 10^{-7}$	$7.55 \cdot 10^{-5} \pm 7.59 \cdot 10^{-8}$	26%
178mm	$1.34 \cdot 10^{-4} \pm 2.42 \cdot 10^{-7}$	$1.11 \cdot 10^{-4} \pm 1.25 \cdot 10^{-7}$	21%
233mm	$7.44 \cdot 10^{-4} \pm 2.46 \cdot 10^{-7}$	$1.17 \cdot 10^{-4} \pm 1.36 \cdot 10^{-7}$	15%
Ollio	$5.78 \cdot 10^{-5} \pm 1.15 \cdot 10^{-7}$	$5.21 \cdot 10^{-5} \pm 7.13 \cdot 10^{-8}$	11%
Stanlio	$2.06 \cdot 10^{-5} \pm 4.44 \cdot 10^{-8}$	$1.57 \cdot 10^{-5} \pm 2.05 \cdot 10^{-8}$	31%

Table 4.19: *Total and unscattered BSS counts at 100 cm from the Am-Be source. The counts are expressed in counts per primary particle.*

Sphere	**Total counts** Cts/pr	**Unscattered counts** Cts/pr	**Reading increase due to scattering**
81mm	$4.20 \cdot 10^{-6} \pm 1.79 \cdot 10^{-8}$	$2.12 \cdot 10^{-6} \pm 2.53 \cdot 10^{-9}$	98%
108mm	$1.11 \cdot 10^{-5} \pm 3.81 \cdot 10^{-8}$	$7.07 \cdot 10^{-6} \pm 1.09 \cdot 10^{-8}$	57%
133mm	$1.72 \cdot 10^{-5} \pm 5.28 \cdot 10^{-8}$	$1.20 \cdot 10^{-5} \pm 1.26 \cdot 10^{-8}$	43%
178mm	$2.31 \cdot 10^{-5} \pm 6.83 \cdot 10^{-8}$	$1.77 \cdot 10^{-5} \pm 2.04 \cdot 10^{-8}$	31%
233mm	$2.26 \cdot 10^{-5} \pm 6.72 \cdot 10^{-8}$	$1.86 \cdot 10^{-5} \pm 2.22 \cdot 10^{-8}$	22%
Ollio	$9.65 \cdot 10^{-6} \pm 3.01 \cdot 10^{-8}$	$8.26 \cdot 10^{-6} \pm 1.15 \cdot 10^{-8}$	17%
Stanlio	$4.08 \cdot 10^{-6} \pm 1.57 \cdot 10^{-8}$	$2.48 \cdot 10^{-6} \pm 3.36 \cdot 10^{-9}$	65%

Table 4.20: *Total and unscattered BSS counts at 150 cm from the Am-Be source. The counts are expressed in counts per primary particle.*

Sphere	**Total counts** Cts/pr	**Unscattered counts** Cts/pr	**Reading increase due to scattering**
81mm	$2.55{\cdot}10^{-6}\pm 9.70{\cdot}10^{-9}$	$9.43{\cdot}10^{-7}\pm 1.22{\cdot}10^{-9}$	170%
108mm	$5.91{\cdot}10^{-6}\pm 1.80{\cdot}10^{-8}$	$3.14{\cdot}10^{-6}\pm 5.02{\cdot}10^{-9}$	88%
133mm	$8.68{\cdot}10^{-6}\pm 2.37{\cdot}10^{-8}$	$5.31{\cdot}10^{-6}\pm 5.94{\cdot}10^{-9}$	63%
178mm	$1.12{\cdot}10^{-5}\pm 2.99{\cdot}10^{-8}$	$7.84{\cdot}10^{-6}\pm 9.46{\cdot}10^{-9}$	43%
233mm	$1.06{\cdot}10^{-5}\pm 2.90{\cdot}10^{-8}$	$8.25{\cdot}10^{-6}\pm 1.02{\cdot}10^{-8}$	28%
Ollio	$4.48{\cdot}10^{-6}\pm 1.30{\cdot}10^{-8}$	$3.67{\cdot}10^{-6}\pm 5.27{\cdot}10^{-9}$	22%
Stanlio	$2.26{\cdot}10^{-6}\pm 8.11{\cdot}10^{-9}$	$1.10{\cdot}10^{-6}\pm 1.56{\cdot}10^{-9}$	105%

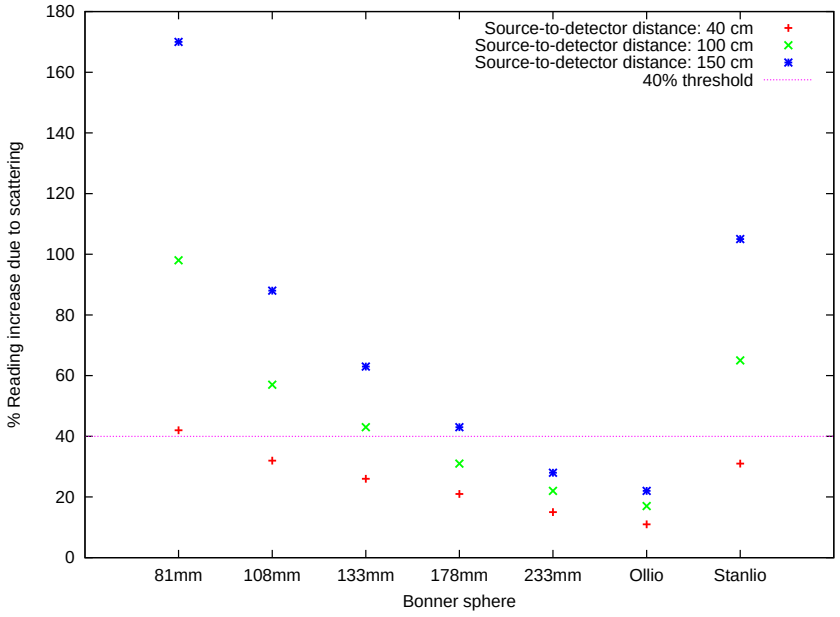

Figure 4.46: *Increase of the Bonner sphere reading due to scattered neutrons.*

Table 4.21: *Contribution of certain scattering objects to the total H*(10) for the Am-Be source.*

Std	**Concrete**		**Support**		**Floor**		**lps**	
dist. cm	$H^*(10)_{concr}$ pSv/pr	Scat.	$H^*(10)_{supp}$ pSv/pr	Scat.	$H^*(10)_{floor}$ pSv/pr	Scat.	$H^*(10)_{lps}$ pSv/pr	Scat.
40	$8.23 \cdot 10^{-5}$	3%	$1.19 \cdot 10^{-3}$	44%	$3.93 \cdot 10^{-5}$	1%	$1.17 \cdot 10^{-3}$	44%
100	$9.38 \cdot 10^{-5}$	16%	$2.17 \cdot 10^{-4}$	36%	$1.01 \cdot 10^{-4}$	17%	$2.82 \cdot 10^{-4}$	47%
150	$1.04 \cdot 10^{-4}$	30%	$9.99 \cdot 10^{-5}$	29%	$6.73 \cdot 10^{-5}$	19%	$1.48 \cdot 10^{-4}$	43%
200	$1.08 \cdot 10^{-4}$	42%	$4.90 \cdot 10^{-5}$	19%	$6.12 \cdot 10^{-5}$	24%	$9.95 \cdot 10^{-5}$	39%
250	$1.11 \cdot 10^{-4}$	48%	$3.83 \cdot 10^{-5}$	17%	$5.85 \cdot 10^{-5}$	25%	$8.75 \cdot 10^{-5}$	38%
300	$1.12 \cdot 10^{-4}$	57%	$2.75 \cdot 10^{-5}$	14%	$4.17 \cdot 10^{-5}$	24%	$7.03 \cdot 10^{-5}$	36%

iv *lps*: detector transport system, also called *l*inear *p*ositioning *s*ystem.

For each object a set of six simulations (one for each calibration point) was performed by setting the scattering object to VACUUM so that the neutrons interacting with the material were not scattered; the resulting H*(10) contribution was scored via the USTRACK card. By subtracting this H*(10) to the total H*(10), the H*(10) contribution for a single scattering object was obtained.

Table 4.21 and Figure 4.47 show the results of this study. It should be noted that it is not correct to sum over the percentage given in Table 4.21 for the same source-to-detector distance because of multiple scattering effects; for instance, a neutron that passes through a part of the bench and is subsequently scattered in the floor before arriving in the scoring volume, contributes both to the curve for the bench and for the floors. Figure 4.47 shows that the scattered neutron contribution varies with the source-to-detector distance; for calibration position close to the source (up to 100 cm) the neutron scattered by the source support structures and by the lps are dominating. From 150 cm onwards the concrete-made elements (walls, roof and ceiling), the floor and still the lps are the main sources of scattered neutrons. Hence, the scattering contribution can be described by two terms: one (related to "concrete" and "floor" scattering) is almost constant with the distance; the other (related to "support" and "lps" scattering) decreases with the distance. This trend of two terms is the basis of the fit equation (Eq. 4.8) described in Section 4.4.1.

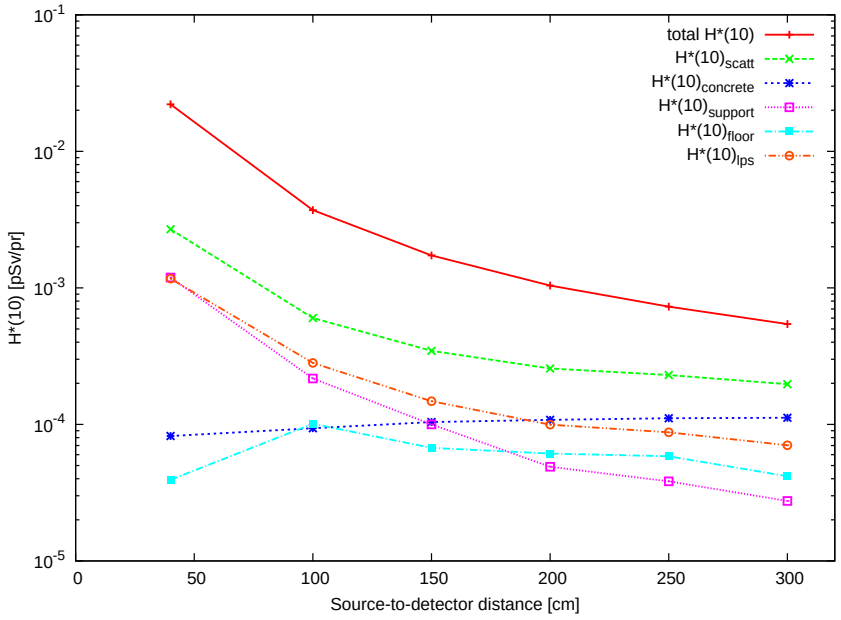

Figure 4.47: *Contribution of certain scattering objects to the total H*(10) for the Am-Be source.*

4.4 Source radiation field characterization

The radiation field characterization is a fundamental process to make the laboratory ready for operation; "characterizing" means establishing the reference value of the calibration quantity of interest, e.g. the H*(10), as a function of the source-to-calibration distance together with its uncertainty. This section illustrates the measurements performed to characterize the radiation fields of the sources with the highest activities: the 888 GBq Am-Be source (Section 4.4.1), the 3 TBq Cs-137 source (Section 4.4.2) and the 11.8 TBq Co-60 source (Section 4.4.3). Even if it is not described here, the characterization was also performed for the other neutron and gamma sources of the calibration hall [43].

4.4.1 Am-Be 888 GBq: measurements and simulations

The radiation field of the 888 GBq Am-Be source was characterized by means of measurements and FLUKA simulations. As already mentioned the contribution of the scattered neutrons must be subtracted from the measurements. The shadow-cone method is often the most employed one and, if properly used, is the very reliable; however, it was not used since the laboratory is not equipped with a set of shadow-cones. The generalized-fit method is well suited and the main

disadvantage, as stated in ref. [30], is that can only be used for spherical moderating detectors with spherical central detectors. The semi-empirical method can only be employed if the main sources of neutron scatter are the room walls, floor and ceiling, which is not always the case since at very small calibration distances the scattering from the source support structures is dominant. There is an important difference in the philosophy of use between the first three methods and the reduced-fitting method. For the first three method one makes an initial careful set of measurements to determine the values of the parameters required to correct for scattering and "geometry" effects; for subsequent calibration of similar instruments, one may then calibrate at just one, or a few points and make the corrections using these parameters. On the other hand, the reduced-fitting method essentially treats each calibration independently and determines the parameters for each individual instrument separately.

For the radiation field characterization of the neutron sources, the SmartREM rem-counter was employed. The detector was calibrated at Physikalisch-Technische Bundesanstalt (PTB) primary standard laboratory. The ambient dose equivalent rate, H*(10), of the SmartREM is calculated from Eq. 4.6:

$$H^*(10) = M \cdot N \cdot c_F \cdot c_L \tag{4.6}$$

where M is the reading of the device, i.e. the uncorrected H*(10) in μSv/h, N is the calibration factor (PTB certificate), c_L is the correction for linearity (PTB certificate) and c_F is the field specific correction that takes into account that the detector is used in a radiation field different from the one used for the calibration (Cf-252, PTB certificate). The numerical values of these coefficients are listed in Table 4.22. The measurements were carried out on both Track1 and Track2, and about 30 points were taken starting at the closest source-to-detector distance available for calibrations (68 cm on Track1 and 65 cm on Track2). The SMARTREM readings were recorded for each position every five seconds for about 20 minutes. The mean value M was calculated as well as its standard deviation (type A). Afterwards, the H*(10) was obtained from Eq. 4.6 by applying the correction factors and the final standard deviation was obtained as the square root of the quadratic sum of the relative uncertainties (type A + type B).

The data were fitted using Eq. 4.7 (generalized-fit method [30]). The fit was performed using PYTHON and the Orthogonal Distance Regression (ODR) that allows the uncertainty on the calibration distance (1 mm, type B) to be taken into account.

$$M_T(l) = \frac{k}{l^2} \cdot F_3(l) \tag{4.7}$$

where $M_T(l)$ is the total count-rate (direct neutrons + scattered neutrons) at a source-to-detector distance l; k is the characteristic constant specific to each

Table 4.22: *SmartREM correction coefficients as listed in the PTB calibration certificate. The uncertainties are quoted at 1σ and are of type B. The relative uncertainties are also listed. The calibration factor,* N*, is given for the Cf-252 and the field specific correction factor,* c_F*, is provided for the Am-Be source.*

	Value	$\mathbf{u}_{rel}$
N (Cf-252)	0.922±0.013	1.4%
$\mathbf{c}_F$ **(Am-Be)**	1.09±0.04	3.7%
$\mathbf{c}_L$	1.00±0.01	1.0%

source-detector combination, which is a free parameter in the fit; $F_3(l)$ corrects for the deviation of the count-rate from the simple-inverse square law and is given by Eq. 4.8:

$$F_3(l) = \frac{F_1(l)}{F_A(l)} + A' \cdot l + s \cdot l^2 \tag{4.8}$$

where $F_1(l)$ is the geometry factor that takes into account the finite size of source or detector (at distances larger than twice the diameter of the device is close to 1, see Eq. 4.9, where r_S and r_D are the radius of the source (1.27 cm) and the detector (10.4 cm), respectively); $F_A(l)$ is the air attenuation (air out-scatter) correction, which is given by ref. [30] for ambient conditions (T = 21^{o}C, pressure 100,4 kPa and humidity 50%) for an Am-Be source (see Eq. 4.10); A' and s are free parameters whose magnitudes and uncertainties are calculated using the least-squares techniques.

$$F_1(l) = 1 + \frac{0.29}{(1 + 1.79 \cdot \frac{l - r_S - r_d}{r_D})^2} \tag{4.9}$$

$$F_A(l) = exp[l \cdot 890 \cdot 10^{-7}] \tag{4.10}$$

The generalized-fit method lies on the assumption that the scattered neutron contribution is described by a constant term, i.e. s, and a term decreasing with distance, i.e. A/l. This hypothesis was verified by the neutron scattering study illustrated at the end of Section 4.3.4; Figure 4.47 confirmed the presence of the two scattering contributions. Eventually, in order to evaluate the fit, the residuals were analysed by fitting their distribution with a Normal function (Eq. 4.11), since the deviation between the measured value and the one calculated from the fit must be a random variable.

Table 4.23: *Fit parameters of Eq. 4.11 together with their standard deviation for both Track1 and Track2.*

	Track1	**Track2**
G	0.06±0.02	0.14±0.02
μ	-3.17·10^{-4}±1.23·10^{-3}	-1.16·10^{-4}±4.95·10^{-4}
σ	6.03·10^{-3}±2.28·10^{-3}	5.47·10^{-3}±7.00·10^{-4}

$$F(x) = \frac{G}{\sigma\sqrt{2\pi}} e^{-\frac{(x-\mu)^2}{2\sigma^2}} \tag{4.11}$$

Some *a priori* considerations can be drawn concerning the measurements performed on Track1 and Track2. The k parameters obtained on Track1 and Track2 should be equal (within the uncertainty) for the same detector since this coefficient does not depend on the calibration bench and method but only on the type of detector. The s parameters, which mainly describe the scattering contribution by the walls, ceiling, roof and floor, are supposed to be equal within the uncertainty. The same behaviour should be theoretically shown by the *A'* parameters that represent the scattered neutron contribution of the source support material; however, the presence of the gamma source irradiator at the end of Track1 could have some influence.

Figure 4.48 shows the H*(10) measured by the SmartREM together with the fit. Eq. 4.7 fits very well the experimental data; the last is also confirmed by the residual analysis shown in Figure 4.49 (for Track1) and in Figure 4.50 (for Track2). The residuals in both cases are normally distributed around zero (the Normal fit parameters are listed in Table 4.23). Table 4.24 lists the fit parameters for Eq. 4.7 and their standard deviation obtained with the ODR for both Track1 and Track2. The ratio between the parameters for Track1 and Track2 is also given. As expected the ratio for the s and k parameters is close to 1; instead the ratio between the *A'* parameters is slightly different from 1 and is the result of the fact that the scattered neutron contribution proportional to *1/l* is not equal on Track1 and Track2.

The experimental measurements on Track2 were compared with FLUKA simulations. As in the first FLUKA study of Section 4.3.4 the H*(10) (direct+scattered) was scored on Track2 from a source-to-detector distance of 30 cm up to 300 cm in steps of 10 cm (for the simulated geometry refer to Figure 4.43). The simulations results showed a relative statistical uncertainty (type A) of about 1%. The data were normalized to the neutron source strength of the 888 GBq Am-Be source,

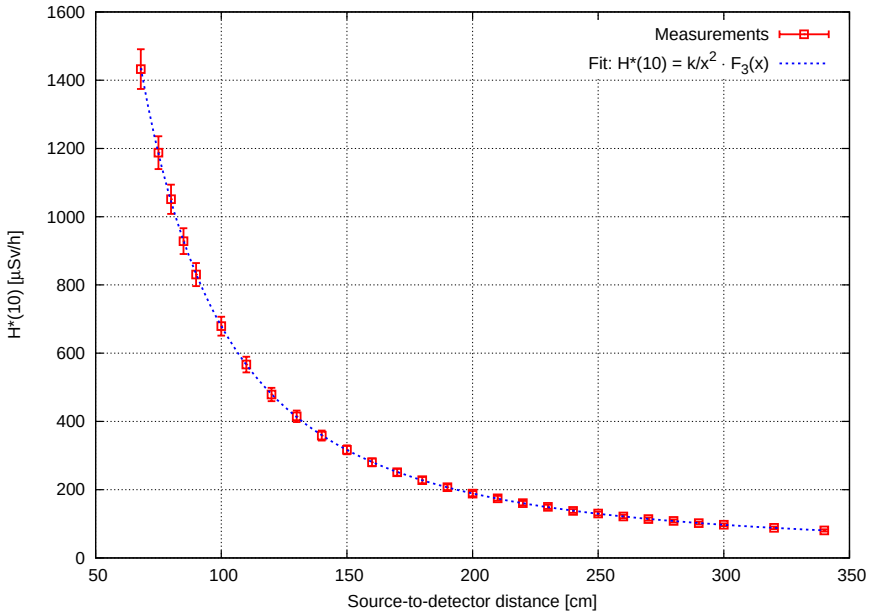

(a) *Track1*

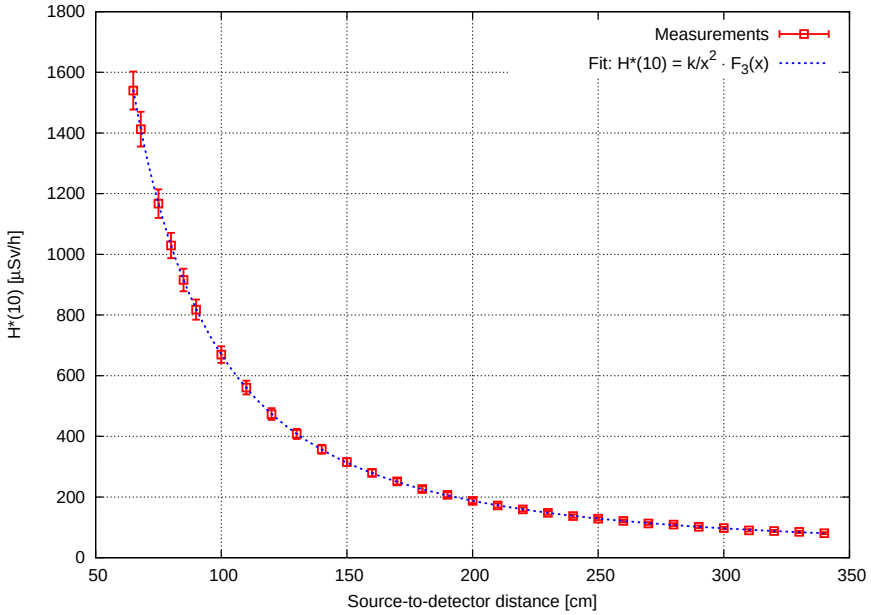

(b) *Track2*

Figure 4.48: *Graph of the measurements performed for the 888 GBq Am-Be source and their standard deviation together with the fit.*

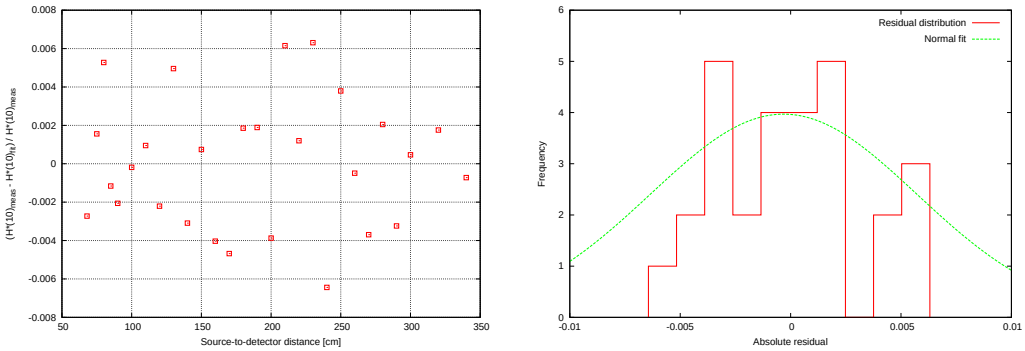

Figure 4.49: *On the left side the absolute residuals of the fit by means of Eq. 4.7 and on the right the absolute residual distribution together with the Normal fit for Track1.*

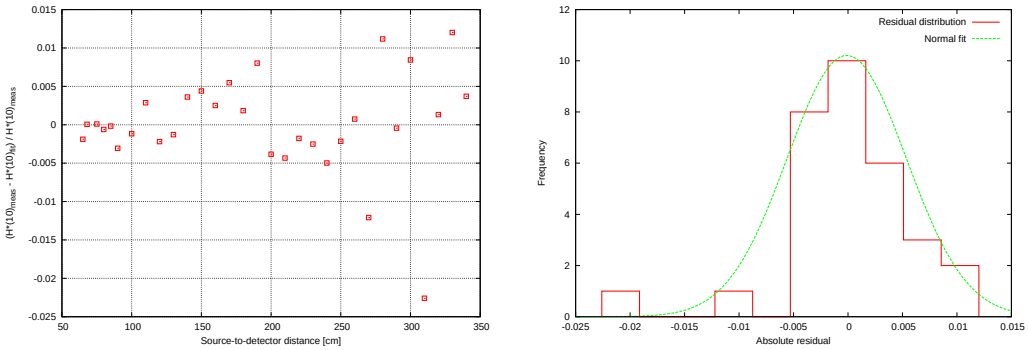

Figure 4.50: *On the left side the absolute residuals of the fit by means of Eq. 4.7 and on the right the absolute residual distribution together with the Normal fit for Track2.*

Table 4.24: *Fit parameters of Eq. 4.7 obtained from the ODR fit together with their standard deviation for both Track1 and Track2.*

	Track1	**Track2**	**Track1/Track2**
A'	$3.37{\cdot}10^{-4}{\pm}5.45{\cdot}10^{-5}$	$4.74{\cdot}10^{-4}{\pm}9.34{\cdot}10^{-5}$	0.71
s	$3.19{\cdot}10^{-6}{\pm}1.28{\cdot}10^{-7}$	$3.06{\cdot}10^{-6}{\pm}2.15{\cdot}10^{-7}$	1.04
k	$6.42{\cdot}10^{6}{\pm}2.87{\cdot}10^{4}$	$6.26{\cdot}10^{6}{\pm}4.70{\cdot}10^{4}$	1.03

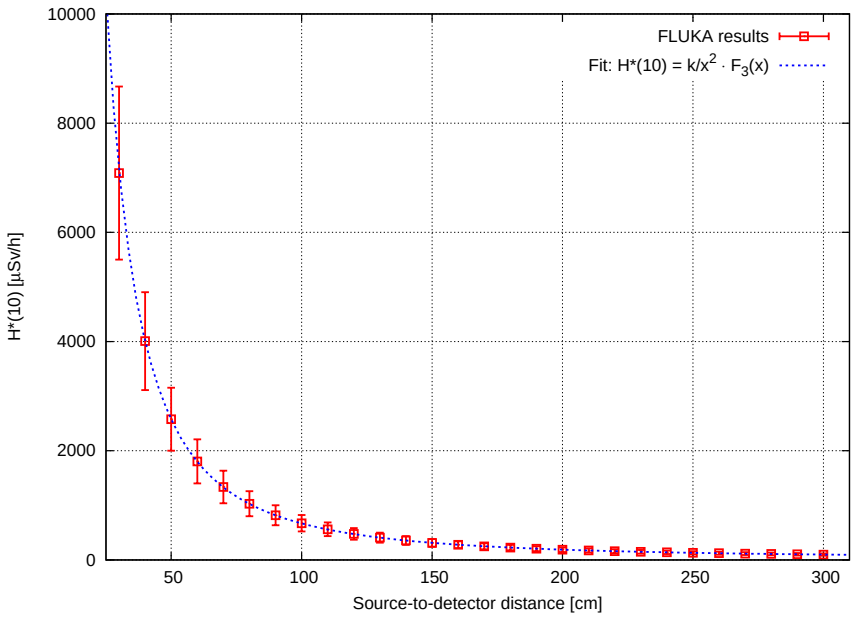

Figure 4.51: *Graph of the simulated H*(10) on Track2 with their standard deviation (1% type A + 5% type B) together with the fit from Eq. 4.7.*

i.e. $5.03{\cdot}10^7$ s^{-1}; the source manufacturer provides a relative uncertainty of 5% (type B) that was taken into account to calculate the final standard deviation of the simulation results.

Figure 4.51 shows the simulated H*(10) together with the fit (Eq. 4.7). The curve fits very well the data and this is confirmed by the residual analysis shown in Figure 4.52 and Table 4.26. The parameters of Eq. 4.7 were obtained from the fit and are listed in Table 4.25; they are in good agreement with the experimental ones calculated for Track2. By plotting on the same graph (Figure 4.53) the experimental and the simulation data one can see the very good agreement between the two. The maximum deviation is about 3% at the source-to-detector distance of 270 cm.

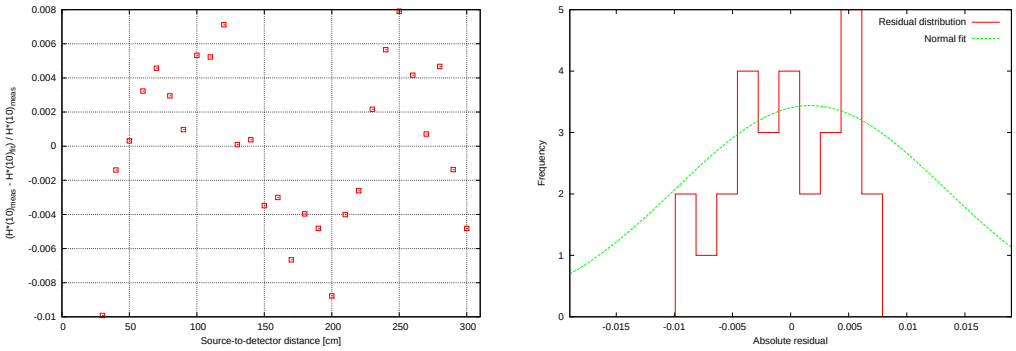

Figure 4.52: *On the left side the aboslute residuals of the fit from Eq. 4.7 and on the right the absolute residual distribution together wit the Normal fit for the simulations on Track2.*

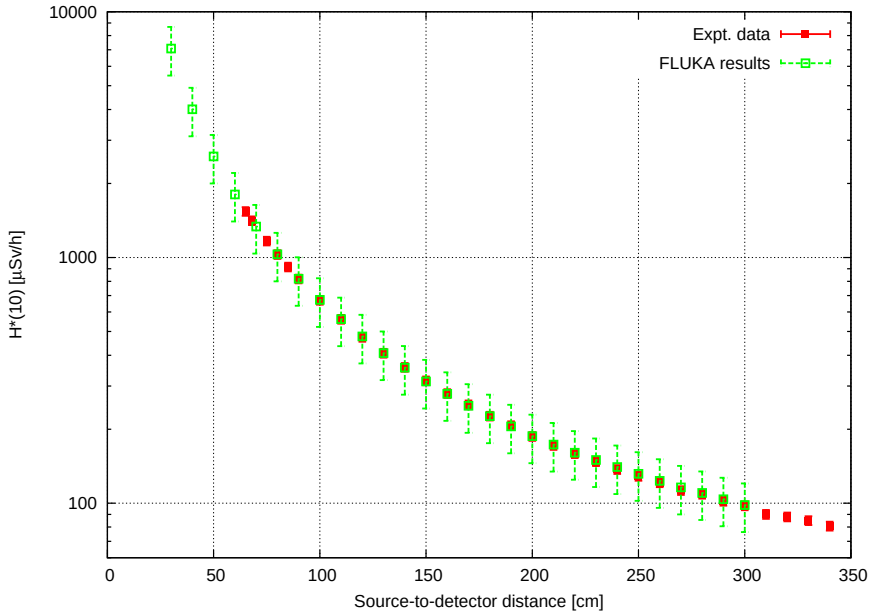

Figure 4.53: *Comparison of the simulated H*(10) and the experimental one on Track2 for the 888 GBq Am-Be source.*

Table 4.25: *Fit parameters of Eq. 4.7 obtained from the ODR fit together with their standard deviation for the simulations on Track2 and comparison with the parameters obtained experimentally.*

	$\mathbf{Track2}_{FLUKA}$	$\mathbf{Track2}_{Expt}$	$\mathbf{Track2}_{FLUKA}/\mathbf{Track2}_{Expt}$
A'	$4.18{\cdot}10^{-4}{\pm}6.26{\cdot}10^{-5}$	$4.74{\cdot}10^{-4}{\pm}9.34{\cdot}10^{-5}$	0.88
s	$3.59{\cdot}10^{-6}{\pm}1.76{\cdot}10^{-7}$	$3.06{\cdot}10^{-6}{\pm}2.15{\cdot}10^{-7}$	1.17
k	$6.25{\cdot}10^{6}{\pm}2.64{\cdot}10^{4}$	$6.26{\cdot}10^{6}{\pm}4.70{\cdot}10^{4}$	1.00

Table 4.26: *Fit parameters of Eq. 4.11 obtained from the Normal fit together with their standard deviation for the simulations on Track2.*

	$\mathbf{Track2}_{FLUKA}$
G	$0.10{\pm}0.04$
μ	$1.71{\cdot}10^{-3}{\pm}2.61{\cdot}10^{-3}$
σ	$1.16{\cdot}10^{-2}{\pm}5.14{\cdot}10^{-3}$

4.4.2 Cs-137 3 TBq: measurements and characterization

The radiation field generated by the Cs-137 sources was characterized in terms of air-kerma rate according to ref. [5] and [44] by means of several ionization chambers. The characterization process consists in measuring with a secondary standard device, i.e. an ionization chamber calibrated in a primary standard laboratory, the air-kerma rate along the calibration track (Track1). Nevertheless care has to be taken in calculating the uncertainty budget. The following ISO recommendations were also taken into account:

- the air-kerma rate shall be measured on the axis of the beam at the various points of test;
- after correcting for air attenuation, the air-kerma rates shall be proportional within 5 % to the inverse square of the distance from the source centre to the detector centre;
- the standard test conditions: ambient temperature between 291.15 K and 295.15 K, ambient pressure between 86 kPa and 106 kPa and, relative humidity between 30% and 75%;

- the instrument to be used for the measurements of the reference radiation shall be a secondary standard or other appropriate instrument;
- sufficient time shall be allowed for the instrument to stabilize;
- sufficient time shall be allowed between measurements so that the measurements are independent of the response time of the instrument;

The air-kerma rate at a specific source-to-detector distance can be expressed by the following model (Eq. 4.12):

$$K_{air} = k_P \cdot k_T \cdot N_k \cdot M \cdot k_R \cdot k_H \tag{4.12}$$

where:

- k_P is the correction factor that takes into account the difference between the reference air pressure, P_0 (1013.2 hPa), and the pressure during the measurements, P; it is given by Eq. 4.13 and its uncertainty is given by Eq. 4.14.

$$k_P = \frac{P_0}{P} \tag{4.13}$$

$$u(k_P) = \frac{u(P)}{P^2} \cdot P_0 \tag{4.14}$$

- k_T is the correction factor that takes into account the difference between the reference air temperature, T_0 (293.2 K), and the temperature during the measurements, T; it is given by Eq. 4.15 and its uncertainty is given by Eq. 4.16.

$$k_T = \frac{T}{T_0} \tag{4.15}$$

$$u(k_T) = \frac{u(T)}{T_0} \tag{4.16}$$

- N_k is the calibration factor in Gy/C given in the ionization chamber calibration certificate.
- k_R is the correction factor that accounts for the uncertainty in the placement of the ion chamber. It is assumed to be equal to 1 and can be modelled by Eq. 4.17:

$$k_R = \frac{R^2}{R_0^2} \tag{4.17}$$

and its associated uncertainty is given by Eq. 4.18:

$$u(k_R) = \frac{2 \cdot R \cdot u(R)}{R_0^2} \tag{4.18}$$

where R_0 is the nominal source-to-detector distance and R is the corresponding stochastic variable, the distribution of which is rectangular, centred in R_0. The width of the distribution is estimated on the precision of determining the reference position and the laboratory experience. The uncertainty, *u(R)*, is therefore given by Eq. 4.19:

$$u(R) = \frac{\Delta R}{2 \cdot \sqrt{3}} \tag{4.19}$$

where ΔR is the distribution width equal to 0.1 cm.

- M is the electrometer reading corrected for polarity effect, ion collection efficiency and leakage. The uncertainty *u(M)* is obtained from the resolution of the instrument (4 digits), i.e. 0.001 pA. *u(M)* is calculated via a rectangular distribution centred in M and with half-width of 0.0005 pA. Therefore *u(M)* = 0.000289 pA.

- k_H is the correction factor that takes into account the dependence of the instrument on the relative humidity. It is assumed to be equal to one and its relative uncertainty, $u_{rel}(k_H)$, is 0.02% if the relative humidity is between 20% and 70%.

Table 4.27 lists the coefficients of Eq. 4.12 together with their relative uncertainty. The relative uncertainty of type B associated to the single measure of the air-kerma rate is given by Eq. 4.20:

$$u_{rel}(K_{air})_B = \sqrt{u^2_{rel}(k_P) + u^2_{rel}(k_T) + u^2_{rel}(N_k) + u^2_{rel}(k_R) + u^2_{rel}(M) + u^2_{rel}(k_H)} \tag{4.20}$$

The final relative uncertainty (type A + type B) over the air-kerma rate is given by Eq. 4.22 and is the quadratic sum of the relative uncertainty of type A coming from the standard deviation of the n number of measurements, H_i (Eq. 4.21), and the maximum of the relative uncertainty of type B.

$$u(K_{air})_A = \sqrt{\frac{\sum_{i=1}^{n}(\bar{H} - H_i)^2}{n(n-1)}} \tag{4.21}$$

$$u_{rel}(K_{air}) = \sqrt{u^2_{rel}(K_{air})_{BMAX} + u^2_{rel}(K_{air})_A} \tag{4.22}$$

The experimental measurements were fitted with the inverse-square law (Eq. 4.23, Figure 4.54) as ISO recommended [44]:

$$K_{air} = \frac{A}{x^2} \tag{4.23}$$

Table 4.27: *Coefficients of Eq. 4.12 for the measurements performed to characterize the 3 TBq Cs-137 source.*

	Value	$\mathbf{u}_{rel}$
k_P	1.052	0.5%
k_T	1.008	0.3%
N_k[Gy/C]	$3.306 \cdot 10^5$	1.0%
k_R	1.000	Max. 0.07%
k_H	1.000	0.02%

Table 4.28: *Fit parameters of Eq. 4.11 obtained from the Normal fit together with their standard deviation for the absolute residuals of Eq. 4.24.*

G	0.020 ± 0.001
μ	$1.59 \cdot 10^{-4} \pm 1.41 \cdot 10^{-4}$
σ	$1.27 \cdot 10^{-3} \pm 1.99 \cdot 10^{-4}$

where A ($1.66 \cdot 10^9 \pm 3.83 \cdot 10^6$) is a free parameter whose magnitude is obtained from the ODR. The fit was judged acceptable (Figure 4.54) since the air-kerma rates are proportional within 5% to the inverse square of the source-to-detector distance; however, the residuals of the fit (Figure 4.55a) are not normally distributed; this may be due to the scattering of photons within the hall, which is not taken into account in Eq. 4.23. Therefore, another fit equation (Eq. 4.24) was used:

$$K_{air} = a + \frac{b}{x} + \frac{c}{x^2} + d \cdot \frac{log(x)}{x^2} + \frac{e}{x^3} \tag{4.24}$$

where a ($3.59 \cdot 10^2 \pm 2.52 \cdot 10^2$), b ($-8.89 \cdot 10^5 \pm 4.16 \cdot 10^5$), c ($5.56 \cdot 10^8 \pm 5.01 \cdot 10^8$), d ($2.25 \cdot 10^8 \pm 1.02 \cdot 10^8$), and e ($1.68 \cdot 10^{10} \pm 7.21 \cdot 10^9$) are free parameters whose magnitude is obtained from the ODR. Eq. 4.24 is an empirical formula provided by the irradiator manufacturer. The fit is very good (Figure 4.54); unlikely the fit with Eq. 4.23, the residuals are normally distributed (Figure 4.55a and b, Table 4.30). Even though this formula is not the one ISO recommended, it was decided to employ it for the determination of the air-kerma rate as a function of the source-to-detector distance.

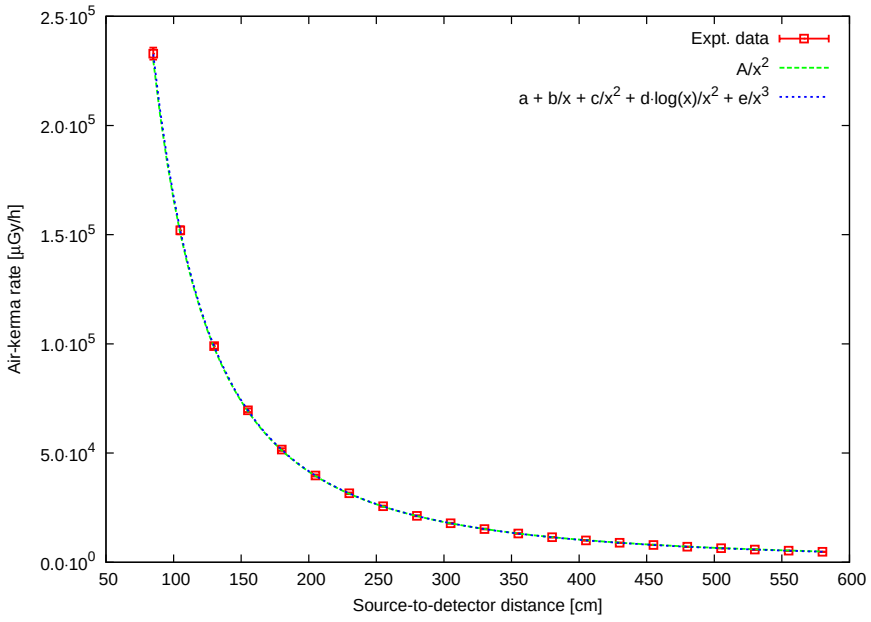

Figure 4.54: *Cs-137 3 TBq air kerma rate from measurements and the two fits.*

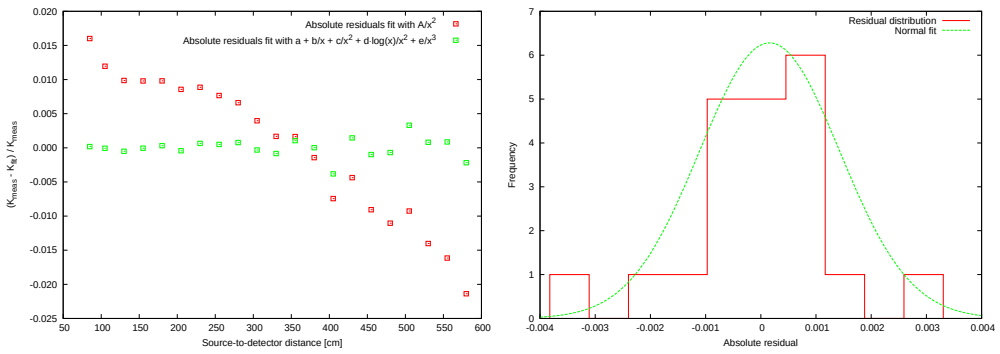

(a) (b)

Figure 4.55: *(a) The absolute residuals of the two fits. (b) The absolute residual distribution of Eq. 4.24 together with the Normal fit.*

Table 4.29: *Coefficients of Eq. 4.12 for the measurements performed to characterize the 11.8 TBq Co-60 source.*

	Value	$\mathbf{u}_{rel}$
k_P	1.026	0.5%
k_T	1.005	0.3%
N_k[Gy/C]	$9.123 \cdot 10^5$	1.0%
k_R	1.000	Max. 0.08%
k_H	1.000	0.02%

Table 4.30: *Fit parameters of Eq. 4.11 obtained from the Normal fit together with their standard deviation for the absolute residuals of Eq. 4.23 and Eq. 4.24.*

	Eq. 4.23	**Eq. 4.24**
G	0.06±0.02	0.06±0.01
μ	$-1.75 \cdot 10^{-3} \pm 2.24 \cdot 10^{-3}$	$4.80 \cdot 10^{-4} \pm 5.29 \cdot 10^{-4}$
σ	$7.57 \cdot 10^{-3} \pm 3.25 \cdot 10^{-3}$	$5.12 \cdot 10^{-3} \pm 7.48 \cdot 10^{-4}$

4.4.3 Co-60 11.8 TBq: measurements and characterization

The same considerations drawn for the characterization of the 3 TBq Cs-137 (Section 4.4.2) were taken into account in order to characterize the radiation field of the 11.8 TBq Co-60 of the irradiation room 1. Table 4.29 lists the coefficients of Eq. 4.12,

Figure 4.56 shows the experimental measurements together with the fits performed using Eq. 4.23 (the inverse-square law) and Eq. 4.24. The inverse-square law ($A = 3.41 \cdot 10^7 \pm 5.94 \cdot 10^4$) fits fairly well the measurements as well as Eq. 4.24 ($a = 2.19 \cdot 10^2 \pm 1.50 \cdot 10^2$, $b = -2.11 \cdot 10^5 \pm 1.57 \cdot 10^5$, $c = -1.08 \cdot 10^8 \pm 1.16 \cdot 10^8$, $d = 3.17 \cdot 10^7 \pm 2.55 \cdot 10^7$, and $e = 1.52 \cdot 10^9 \pm 1.27 \cdot 10^9$). The residual analysis reveals that, even if the residuals of both fits look like randomly distributed around zero (Figure 4.57a), Eq. 4.24 fits much properly the data since its absolute residual distribution is well fit by a Normal function. As done for the Cs-137 sources, Eq. 4.24 was also employed for the determination of the air-kerma rate as a function of the source-to-detector distance.

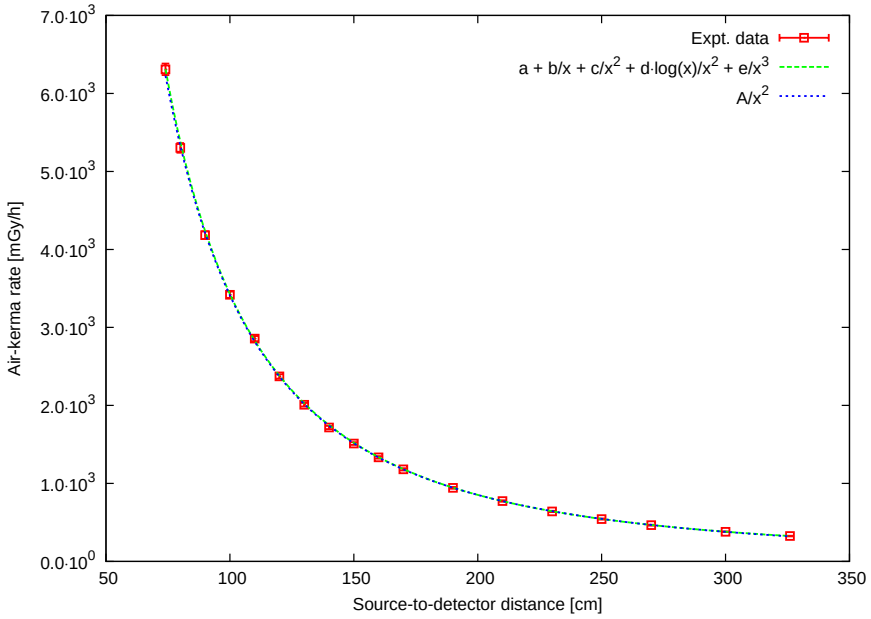

Figure 4.56: *Co-60 11.8 TBq air kerma rate from measurements and the two fits.*

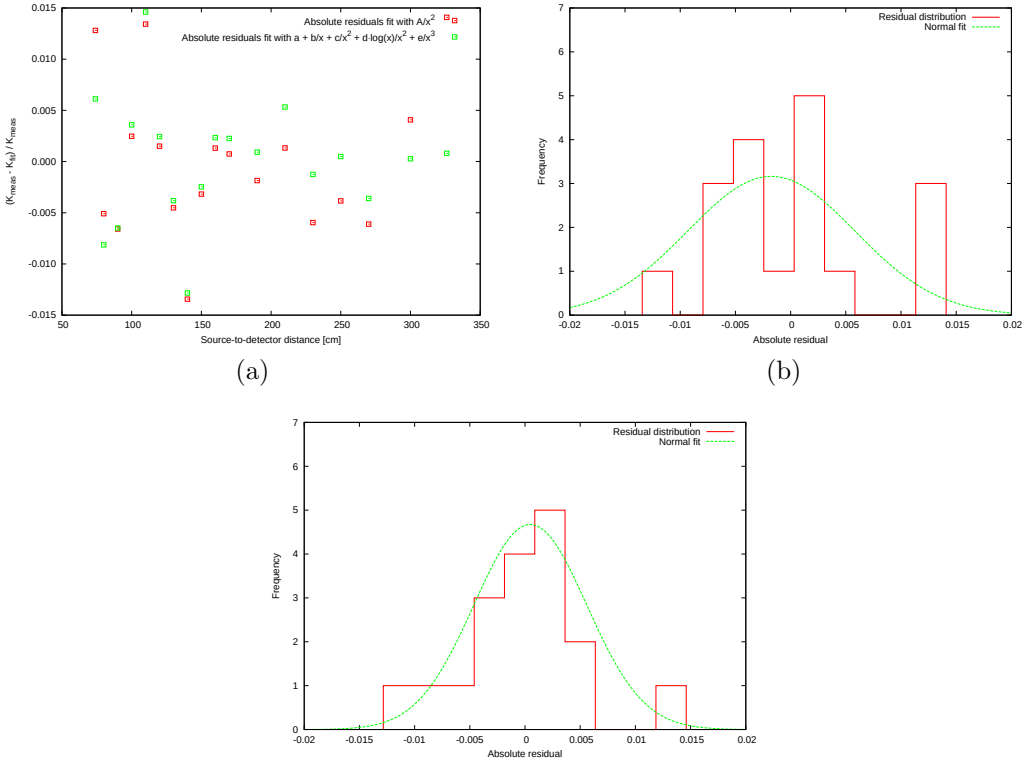

Figure 4.57: *(a) Absolute residuals of the two fits. (b) Absolute residual distribution for the inverse square law (Eq. 4.23). (c) Absolute residual distribution for Eq.4.24.*

Chapter 5

CERN-EU high-energy Reference Field (CERF) facility

CERF is a facility complementary to the RP calibration laboratory (Chapter 4) since it provides a simulated workplace neutron field with a broad spectrum with energies extending up to hundreds of MeV. CERF has been available at CERN since 1992 (Section 5.1) and the reference spectra and dose values were calculated using the 1997 version of the FLUKA code, from now-on FLUKA-1997 [45–48]. The code has undergone many developments, especially concerning the neutron physical models. Hence, new simulations were performed with the current FLUKA development version (from now-on FLUKA-2015) and a few geometrical changes were implemented (Section 5.3). The results were benchmarked with measurements performed in the December 2014 CERF run. This work, even though it is not still ongoing, aimed at properly characterizing the neutron radiation field in order to start the facility accreditation process as reference workplace field. Together with the calibration laboratory, CERF provides CERN with a wide range of calibration fields for radiation protection, tests and research. Section 5.2 describes the ionization chamber (IC) that is used to monitor the CERF beam and the activation experiments carried out to verify its calibration factor. The verification of the calibration factor is fundamental to provide a reliable reference for data normalization. Finally, Section 5.4 shows how CERF can be employed not only for radiation protection calibrations but also for the measurements of cross-sections for proton- and pion-induced reactions at high-energies. The outcomes of these experiments demonstrate the wide capabilities of CERF.

5.1 H6 area and CERF facility

CERF is installed in one of the secondary beam lines (H6) from the Super Proton Synchrotron (SPS), in the North Experimental Area on the Prévessin (France) site of CERN. This section provides a general description of the H6 experimental area and of the CERF facility.

5.1.1 H6 area

The H6 beam is derived from the T4 target station served by the SPS proton beam with a momentum of 450 GeV/c and since July 2000 by protons of 400 GeV/c, with typical intensities of several 10^{12} protons per burst; the SPS supercycle has usually two extractions to the North Experimental Area per minute, with a duration of about 5 s. The beam line can be operated to transport secondary particles in the momentum range 5 GeV/c $\leq$p$\leq$ 205 GeV/c and to create tertiary beams. Those are available in sufficient intensities if the secondary H6 beam has at least an energy of 100 GeV; a further target can be introduced into the beam to produce tertiary beams of lower energy. The CERF facility is situated about 410 m downstream of the T4 target [49]. The layout of the target station T4 is shown schematically in Figure 5.1. The direction of incidence of the primary proton beam on the target is governed by the two magnets B1T and B2T. Magnets B3T and BEND1(H6) serve to direct the secondary particles of the chosen polarity, momentum and production angle into the H6 line and deviate the remaining beam onto the dump [50].

Several scintillators and Multiwire Proportional Chambers (MWPCs) located in the beam line are used to monitor the steering of the beam and to record the spot size and the position of the beam. Figure 5.2 shows the beam optics layout of the H6 beam line indicating the position of magnets, collimators, beam scintillators, MWPCs and the CERF facility.

5.1.2 CERF facility

The CERF facility is a development of an idea conceived by Stevenson in 1987, when an experimental area was set-up to study the spatial distribution of hadron and low-energy neutron fluence and of absorbed dose in the cascades induced in iron and lead calorimeter structures irradiated by high-energy hadron beams. The experiments were intended to provide benchmarks for Monte Carlo codes simulating the development of hadron-induced cascades. At that time the experimental area simply consisted of a thick iron or lead block surrounded by a concrete shield. The CERN reference radiation facility is a development of these experiments; it was set-up in 1992 and subsequently upgraded to its present

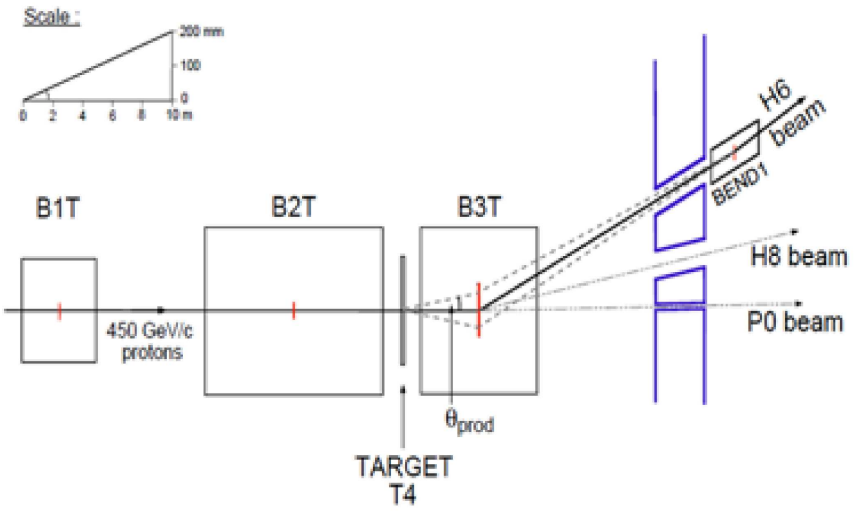

Figure 5.1: *Schematic plan of the target station T4 [50].*

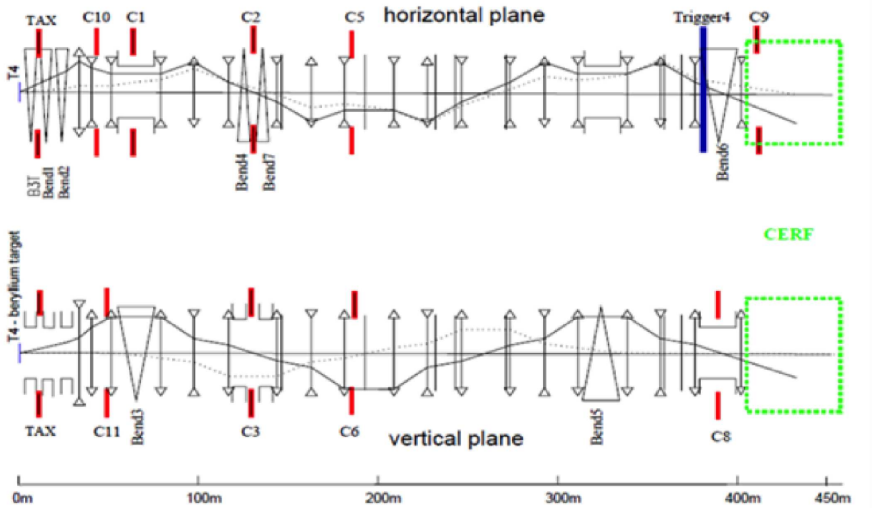

Figure 5.2: *Elements of the H6 beam optics in the horizontal and vertical planes. Not to scale. The solid line indicates the excursion of a particle with an angular offset at T4 (1 mrad) and the dotted line shows the trajectories of on-axis particles with a momentum different from the nominal one ($\Delta p/p \sim 1\%$) [50].*

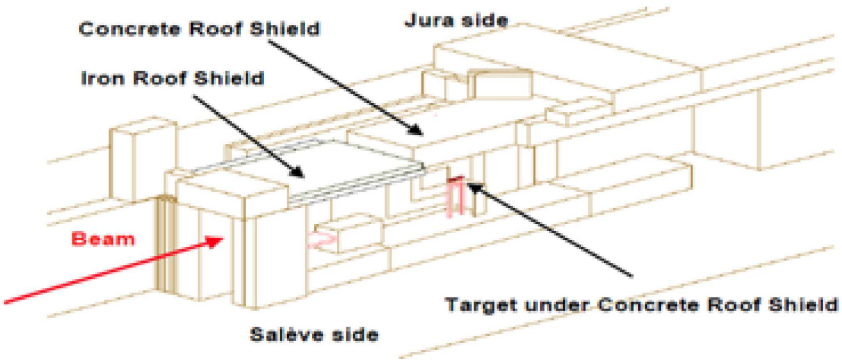

Figure 5.3: *Axonometric view of the CERF facility in the North Experimental Hall on the Prèvessin site of CERN as modeled in FLUKA. The side shielding on the Saléve side is removed to show the inside of the irradiation cave with the copper target set-up [51].*

form in 1993. In addition to the interest for testing active instrumentation and passive detectors used around high-energy particle accelerators, this reference field is sufficiently similar to the cosmic ray field encountered at 10-20 km altitude such that instrumentation is tested, inter-compared and calibrated at CERN and subsequently used for in-flight measurements on board commercial aircraft [51]. An axonometric view of the CERF facility is shown in Figure 5.3. A positive hadron beam (a mixture of 61% pions, 35% protons and 4% kaons, as determined experimentally) with a momentum of usually 120 GeV/c is stopped in a copper target, 7 cm in diameter and 50 cm in length, which can be installed in two different positions inside the irradiation cave. The interaction of the beam with the target produces secondary particles (mainly neutrons, but also photons, electrons, muons, pions and protons, see also Section 5.3) which traverse a shielding, on top of these two positions and at 90° with respect to the incoming beam direction, made up of either 80 cm concrete or 40 cm iron. These roof-shields produce almost uniform radiation fields over two areas of 2x2 m^2, each of them divided into 16 squares of 50x50 cm^2, as shown in Figure 5.4. Each element of these grids represents a reference exposure location.

The spectrum outside the iron shield is dominated by neutrons in the 0.1-1 MeV energy range. The energy distribution outside the concrete shield shows an additional large relative contribution of 10-100 MeV neutrons. The latter reproduces fairly closely, although not exactly, the neutron field produced by cosmic rays at commercial flight altitudes. The photon fluence is almost one order of magnitude lower than the neutron fluence on the concrete roof-shield. The electron fluence is about one order of magnitude less than that of neutrons and the muon fluence

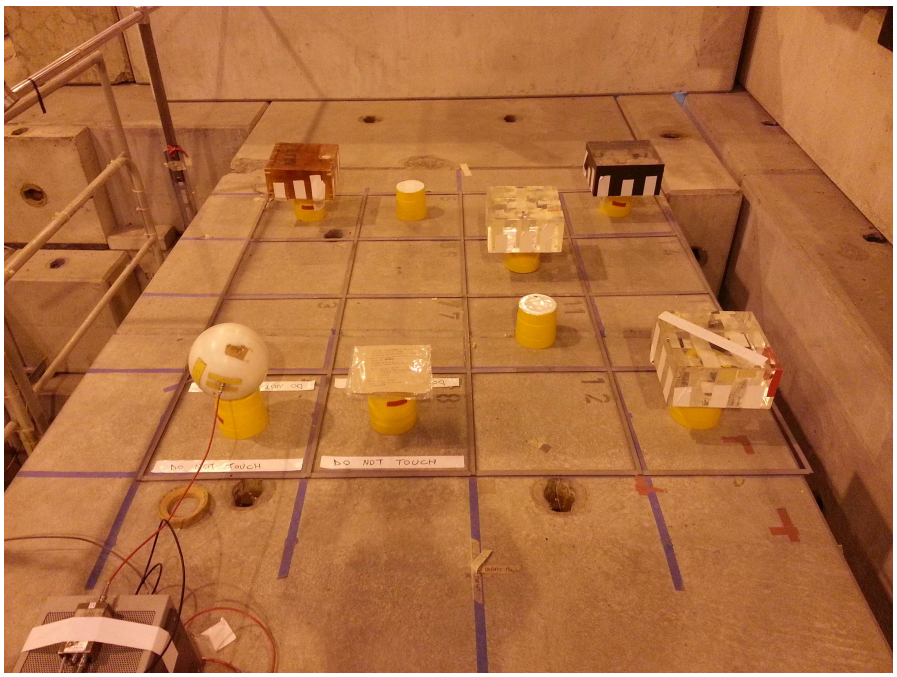

Figure 5.4: *The reference grid with the 16 exposure locations used on the concrete roof shield.*

almost three orders of magnitude less. However, an additional muon component is also present which directly comes from the upstream H6 beam line and adjacent lines, as well from pion decay in the beam line. Their intensity depends on various factors which are not under direct control, such as the intensity of secondary beams in neighboring beam lines. The accuracy of the calculated neutron spectral fluences was verified in the past by extensive measurements performed by several collaborating institutions and different instrumentation. The intensity of the primary beam is monitored by an air-filled Ionization Chamber (IC) at atmospheric pressure, placed in the beam just upstream of the copper target, connected to a current digitizing circuit. One IC-count corresponds (within $\pm 10\%$) to $2.2 \text{x} 10^4$ particles impinging on the target (see Section 5.2 for the IC calibration). Both the calculated spectral fluences and the data of the experiments performed at CERF are usually normalized to the intensity of the beam impinging on the target [51].

5.2 Beam monitoring at CERF

The calibration factor of the IC used to monitor the 120 GeV/c hadron beam at CERF was verified via different techniques. Firstly, it was calculated by assessing the energy deposited by the CERF hadron beam in the active volume of the chamber via FLUKA simulations. Secondly, it was derived from activation experiments performed with hyperpure aluminum and copper foils. The calibration via copper activation was never used before and showed to be a promising technique. In this section the theoretical bases of the monitor reactions are explained and the various factors to be taken into account for the calibration with the activation foil technique are thoroughly discussed.

5.2.1 Ionization Chamber description

The IC is a simple parallel-plate, transmission-type ionization chamber with a diameter of 185 mm. The chamber has five parallel electrode plates made of Mylar, of 2.5 mg/cm^2 thickness and 17 mm inter-plate spacing. The central plate is the collector and the ones on either side are the polarity electrodes. A schematic view of the monitor is shown in Figure 5.5. The inter-plate spacing has been derived from an industrial computer tomography scan performed at CERN (Figure 5.6). It has been found to be 17 mm, a value slightly larger than the one used in the past (16 mm) for the estimate of the calibration factor. The voltage on the plates is supplied through a BNC cable by an external battery placed on the floor just below the chamber. The polarization voltage provided by this battery is about -270 V. The beam traverses 34 mm of air (rather than 32 mm as thought in the past) at atmospheric pressure in the sensitive part of the chamber. The IC is mounted on a standard pedestal normally used to support beam line components such as vacuum chambers. The output signal of the chamber is fed into a charge digitizer, which is mounted on the lower side of a base plate; this plate is mounted together with the IC, sandwiched between the chamber and the pedestal. The digitizer requires a 24 V voltage provided through a Burndy connector by a power supply placed on the floor next to the pedestal (Figure 5.6). The output TTL pulses (5 V amplitude and 5 μs length) are fed to a National Instrument USB 6341 DAQ which is connected to a desktop computer (PC) in the CERF cage. The data acquisition is controlled via a recently written LabVIEW program running on a PC.

The IC and related electronics were checked with a Cs-137 source in the former calibration laboratory. The IC was exposed to dose rates ranging from 10 μSv/h to 50 mSv/h. Table 5.1 shows the results of the measurements and the related efficiency of the chamber, expressed in fA per μSv/h. Apart from the two sensitivity values affected by a non-homogenous field since the chamber was too close to the source, the sensitivity is quite constant and its mean value is 9.9 fA/μSv/h.

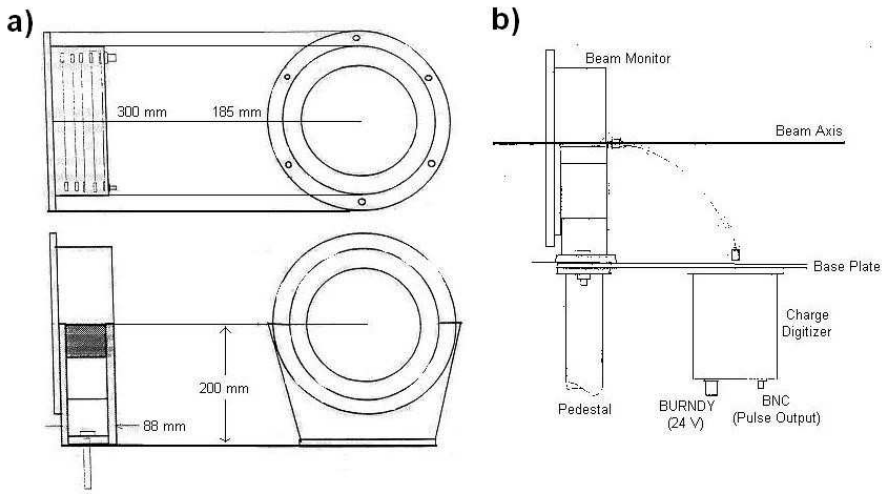

Figure 5.5: *a) Schematic view of the IC and its support; b) sketch of the installation of the IC and charge digitizer [52].*

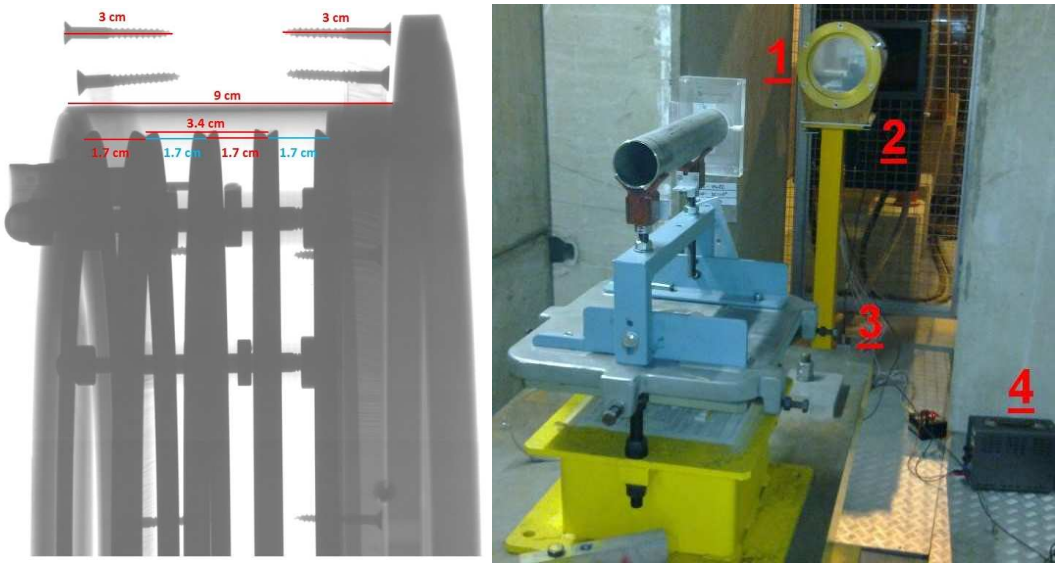

(a) *X-ray scan* (b) *IC set-up*

Figure 5.6: *a) Image of the industrial computed tomography of the IC performed at CERN. The wooden support of the chamber is not visible in the X-ray image. b) Beam monitoring set-up: IC (1), charge digitizer (2), battery (3) and power supply (4).*

Table 5.1: *Results of measurements performed in the former calibration laboratory with a Cs-137 source.*

Dose rate μSv/h	**Output frequency** Hz	**Corresponding current** pA	**Sensitivity** fA/μSv/h
10	0.12	0.10	10.0
100	1.18	0.98	9.8
500	5.88	4.90	9.8
1000	12.1	10.1	10.1
5000*	55.8	46.5	9.3
10000	118	98.9	9.9
50000*	532	443	8.9

* Measurements affected by non-homogeneous field

The value derived in the past was 10.6 fA/μSv/h [53], but the acquisition system of the output signal was quite different.

5.2.2 Estimation of the calibration factor

Before performing the activation experiments, the IC calibration factor was estimated via the FLUKA code [54]. The expected charge q collected on the plates of the IC per primary particle must be calculated to estimate the calibration factor (see Eq. 5.1).

$$q = E_{dep} \cdot \frac{e}{W_{air}} \tag{5.1}$$

E_{dep} is the energy deposited by a primary particle in the sensitive volume of the IC, e is the electron charge ($1.609{\cdot}10^{-19}$ C) and W_{air} (34.23±0.14 eV [55]) is the average energy released by the primary particles to produce an ion pair in air. FLUKA simulations were run to assess the energy deposited by 120 GeV/c protons, positive pions and positive kaons in the air volume of the IC (p = 0.963 atm, $\rho = 1.12{\cdot}10^{-3}$ g/cm^3). The geometry employed in the simulation is shown in Figure 5.7. In the past [56, 57] the collected charge was estimated via a formula that took into account the air density, the atmospheric pressure and the stopping power (taken from the literature) of the primary particles. However, this method lies on the stringent assumption that the stopping power value is equal to the energy deposited by a primary particle in the active volume. This is not exactly true. In fact, in the case of a particle traversing the active volume of the IC, the

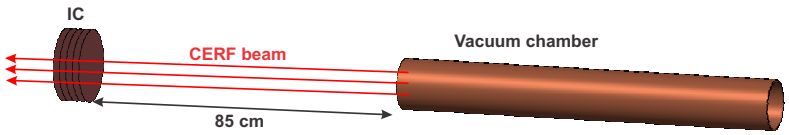

Figure 5.7: *Scheme of the geometry employed in the FLUKA simulations for the calculation of the deposited energy.*

stopping power defines the loss of kinetic energy of the particle in the volume, which is not equal to the deposited energy. The deposited energy does not include the energy transported by the delta rays that escape from the volume, while it takes into account the energy lost by the particle through nuclear reactions. This problem can be overcome by employing FLUKA to obtain the energy deposited. The values of the air density and the active length of the IC are implicitly included in the results, since they are given as input parameters of the simulations.

In the FLUKA input file the DELTARAY card was activated to consider the delta rays production by muons and charged hadrons in the sensitive volume with an energy threshold of 50 keV. Electromagnetic transport cards (EMF and EMF-CUT) were activated setting the transport threshold energy for electrons and positrons to 50 keV and for photons to 10 keV. The energy deposition within the IC sensitive volume was scored by the USRBIN card. The results of the simulations give an energy deposition value of 7.92 keV for protons, 8.15 keV for positive pions and 7.94 keV for positive kaons. The results are affected by 1% statistical uncertainty. Taking the beam composition corrected for the pion decay into account (see Section 5.2.3 for the detailed explanation), i.e. 60.0% pions, 35.9% protons, 4.1% kaons, the weighted energy deposition is 8.06 keV per primary particle. The expected charge generated in the IC by a primary particle is given by Eq. 5.2.

$$q = 8.06 \cdot 10^3 \; eV \cdot \frac{1.609 \cdot 10^{-19} \; C}{34.23 \; eV} = 3.79 \cdot 10^{-17} \; C \tag{5.2}$$

By using the sensitivity factor of the charge digitizer (k = 1.19 counts/pC, as given in the previous Section) the expected calibration factor, i.e. the number of primary particles needed to obtain one TTL pulse from the charge digitizer, is:

$$CF = (q{\cdot}k)^{-1} = (3.79{\cdot}10^{-5}\, pC{\cdot}1.19\, counts/pC)^{-1} = 22172\, particles/count \tag{5.3}$$

This result is affected by the uncertainty on W_{air} (0.4%, systematic) and E_{dep}, whose uncertainty is the sum of two components, the one derived from the FLUKA

simulations (1%, statistical) and the uncertainty on the knowledge of the active length of the PIC (3%, i.e. 1 mm over 34 mm, statistical, which derives from the spatial resolution of the program employed to analyze the tomographic image). The total uncertainty is then obtained by quadratically adding the two statistical uncertainties and by linearly adding the systematic uncertainty, which gives a calibration factor of 22172±789 particles per IC-count.

5.2.3 Foil activation technique: Al and Cu activation

Foil activation is a well-established technique [58] for measuring the intensity of high energy proton beams. It is particularly convenient for the calibration of ICs used for on-line beam monitoring. One of its advantages is the accuracy that can be achieved if the cross section of the reaction of interest is known with a small uncertainty. When the protons traverse the foil they generate spallation reactions *A(p,x)B*, where *A* is the stable isotope of which the foil is constituted, *B* is the radioisotope produced in the foil by the spallation reaction, whose activity is determined via γ-spectrometry, x represents the reaction products (one or more particles, depending on the reaction) escaping the foil. If *A(t) [Bq]* is the activity induced in the foil, t_{IRR} *[s]* and t_{WAIT} *[s]* are the irradiation time and waiting time, i.e. the time elapsed from the end of the irradiation until the foil is counted, N_x *[cm^{-2}]* is the foil surface atomic density, σ *[cm^2]* is the production cross section of the selected radioisotope, the particle flux Φ' (number of particles per second traversing the foil) can be obtained as:

$$\Phi' = \frac{A(t)}{N_x \cdot \sigma \cdot (1 - e^{-\lambda t_{IRR}}) \cdot e^{-\lambda t_{WAIT}}} \tag{5.4}$$

A(t) is measured by γ-spectrometry, while t_{IRR} and t_{WAIT} must be recorded. In the present experiment t_{WAIT} was recorded manually while t_{IRR} was obtained from the log-file of the acquisition system.

An ideal monitor reaction should show the following properties [59]:

- cross section known with good accuracy;
- half-life of the radioisotope produced in the foil longer than the irradiation time, but not too long in order to obtain a detectable activity;
- γ-line(s) of the radioisotope produced in the foil easily detectable and distinguishable by γ-spectrometry;
- negligible contribution to the production of the radionuclide of interest by secondary particles, such as neutrons and energetic secondary hadrons, generated by interaction of the positive hadron beam in the target.

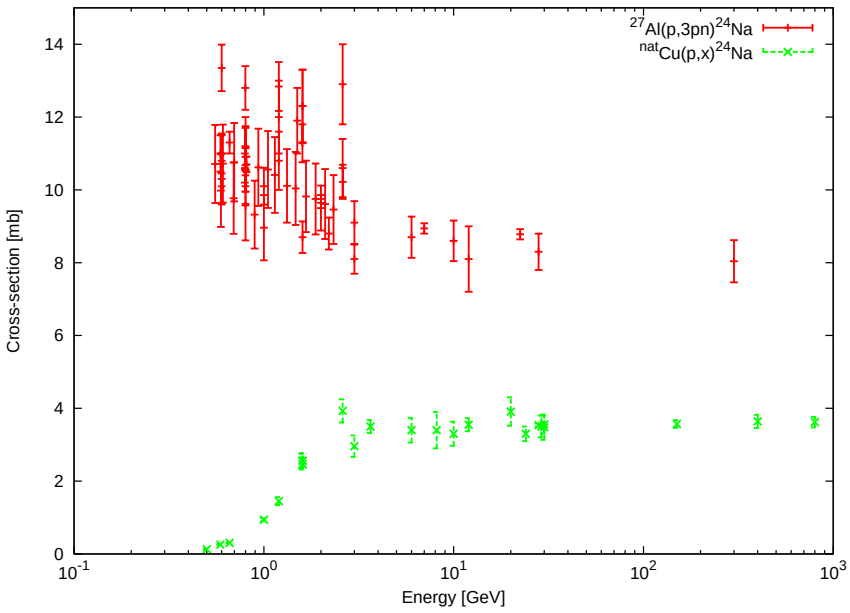

Figure 5.8: *Cross-section data available in the literature for the ^{27}Al(p,3pn)^{24}Na and the ^{nat}Cu(p,x)^{24}Na reactions for energies higher than 0.5 GeV [61].*

Unfortunately none of the commonly used reactions satisfy all of these requirements and one has to find a compromise. The first chosen reaction is the ^{27}Al(p,3pn)^{24}Na reaction, which is one of the most extensively used beam monitor reactions [58]. Its main advantages are the following [59].

- The short half-life of ^{24}Na (∼15 h) results in a high specific activity so a relatively short irradiation time is adequate to obtain a reasonable activity to be determined by γ-spectrometry.
- ^{24}Na decays by β^- emission producing two γ-rays of energies 2.754 MeV and 1.369 MeV (branching ratios: 99.94% and 100%, respectively), whose peaks can be easily identified by γ-spectrometry.
- The ^{27}Al(p,3pn)^{24}Na cross section is known with good accuracy in a wide energy range. Figure 5.8 plots the available cross-section data for energies higher than 0.5 GeV. The 300 GeV value comes from indirect measurements [60].
- Hyperpure ^{27}Al foils are readily available.

To obtain an accurate determination of the particle flux, as derived from Eq. 5.4, one must take into account several parameters on which the reaction critically depends:

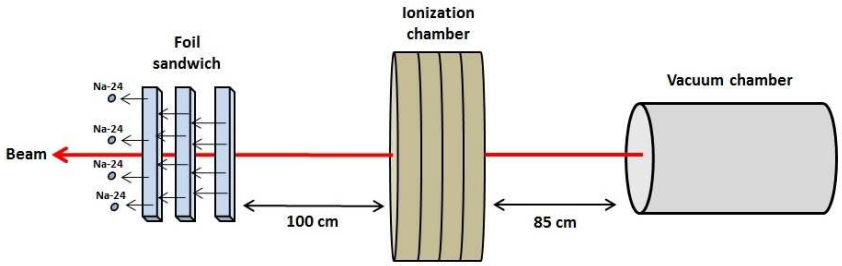

Figure 5.9: *Foil activation experimental set-up (not to scale) [59].*

- the cross section value at the energy of interest;
- the importance of the competing ^{27}Al(n,α)^{24}Na reaction, as well as of the reactions induced by energetic secondary hadrons produced in the foils, in the determination of the total induced activity;
- the recoil of some of the nuclei produced in the spallation process that can leave the foil in the same direction of the primary beam (see Figure 5.9).

A first problem arises in the determination of the cross-section to be employed in case of a mixed hadron beam, which is the case of CERF. Whilst for the proton-induced spallation reaction the cross-section data are available, for pion-induced reactions there are no published data. The value of the pion-induced cross-section can be indirectly determined using the FLUKA code. Even if FLUKA cannot be used to derive the absolute value of the cross-sections at very high energies with the required accuracy, it is much more reliable in the determination of the ratio of the cross-sections of reactions induced by different particles at the same energy on the same target. One can therefore calculate the ratio between the cross section of pion- and proton-induced reactions and then derive the absolute value of the pion-induced one. The cross-section ratio can be obtained by running the nuclear interaction models of FLUKA in interaction only mode, accounting for both absorption and quasi-elastic reactions. The output file provides the cross-section for each isotope produced in the interaction between the primaries and the target. By running two simulations, for protons and for pions, one obtains the ratio between the pion- and the proton-induced cross-sections for the reaction of interest. Since the value of the proton-induced spallation cross-section of interest is known from the literature, one can derive the pion-induced cross-section and thus obtain the effective cross-section for the mixed beam. The importance of the reactions induced by neutrons and energetic secondary hadrons in the production

of ^{24}Na is discussed in Section 5.2.5. This effect has been evaluated *a posteriori* by analysing the induced activities of all the exposed foils. The foils were irradiated in sandwiches of three to take into account the recoil of some of the nuclei produced in the spallation process that can leave the foil in the same direction of the primary beam due to the so-called Lorentz boost [62]. In order to maintain the equilibrium between the loss of recoil nuclei knocked out of the foil and the gain of nuclei knocked into the foil from upstream material, only the central one must be considered for data analysis, whereas the upstream and the downstream ones act as catchers. These catchers, having the same thickness of the central foil, are thick enough to capture all the knocked on or knocked back products; this is because the foil is thicker than the projected range of the recoil nuclei in aluminium and copper.

The ^{nat}Cu(p,x)^{24}Na reaction is a promising alternative reaction for beam monitoring, as it shows two advantages when compared to ^{27}Al(p,3pn)^{24}Na.

- The cross-section, even if it is lower than that of ^{27}Al(p,3pn)^{24}Na, is known with better accuracy at high energies. Figure 5.8 plots the available cross-section data for energies higher than 0.5 GeV. At very high energies (30, 150, 400 and 800 GeV) Baker et al. [63] found an energy-independent cross-section value of 3.59±0.14 mb.
- ^{24}Na is produced only in deep spallation reactions induced by high energy hadrons, while the secondary neutrons produce mostly isotopes close to the original target mass.

As for the ^{27}Al(p,3pn)^{24}Na reaction, the following two parameters play an important role in the determination of the particle flux:

- the value of the reaction cross-section at the energy of interest;
- the recoiling nuclei as discussed above.

In case of mixed proton/pion beams the same procedure described above can be followed to obtain the effective beam cross-section. As for the ^{27}Al foils, the ^{nat}Cu foils were exposed in sandwiches to compensate for the recoil effect.

5.2.4 Experimental set-up and results

Table 5.2 lists the specifications of the hyper-pure ^{27}Al and ^{nat}Cu foils used in the IC calibration experiment. The foils were fixed on a Plexiglas frame mounted on both ends of a hollow aluminium tube of the same dimensions of the target normally employed at CERF placed downstream of the IC. The beam size was

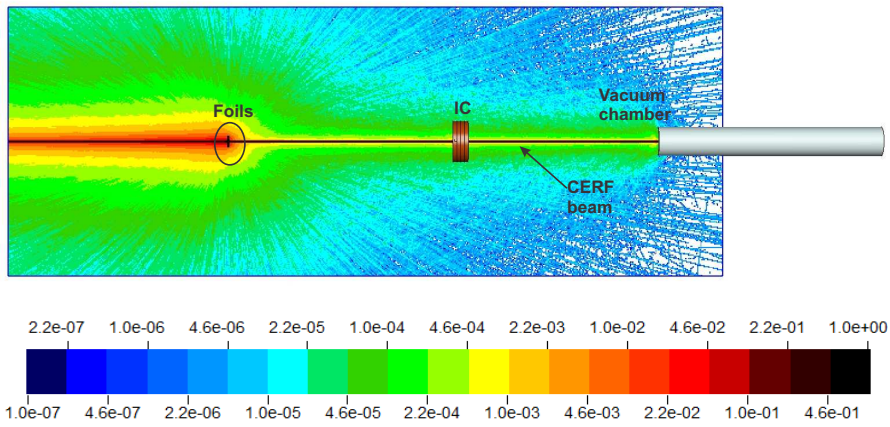

Figure 5.10: *Fluence of all particles [59](electrons, kaons, neutrons, photons, protons and pions) produced by the beam in the experimental set-up (the legend is given in cm^{-2}), plotted with SimpleGeo [64].*

smaller than the foil dimensions so that all particles traversing the IC hit the foils (Figure 5.10). To evaluate the contribution of scattered radiation to the foil activation, in one of the experiments an additional foil was exposed out of beam.

The spectrometry measurements were performed with a very low background XtRa (Extended Range) coaxial germanium detector by Canberra (GX4020 model) with a resolution of 2.0 keV (FWHM) at 1.33 MeV and relative efficiency $\geq 40\%$. The data acquisition and analysis was carried out with the Genie-2000 and the PROcount-2000 software, which include a set of spectrum analysis algorithms and provide nuclide identification, interference correction, weighted mean activity, background subtraction and efficiency correction. The software takes into account geometrical effects, self-absorption in the sample and decay of the isotope during the spectrometry measurement. The results are given in Table 5.3. Where available, the activity of the upstream and downstream foils is given. The value used in Eq. 5.4 was the one of the central foil, except for measurement 1 where, due to the high uncertainties, an average of the central and downstream foil was employed. The foil exposed out of beam did not show any significant induced activity for both materials, confirming that the contribution of the scattered radiation is negligible.

To obtain the IC calibration factor one needs to know the parameters in Eq. 5.4. To improve the accuracy of the calculation, the irradiation time was subdivided in one-second irradiation periods, thanks to the fact that the beam intensity was recorded every second in the acquisition log-files. The total activity was obtained as the sum of the partial activities induced by each one-second irradiation, by

Table 5.2: *Specifications of the foils used in the activation experiments [59]. The atomic density is the surface atomic density in cm^2.*

99.999% Al foils (ρ_{Al} = 2.71 g/cm^3, M$_{Al}$ = 27 g/mol)				
Foil dimensions [mm^2]	50 x 50	50 x 50	50 x 50	
Foil thickness X$_{Al}$ [mm]	0.50±0.05	1.0±0.1	2.0*±0.2	
Mass thickness [mg/cm^2]	135	270	540	
Atomic density N$_x$ [cm^2]	$3.0222{\cdot}10^{21}$	$6.0445{\cdot}10^{21}$	$1.2089{\cdot}10^{22}$	
Impurities [ppm]	Mg 1.2, Si 0.8, Cu 0.3, Fe 0.3			
99.99% Cu foils (ρ_{Cu} = 8.92 g/cm^3, M$_{Cu}$ = 63.546 g/mol)				
Foil dimensions [mm^2]	50 x 50	50 x 50	50 x 50	50 x 50
Foil thickness X$_{Cu}$ [mm]	0.125*±0.001	0.250±0.003	0.500*±0.005	1.000±0.010
Mass thickness [mg/cm^2]	111.5	223	446	892
Atomic density N$_x$ [cm^2]	$1.0567{\cdot}10^{21}$	$2.1133{\cdot}10^{21}$	$4.2266{\cdot}10^{22}$	$8.4531{\cdot}10^{21}$
Impurities [ppm]	Ag 70, Fe 2, Ni 2, Pb 2, Si 2, Al 1, Bi 1, Ca 1, Mg 1, Sn 1			

* Two separate experiments were performed for this thickness

Table 5.3: *Results of the foil activation experiments (uncertainties quoted at 1σ) [52, 59]. Thick. = thickness, Flu. = integrated fluence, Act. = activity, n.a. = not available.*

Al foils						
Measurement	1	2	3	4		
Thick. [mm]	2.0	2.0	1.0	0.50		
T$_{IRR}$ [s]	31139	31371	58223	31371		
Flu. [IC-cts]	$2{\cdot}10^6$	$2.3{\cdot}10^6$	$3.8{\cdot}10^6$	$2.3{\cdot}10^6$		
Act.$_{up}$ [Bq]	45.8±2.2	n.a.	34.5±1.9	n.a.		
Act.$_{cen}$ [Bq]	52.7±5.4	56.8±2.3	37.1±1.9	12.3±0.6		
Act.$_{down}$ [Bq]	47.1±1.6	n.a.	n.a.	n.a.		
Cu foils						
Measurement	5	6	7	8	9	10
Thick. [mm]	1.000	0.500	0.500	0.250	0.125	0.125
T$_{IRR}$ [s]	55459	54831	55459	55459	54831	55459
Flu. [IC-cts]	$9.09{\cdot}10^6$	$3.30{\cdot}10^6$	$9.09{\cdot}10^6$	$9.09{\cdot}10^6$	$3.03{\cdot}10^6$	$9.09{\cdot}10^6$
Act.$_{cen}$ [Bq]	48.7±2.2	8.4±0.6	22.1±1.1	13.0±0.9	2.3±0.2	5.2±0.6

taking into account the decay of ^{24}Na occurring from the end of each one-second irradiation until the arrival in the spectrometry laboratory, about 30 minutes after the end of the irradiation. Therefore, the beam-on/beam-off periods, i.e. spill time over the total SPS cycle (10 s and 45 s, respectively), were exactly taken into account and fluctuations in the beam intensity during the spill were also properly considered. The values of t_{IRR}, t_{WAIT} and Φ' were then derived from the IC acquisition log-files, where all the quantities are registered every second. The surface atomic densities, N_x, are given in Table 5.2 for each foil. The beam effective cross-section was calculated as follows. For the ^{27}Al(p,3pn)^{24}Na reaction the proton-induced cross-section at 120 GeV/c was assumed equal to the one calculated by Cumming [58] at 28 GeV/c, i.e. 8.3±0.5 mb. The pion/proton cross-section ratio was obtained by the FLUKA interaction models as described in Section 5.2.3, giving a value of 0.764±0.011 (the uncertainty is the statistical uncertainty of the Monte Carlo simulations). The pion-induced cross-section is then 6.3±0.4 mb. To obtain the beam effective cross-section one also has to take into account the pion decay and calculate the surviving pion fraction since the CERF area is located at 410 m from the T4 target, where pions are produced. Pions have a mass of 0.14 GeV/c^2 and half-life of $2.6 \cdot 10^{-8}$ s; the latter has to be corrected for relativistic effects via the Lorentz factor, which is 857.1 at 120 GeV/c, obtaining a value of $2.23 \cdot 10^{-5}$ s. The travel time from the T4 target and CERF for a pion travelling approximately at the speed of light is $1.37 \cdot 10^{-6}$s; therefore, one can calculate the surviving fraction, P_{sur}, via Eq. 5.5:

$$P_{sur} = e^{-ln(2) \cdot \frac{t}{T_{1/2\ corr}}} \tag{5.5}$$

where t is the travel time from the T4 target to CERF and $T_{1/2\ corr}$ the pion half-life corrected for relativistic effects. Eq. 5.5 gives that the 95.8% of pions do not decay [52]. Hence, the actual beam composition at CERF is 60.0% pions, 35.9% protons and 4.1% kaons. By neglecting the kaon component and re-distributing it on the other components according to their respective weight, the beam effective cross-section (62.6% pions and 37.4% protons) is 7.05±0.39 mb.

For the ^{nat}Cu(p,x)^{24}Na reaction the proton-induced cross-section at 120 GeV/c was assumed equal to the one calculated by Baker et al. [63] at 30, 150, 400 and 800 GeV, i.e. 3.59±0.14 mb. The pion/proton cross-section ratio was found to be equal to 0.726±0.016. The pion-induced cross-section is then 2.61±0.12 mb and the beam effective cross-section is 2.98±0.13 mb.

From Eq. 5.4 one can derive the value of the particle flux Φ' and consequently the value of the raw calibration factors (before correction, see below) for each experiment (see Table 5.4), where the uncertainties derive from the uncertainties on the activity, on the foil thickness (1%) and on the cross section (5.6% and 4.4% for ^{27}Al(p,3pn)^{24}Na and ^{nat}Cu(p,x)^{24}Na, respectively). The uncertainty on the

Table 5.4: *Raw calibration factors (before correction) as calculated from Eq. 5.4 [52].*

Measurement	**Foil thickness** [mm]	**Raw calibration factor** [particles per IC-count]
1	2.000 (Al)	27848±1679
2	2.000 (Al)	27224±1941
3	1.000 (Al)	25235±1997
4	0.500 (Al)	23581±1725
5	1.000 (Cu)	22297±1437
6	0.500 (Cu)	21343±1742
7	0.500 (Cu)	19953±1344
8	0.250 (Cu)	22924±1833
9	0.125 (Cu)	23191±2587
10	0.125 (Cu)	19412±2561

beam composition, which did not vary during the experiment, is not taken into account since it is below 2% [65].

The calibration factors from the aluminium activation need to be corrected for the contribution of the competing reactions to the overall activity. To take into account this contribution, which is proportional to the thickness of the foil, one has to extrapolate the calibration factor to zero thickness. Figure 5.11 plots the calibration factors calculated from the different ^{27}Al activation experiments with the corresponding least square linear fit. The extrapolated value is 22392±2090 particles/IC-count, where the uncertainty is calculated via the reduced χ-square method. This correction is not needed for the values obtained from the copper activation (Figure 5.12), since the secondary neutrons do not produce ^{24}Na. For the measurements performed with the Cu samples we can assume that, being the results compatible within their range of uncertainties, the competing reactions induced by energetic secondary hadrons are of little importance. The best estimation for the calibration factor, obtained via the weighted average method, is 21417±713 particles/IC-count. All the results given above are based on the following assumptions.

- The ^{27}Al and ^{nat}Cu atoms are homogeneously distributed in the exposed foils. This is guaranteed by the supplier.

- The effect of the impurities present in the foils on the induced activity is negligible. This has been verified via FLUKA simulations in which the impurities

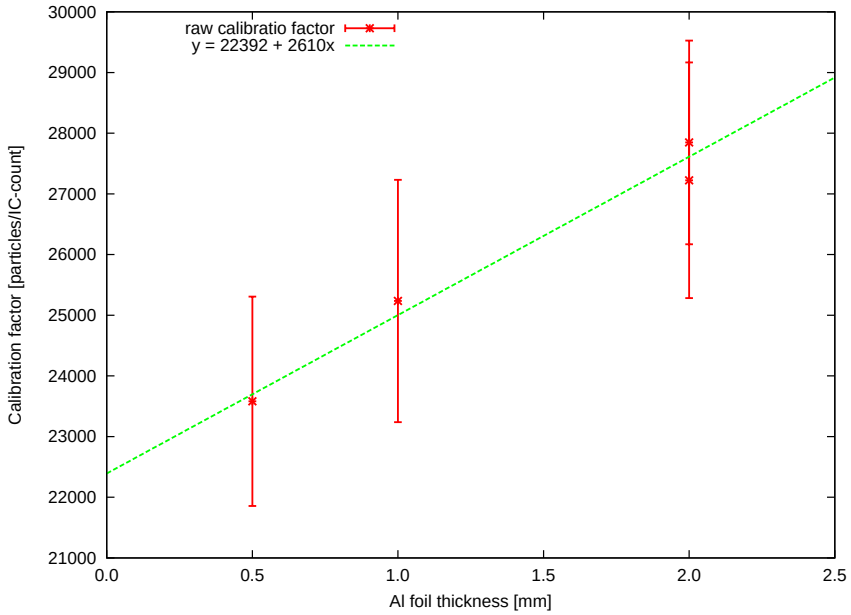

Figure 5.11: *Calibration factor calculated via the activation of the aluminum foils and the linear fit to the data.*

declared by the supplier have been included in the foils. The difference in the activity by adding the impurities is less than 1%.

- The self-absorption of γ-rays in the foils is negligible. This has been verified by taking into account the attenuation of the photons emitted by ^{24}Na in 2 mm of ^{27}Al and 0.5 mm of ^{nat}Cu. Since the mass attenuation coefficients are $3.54{\cdot}10^{-2}$ cm^2/g and 3.59 cm^2/g [66], respectively, the maximum attenuation that the γ-rays can undergo before being detected by the spectrometer is less than 2%. This small effect is taken into account by the spectrometry software.

5.2.5 Discussion

The values of the calibration factor as derived via the activation of the aluminium and the copper foils are consistent within their range of uncertainties. These results were compared with the estimation of calibration factor via FLUKA simulations, i.e 22172±789 particles per IC-count; the last is in good agreement with the value determined experimentally. The present results are also in good agreement with past experimental results obtained with different calibration techniques (Table 5.5 and Figure 5.13): production of ^{18}F in Al foils (23000±2300 par-

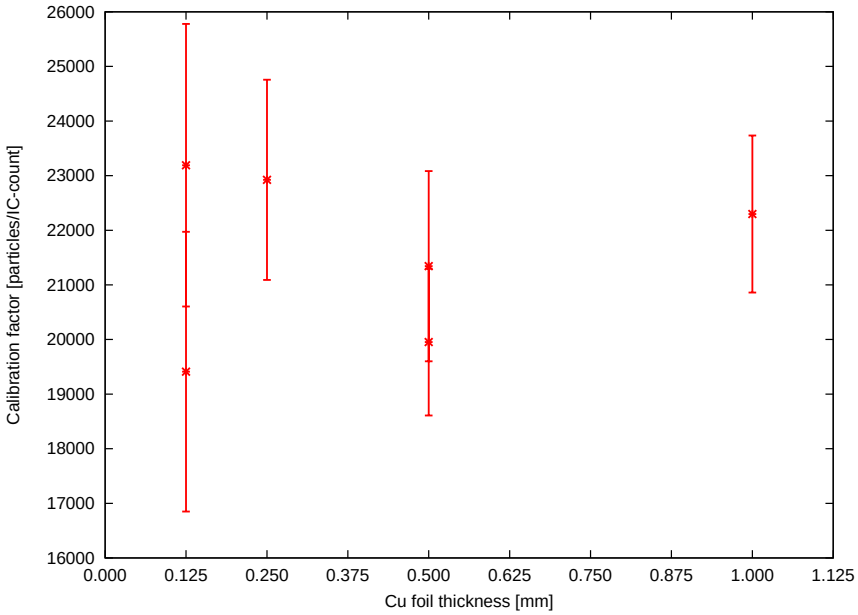

Figure 5.12: *Calibration factor calculated via the activation of the copper foils.*

ticles per IC-count [67]) and of ^{11}C in ^{12}C foils (23400±1400 particles per IC-count [57]), and coincidence of scintillators (22116±92 particles per IC-count [68]).

The ^{27}Al(p,3pn)^{24}Na confirmed to be a suitable reaction even though some considerations have to be made. Two competing mechanisms lead to the production of ^{24}Na from ^{27}Al: the ^{27}Al(n,α)^{24}Na reaction and the reactions induced by energetic secondary hadrons. The ^{27}Al(n,α)^{24}Na reaction has a threshold of 5.5 MeV and a cross section rising to 120 mb at 14 MeV [69]. Data in the literature are contradictory about the importance of this effect. Some authors showed it has little importance: Stehney [70] measured a contribution of less than 1% per 200 mg/cm^2 foil thickness, while Cumming et al. [71] proposed a value of 0.25% per 100 mg/cm^2. Other authors estimated a bigger importance: Brandt et al. [72] reported that this effect has an influence in the order of 1.1±0.5% per 100 mg/cm^2, while Grover [73] showed a strong dependence on foil thickness, about 3.3% per 100 mg/cm^2. All these estimates refer to protons; no data are available for different particles. The contribution of the competing reactions has here been determined by analysing the results obtained from the experiment. It is worth noting that this contribution may also depend on the materials present upstream and downstream of the target as well as on the characteristics of the resulting neutron "halo". One can express the calibration factor as the sum of two terms (see Eq. 5.6): the first is due to the activity induced by the primary particles, the second to the activity induced by the secondary particles, neutrons and high energy hadrons, which is

Table 5.5: *Calibration factors as calculated in past experiments, compared with the IC reference value [52].*

Calibration type	**Calibration factor** particles per IC-count	**Standard deviation**
Al-27	22392	2090
Cu	21417	713
FLUKA	22172	789
F-18 [67]	23000	2300
C-12 [57]	23400	1400
Scintillators [68]	22116	92
Reference	22000	2200

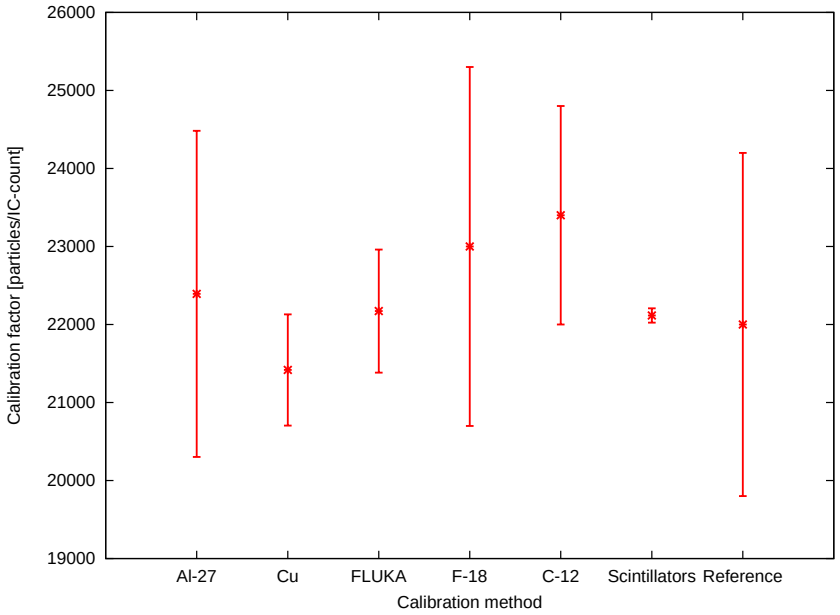

Figure 5.13: *Plot of the calibration factors as calculated via different experiments, compared with the reference value used in past years [52].*

proportional to the foil mass thickness and to a coefficient k, expressed in percent per 100 mg/cm^2 [59]:

$$C_x = C_{prim} + k \cdot C_{prim} \cdot x \tag{5.6}$$

where C_x is the calibration factor obtained for a foil of mass thickness x and C_{prim} is the calibration factor extrapolated to zero thickness. The constant k here refers to the partial activity due to the primary particles, whereas in other papers the contribution refers to the total activity. This choice was done to make Eq. 5.6 more consistent, even if the numerical difference is nevertheless of little importance. One can derive the value of the constant k from the linear fit in Figure 5.11: C_{prim} = 22392 particles per IC-count, $k \cdot C_{prim}$ = 2610 particles per IC-count per mm. By normalising the constant to the foil mass thickness (1 mm = 271 mg/cm^2, see Table 5.2) one then obtains $k = 0.117\ mm^{-1} = 4.3\%\ per\ 100\ mg/cm^2$, close to the data of Grover for protons [73]. It must be noted that the value obtained by Grover refers to the ^{27}Al(n,α)^{24}Na reaction only, whereas here the two contributions from neutrons and energetic secondary hadrons cannot be evaluated separately.

Another effect to be taken into account is the recoil nuclei effect; therefore, only the activity of the central foil of the sandwich was employed in Eq. 5.4, except for measurement 1. The loss of nuclei knocked out of the foil is in fact not compensated in the case of the upstream one. To verify the importance of the effect, for some measurements several analysis were carried out (see Table 5.3). However, all the activity values are compatible within 2σ. This shows that the importance of this effect is limited. This is confirmed by the FLUKA interaction models, which give a mean energy of the recoil ^{24}Na nuclei of about 2 MeV. This corresponds to a projected range of 2 μm in the Al target, i.e. only the nuclei produced in the last layer (a few microns) of the foil escape in the beam direction. This fraction corresponds to a maximum of about 0.4% on the overall activity for the 0.5 mm sandwich [59].

The IC calibration performed via the activation of copper foils showed results consistent with those obtained by the better known activation of aluminium foils. Moreover, due to the higher accuracy with which the cross-section of the ^{nat}Cu(p,x)^{24}Na reaction is known, the final uncertainty is lower. The validity of this alternative reaction is also confirmed by the agreement with the results obtained from the FLUKA simulations. The ^{nat}Cu(p,x)^{24}Na reaction has the advantage that there are no competing neutron-induced reactions producing ^{24}Na and that the contribution from energetic secondary hadrons is negligible. The importance of the recoil nuclei effect is limited also in this case, since the mean energy of the recoil ^{24}Na nuclei is 11 MeV, which corresponds to a projected range of 3 μm in the Cu target, i.e. about 2.5% of the overall activity for the 0.125 mm sandwich.

The reference calibration factor of 22000±2200 particles per IC-count was therefore confirmed by the ^{27}Al and ^{nat}Cu activation, and by the FLUKA calculations.

5.3 Upgraded radiation field characterization: new simulations and measurements

CERF reference spectra and dose values were calculated in 1997 by means of the FLUKA code [51], hereafter FLUKA-1997. Since then many progresses have been made in the code and several major versions have been released. Among the various developments, the following are of great importance for the calculations of the CERF reference values (for more details see Chapter 2 and Ref. [74]).

- Already starting from Fluka2006.3, a new high energy event generator has been developed, based on the sophisticated nuclear physics of PEANUT coupled with the proved FLUKA Dual Parton Model description for hadron-hadron collisions and a brand new Glauber cascade treatment. This model will eventually substitute as default the old one (PEANUT is already the default below 5 GeV). It is not yet the default, mostly because it is heavier on CPU, and results are hardly different above 10-15 GeV, unless residual nuclei are of interest. Also the new model potentially provides a fully featured simulation of high energy quasi-elastic events, which requires cleaning up some FLUKA inconsistencies before being activated.

- Several improvements in the hadron-nucleus event generators have been implemented.

- The old 72 groups neutron library has been declared obsolete and is no longer distributed. New neutron cross-section library below 20 MeV, including 260 neutron and 42 gamma groups: 31 neutron groups are thermal (1 in the previous library). All neutron cross-section data are freshly computed from the most recent evaluated nuclear data files. The new 260 group library is now the default one (even though the "old" 72 group one is still distributed). The transition energy between the group and the model treatment for neutrons is now 20 MeV and no longer 19.6 MeV.

- The default material temperature is now 296 K and no longer 293 K, which has some importance for the cross-section employed in the code.

For these reasons and in view of the CERF accreditation as a simulated workplace reference field, new FLUKA simulations were performed with the development version of the code, hereafter FLUKA-2015, that will be released in Spring

2015. For the time being, the new simulations were performed only for the target position under the concrete roof in order to validate the method; it is foreseen to carry out simulations and measurements in the future for the target position under the iron roof. The results of the simulations were compared with neutron measurements performed during the December 2014 CERF run.

5.3.1 New FLUKA simulations of the CERF facility

The input file was created starting from the 1997 original version; few changes were made in the geometry (Figure 5.14) after *in situ* measurements. The 8 concrete side positions, which were not present in the old version, were added to the input file as well as several USRTRACK and AUXSCORE cards to score directly the neutron H*(10) in spheres 12 cm in radius, the centre of which at 25 cm above the concrete roof (CT = concrete top) and at 25 cm from the concrete side (CS) wall for the CS1, CS2, CS3 and CS4 positions and at 75 cm from the same wall for the CS5, CS6, CS7 and CS8 positions. The following parameters were also included:

- the external event generators DPMJET and RQMD were linked to perform interactions at energies larger than 125 MeV/n;
- evaporation and coalescence mechanism were activated with two PHYSICS cards;
- IONSPLITting option, which activates the superposition model, i.e. ion splitting into nucleons, was switched on between 100 MeV/n and 150 MeV/n;
- pair production and bremmsstrahlung were both activated with a photon energy threshold of 30 keV for explicit bremsstrahlung production;
- photonuclear interactions were activated at all energies;
- the transport of ions (A>1) was activated including nuclear interactions with the IONTRANSport card;
- DELTARAY card activated the delta ray production by muons and charged hadrons with a threshold of 500 keV;
- PART-THReshold cards were inserted for setting the proton and muon kinetic energy cut-off at 1 MeV.

Three sets of simulations were run: one for protons, one for positive pions and one for positive kaons. The results were then averaged according to the beam

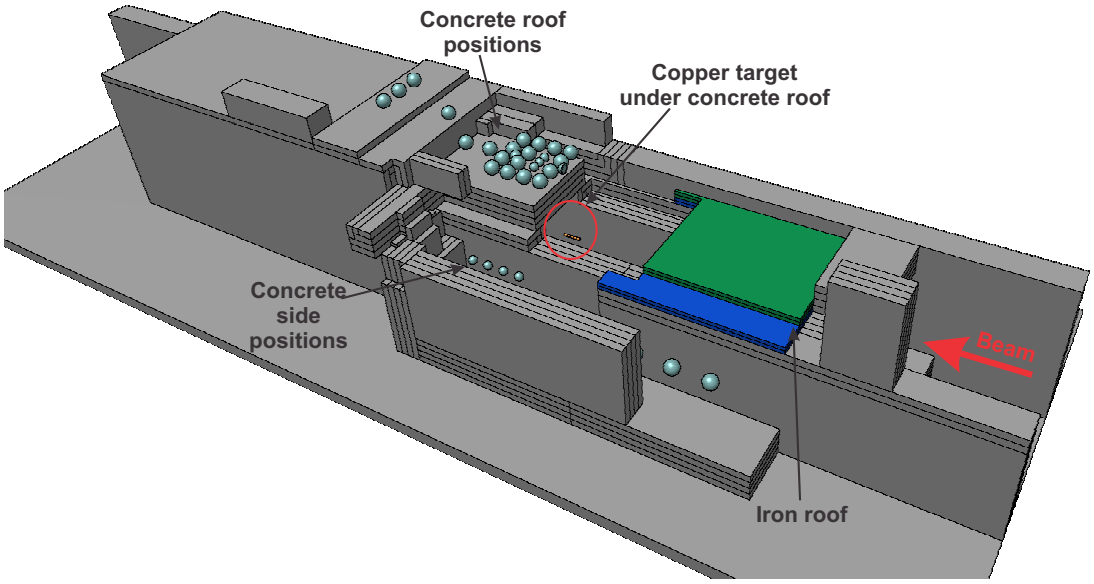

Figure 5.14: *Cross-sectional view of the CERF facility.*

composition, i.e. 61% pions, 35% protons and 4.1% kaons. The beam composition, as already mentioned, takes into account the pion decay, which was not included in the previous FLUKA results reported in Ref. [51].

5.3.2 FLUKA-1997 and FLUKA-2015 comparison

Figures 5.15-5.18 compare the neutron spectral fluence between FLUKA-2015 and FLUKA-1997 for some of the concrete roof positions. The main difference concerns the thermal part of the spectrum: FLUKA-2015 with its 31 neutron groups for thermal energies (against the 1 of FLUKA-1997) obviously has a better resolution, which results in a well-defined thermal peak. The high-energy part of the spectrum for FLUKA-2015 extends to about 2 GeV, instead FLUKA-1997 simulated up to 1 MeV, which is probably due to some cut-off applied in the old simulations. Figure 5.19 compares the neutron spectral fluences obtained with FLUKA-2015 for two side positions (CS2 and CS5) and for one position on the roof (CT5). The neutron spectra on the side have higher intensities than those on the concrete roof and show a much higher thermal peak; the last is the results of the neutron scattering with the concrete wall located behind the side locations (Figure 5.14). Unfortunately, the side spectra were not available for FLUKA-1997 and thus a comparison is not possible. The analysis of the integrated fluence and of the neutron H*(10) allows other differences to be observed.

Table 5.6 and Figure 5.20 show the integrated neutron fluence for the concrete

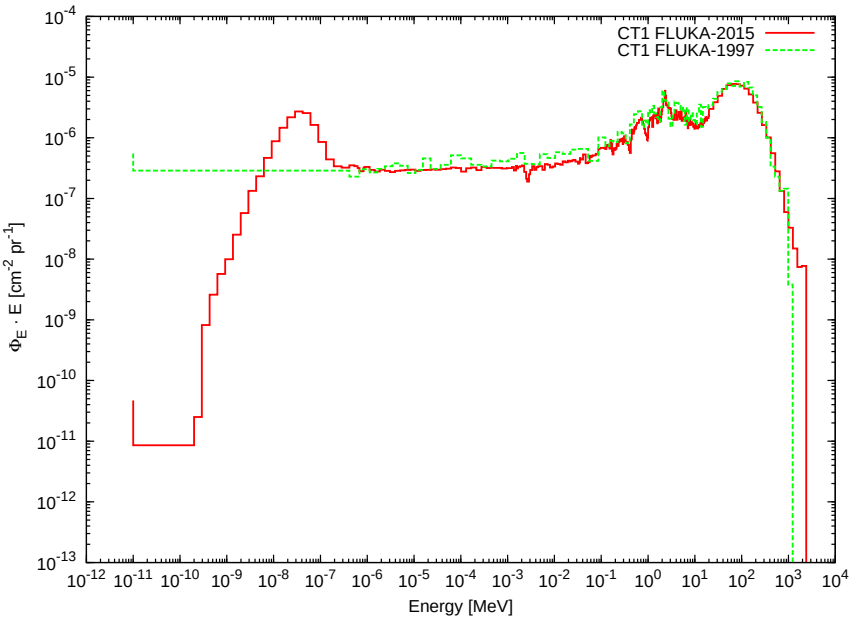

Figure 5.15: *Comparison of the neutron spectral fluence between FLUKA-2015 and FLUKA-1997 for position CT1.*

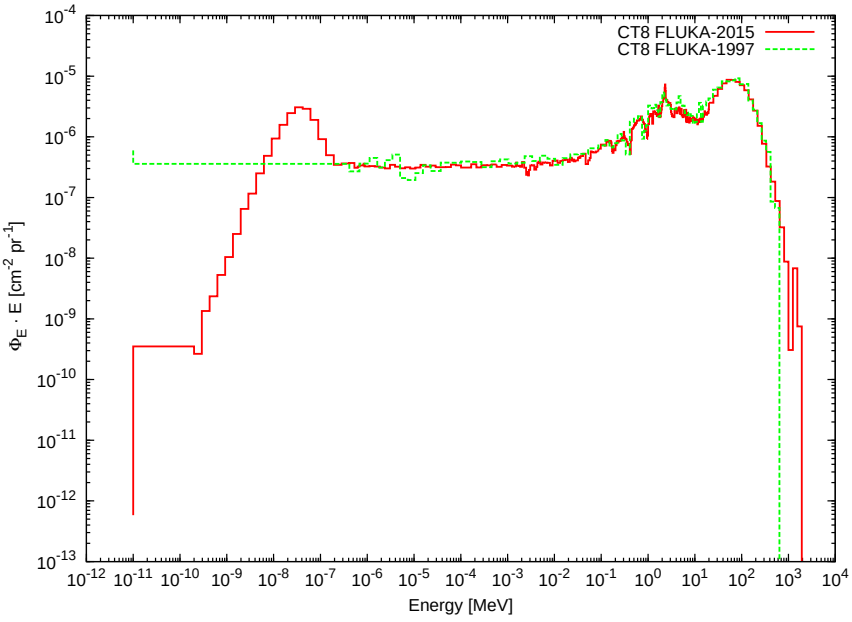

Figure 5.16: *Comparison of the neutron spectral fluence between FLUKA-2015 and FLUKA-1997 for position CT8.*

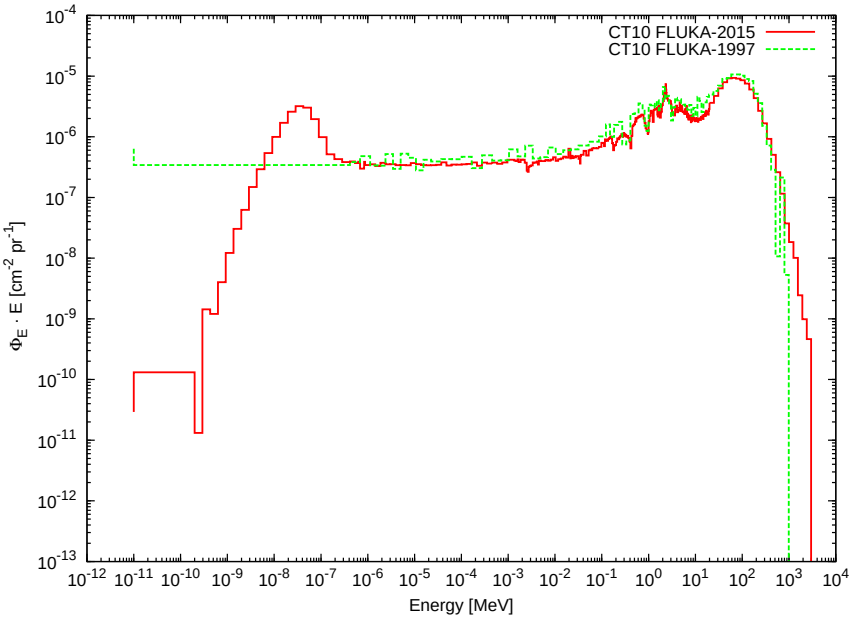

Figure 5.17: *Comparison of the neutron spectral fluence between FLUKA-2015 and FLUKA-1997 for position CT10.*

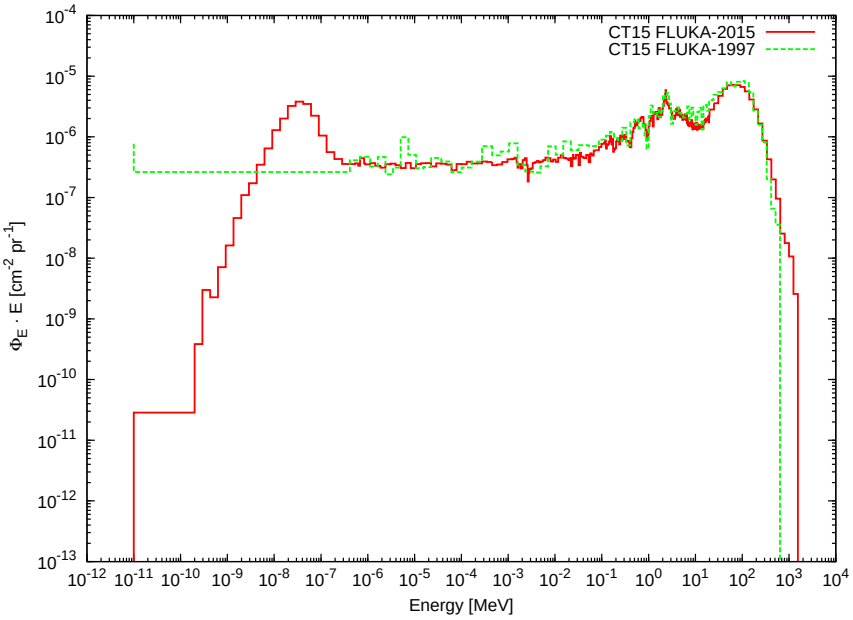

Figure 5.18: *Comparison of the neutron spectral fluence between FLUKA-2015 and FLUKA-1997 for position CT15.*

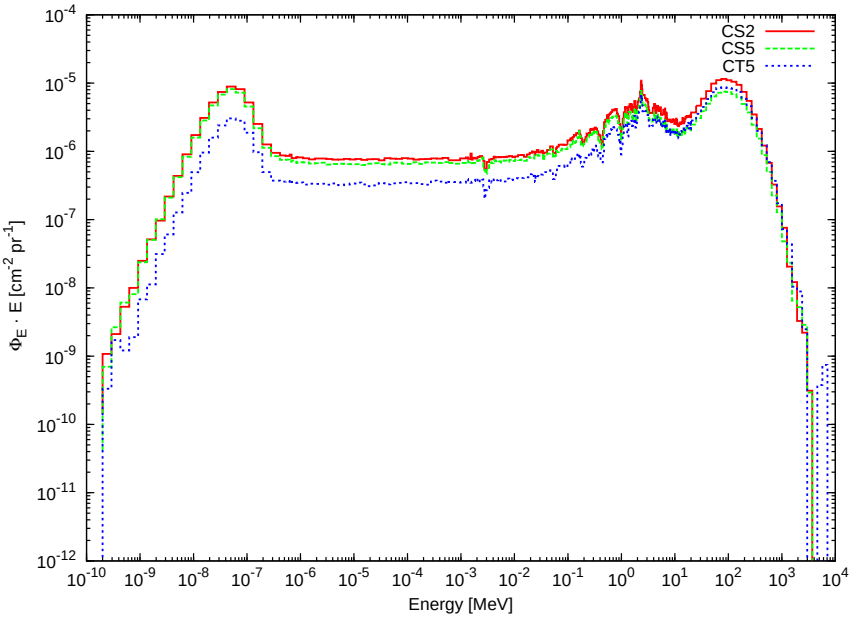

Figure 5.19: *Comparison of the neutron spectral fluence for two concrete side positions (CS2 and CS5) and one roof position (CT5) obtained with FLUKA-2015.*

reference positions. FLUKA-1997 overestimates the neutron fluence by 16% on the average. Table 5.7 and Figure 5.21 compare the neutron H*(10) from FLUKA-2015 and FLUKA-1997 for the concrete roof positions (H*(10) side values are reported only for FLUKA-2015 since no data are available for FLUKA-1997). FLUKA-1997 overestimates the neutron H*(10) by about 11% on the average. The differences between FLUKA-1997 and FLUKA-2015 are not unexpected and may be explained by the more accurate models used in the FLUKA-2015 [75], by the geometrical modifications (Section 5.3.1) and by the slightly different beam composition. Finally, Figure 5.22 shows the spectral fluence for several particles (protons, positive and negative pions, photons, electrons and positrons, and muons) compared with the neutron one for position CT8.

5.3.3 Benchmark of the FLUKA-2015 simulation results

The neutron ambient dose equivalent rates from FLUKA-2015 listed in Section 5.3.2 were benchmarked and validated by means of measurements performed with the WENDI-2 rem-counter in the December 2014 CERF run. It should be noted that even though many data are available in the literature concerning neutron measurements at CERF, many of them are not suitable to perform an accurate comparison with the FLUKA values since several parameters, which can strongly

Table 5.6: *Integrated neutron fluence for FLUKA-1997 and FLUKA-2015. The uncertainties are not listed since always lower than 1%. For the concrete side positions the FLUKA-1997 values are not available.*

Position	**FLUKA-2015** [part/cm^2/pr]	**FLUKA-1997** [part/cm^2/pr]	**Ratio FL-1997/FL-2015**
CT1	$3.41 \cdot 10^{-5}$	$3.96 \cdot 10^{-5}$	1.16
CT2	$3.50 \cdot 10^{-5}$	$3.93 \cdot 10^{-5}$	1.12
CT3	$3.43 \cdot 10^{-5}$	$3.80 \cdot 10^{-5}$	1.11
CT4	$3.02 \cdot 10^{-5}$	$3.25 \cdot 10^{-5}$	1.08
CT5	$3.91 \cdot 10^{-5}$	$4.51 \cdot 10^{-5}$	1.16
CT6	$4.11 \cdot 10^{-5}$	$4.67 \cdot 10^{-5}$	1.13
CT7	$4.06 \cdot 10^{-5}$	$4.72 \cdot 10^{-5}$	1.16
CT8	$3.62 \cdot 10^{-5}$	$3.97 \cdot 10^{-5}$	1.09
CT9	$3.83 \cdot 10^{-5}$	$4.58 \cdot 10^{-5}$	1.20
CT10	$4.06 \cdot 10^{-5}$	$4.83 \cdot 10^{-5}$	1.19
CT11	$4.00 \cdot 10^{-5}$	$4.68 \cdot 10^{-5}$	1.17
CT12	$3.55 \cdot 10^{-5}$	$4.04 \cdot 10^{-5}$	1.14
CT13	$3.22 \cdot 10^{-5}$	$3.89 \cdot 10^{-5}$	1.21
CT14	$3.52 \cdot 10^{-5}$	$4.08 \cdot 10^{-5}$	1.16
CT15	$3.50 \cdot 10^{-5}$	$4.05 \cdot 10^{-5}$	1.16
CT16	$3.13 \cdot 10^{-5}$	$3.63 \cdot 10^{-5}$	1.16
CS1	$6.71 \cdot 10^{-5}$	n.a.	n.a.
CS2	$6.81 \cdot 10^{-5}$	n.a.	n.a.
CS3	$6.59 \cdot 10^{-5}$	n.a.	n.a.
CS4	$5.83 \cdot 10^{-5}$	n.a.	n.a.
CS5	$5.33 \cdot 10^{-5}$	n.a.	n.a.
CS6	$5.35 \cdot 10^{-5}$	n.a.	n.a.
CS7	$5.10 \cdot 10^{-5}$	n.a.	n.a.
CS8	$4.55 \cdot 10^{-5}$	n.a.	n.a.

Table 5.7: *Neutron H*(10) in nSv per IC-count for FLUKA-1997 and FLUKA-2015. The uncertainties are not listed since always lower than 1%.*

Position	**FLUKA-2015** [nSv/IC-count]	**FLUKA-1997** [nSv/IC-count]	**Ratio FL-1997/FL-2015**
CT1	0.196	0.216	1.10
CT2	0.205	0.225	1.10
CT3	0.202	0.213	1.05
CT4	0.177	0.185	1.04
CT5	0.228	0.254	1.12
CT6	0.241	0.270	1.12
CT7	0.239	0.267	1.12
CT8	0.212	0.223	1.05
CT9	0.221	0.253	1.14
CT10	0.236	0.270	1.15
CT11	0.233	0.265	1.14
CT12	0.206	0.221	1.07
CT13	0.176	0.207	1.17
CT14	0.187	0.222	1.19
CT15	0.184	0.207	1.12
CT16	0.163	0.182	1.12
CS1	0.312	n.a.	n.a.
CS2	0.325	n.a.	n.a.
CS3	0.317	n.a.	n.a.
CS4	0.278	n.a.	n.a.
CS5	0.231	n.a.	n.a.
CS6	0.235	n.a.	n.a.
CS7	0.225	n.a.	n.a.
CS8	0.198	n.a.	n.a.

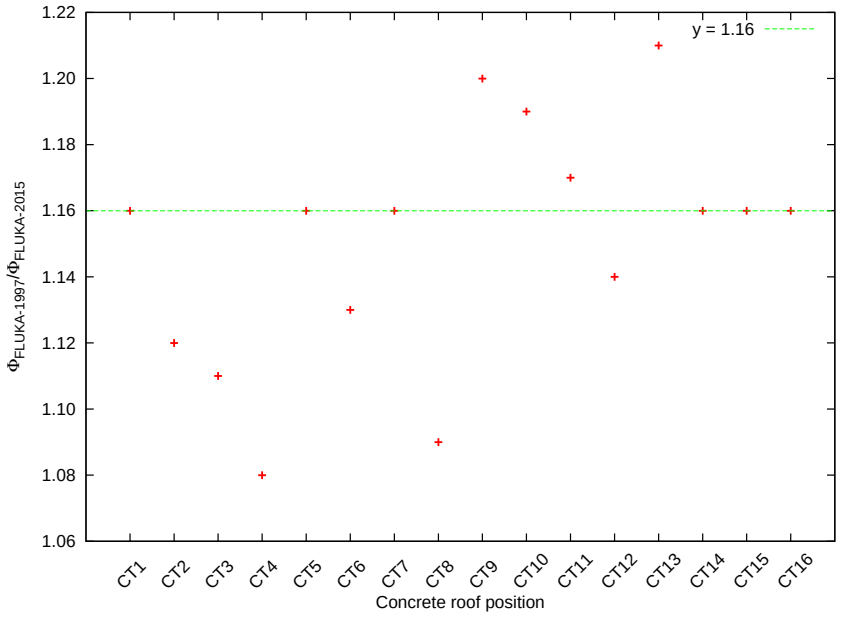

Figure 5.20: *Ratio of the neutron fluence for FLUKA-1997 and FLUKA-2015 for the concrete roof positions. The green line is the average difference.*

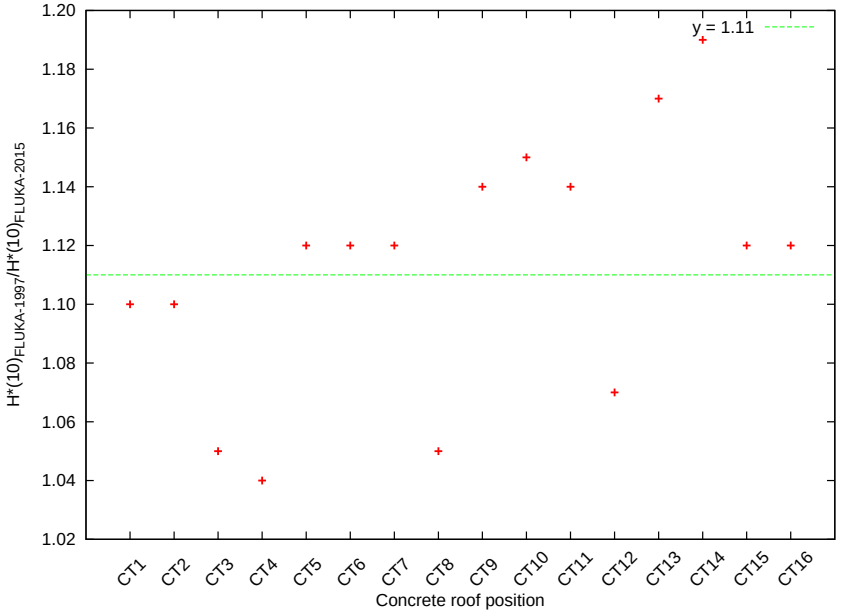

Figure 5.21: *Ratio of the neutron H*(10) for FLUKA-1997 and FLUKA-2015 for the concrete roof positions. The green line is the average difference.*

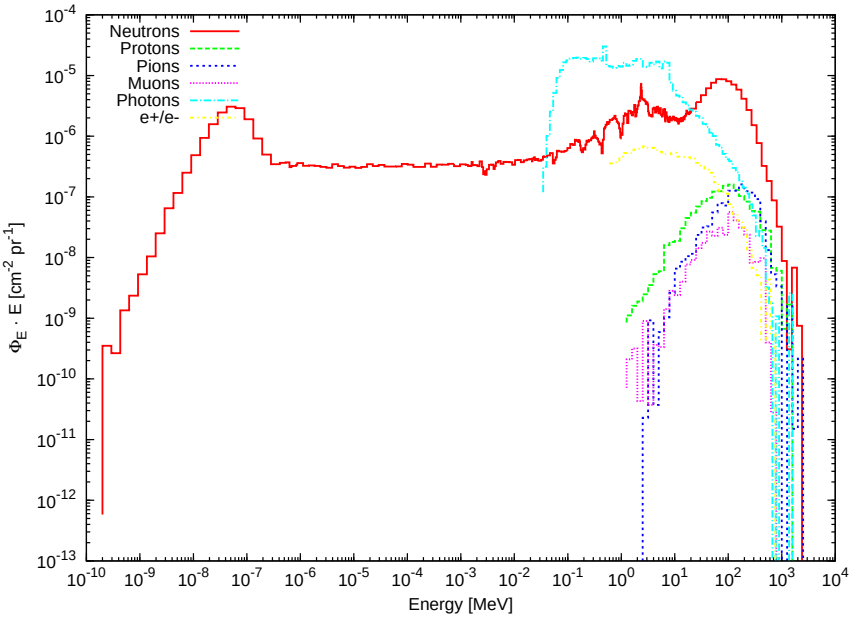

Figure 5.22: *Spectral fluence for several particles in position CT8 obtained with FLUKA-2015.*

influence the data analysis, are not known, e.g. exact distance of the detector from the concrete roof (FLUKA reference values are given at 25 cm), variation of the count rate with the beam intensity, detector calibration factors. For the purpose of this work, the comparison with the WENDI-2 measurements was considered sufficient to provide a first validation of the results; however, intercomparisons of several neutron detectors are foreseen at CERF in the next years (2015-2017) in view of the accreditation of CERF as simulated workplace reference field.

Figure 5.23 shows the ratio between the H*(10) measurements carried out with the WENDI-2 and the new FLUKA reference values. The FLUKA results and WENDI-2 measurements are fairly in agreement within 1σ on the concrete roof (CT1, CT2, CT5, CT8, CT7 and CT9 positions); the WENDI-2 overestimates by about 20% to 40% the neutron H*(10) on the concrete side. In order to explain the difference between simulations and measurements, the following elements must be taken into account.

- The response function of the WENDI-2 does not exactly reproduce the ICRP74 [17] fluence-to-dose conversion coefficients (Figure 5.24).
- The WENDI-2 overestimates the H*(10) in the epithermal part of the spectrum and in particular at high neutron energies (from about 60 MeV); therefore, one can expect an overestimation of H*(10) for neutron fields clearly

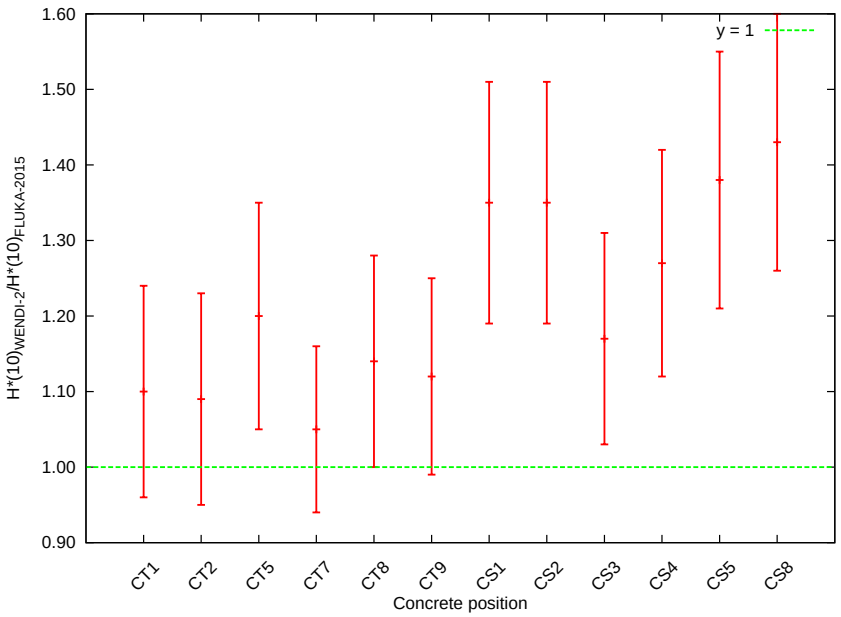

Figure 5.23: *Ratio of the neutron H*(10) from the measurements performed with the WENDI-2 and the new FLUKA reference values. The green line represents the ratio equal to one. WENDI-2 CT7 measurement is taken from ref. [76].*

dominated by energies above 100 MeV as at CERF.

- The WENDI-2 calibration factor of 3024 counts per μSv provided by the manufacturer comes from a calibration with a Cf-252 source (fluence-average energy of 2.13 MeV [3]), whereas the CERF spectrum is completely different.

A possible way to account for the effect of different radiation fields is obtained by introducing specific correction factors. These correction factors are determined recording simulated neutron spectra which are then convoluted with the pure WENDI-2 response function as well as with the conversion coefficients for ambient dose equivalent. The ratio of the two integrated energy spectra eventually yields field calibraton factors in units of counts per μSv. Subsequently these results have to be divided by the sensitivity of the detector (counts per $\mu\mathrm{Sv}_{Cf-252}$) given by the manufacturer to determine the correction factors [78]. Before implementing this approach, which lies on the accurate simulation of the experimental situation, the FLUKA neutron fluence spectra were validated by convoluting them with the WENDI-2 response function; this yielded the WENDI-2 "simulated" neutron H*(10) that was compared with the experimental measurements. The agreement between the two represented the degree of accuracy of the simulations. Afterwards the correction factor was calculated and applied to the WENDI-2 measurements.

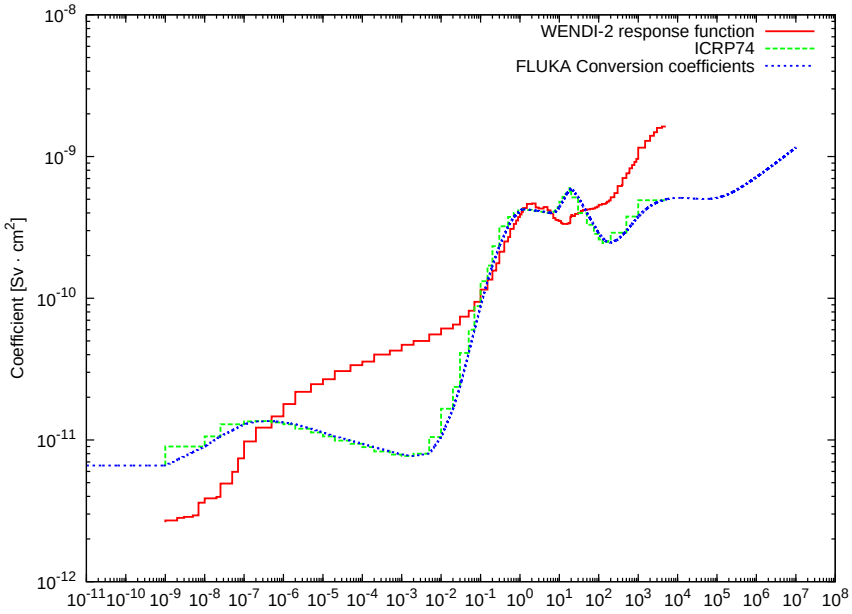

Figure 5.24: *Response function of the WENDI-2 [19], ICRP74 [17] fluence-to-dose conversion coefficients and FLUKA fluence-to-dose conversion coefficients [77].*

To validate the methodology, the FLUKA neutron fluence spectra were firstly convoluted with the FLUKA fluence-to-dose conversion coefficients [77] to reproduce the H*(10) as directly simulated. For simplicity the linear interpolation method was employed even though the 4-point Lagrangian interpolation formula on a log-log scale is recommended by ref. [17]. The results reproduced exactly (less than 3‰ difference) the FLUKA neutron H*(10) validating this approach. Then, the FLUKA neutron fluence spectra were convoluted with the pure WENDI-2 response function [19] obtaining the integrated counts, i.e. WENDI counts per IC-count. The counts were divided by the WENDI-2 calibration factor of 3024 counts per μSv, as provided by the manufacturer, resulting in the WENDI-2 "simulated" neutron H*(10); the last was then compared with the measured neutron H*(10). Table 5.8 shows the results of the convolution together with the FLUKA reference values and the WENDI-2 experimental measurements. On the concrete roof the H*(10) is satisfactory reproduced since all values are within 1σ as shown in Figure 5.25. On the concrete side, the agreement is not as good since the convolution results sistematically underestimate the H*(10). A characteristic trend from CS1 to CS8 is present both for the experimental measurements and for the WENDI-2 "simulated" values. The rather high difference on the concrete side may be explained in terms of the simulated geometry, which was not accurate enough to reproduce the concrete side neutron spectra. The last are dominated not only

Table 5.8: *Neutron H*(10) for several positions obtained by FLUKA, by measurements with the WENDI-2 (WENDI-2 Expt.) and by convoluting the FLUKA fluence spectra with the WENDI-2 response function (WENDI-2 Sim.). The last column list the ratio between the WENDI-2 Expt. values and the WENDI-2 Sim. ones.*

Position	**FLUKA** H*(10) [nSv/IC]	**WENDI-2 Expt.** H*(10) [nSv/IC]	**WENDI-2 Sim.** H*(10) [nSv/IC]	**Ratio Expt./Sim.**
CT1	0.196± 0.023	0.215± 0.026	0.235± 0.024	0.91
CT2	0.205± 0.025	0.224± 0.028	0.242± 0.025	0.93
CT5	0.228± 0.026	0.272± 0.033	0.272± 0.028	1.00
CT7	0.239± 0.028	0.260± 0.027	0.276± 0.028	0.94
CT8	0.212± 0.026	0.241± 0.028	0.241± 0.025	1.00
CT9	0.221± 0.026	0.248± 0.029	0.264± 0.027	0.94
CS1	0.312± 0.034	0.422± 0.049	0.366± 0.037	1.15
CS2	0.325± 0.035	0.437± 0.051	0.378± 0.039	1.16
CS3	0.317± 0.034	0.372± 0.041	0.362± 0.037	1.03
CS4	0.278± 0.031	0.353± 0.039	0.310± 0.032	1.14
CS5	0.231± 0.026	0.318± 0.037	0.266± 0.027	1.20
CS8	0.198± 0.023	0.283± 0.033	0.219± 0.022	1.29

by high-energy neutrons but also by thermal and epithermal neutrons (as shown in Figure 5.19), mainly originated by scattering from the surrounding structures; therefore, a much more accurate modeling of these elements is required to employ the concrete side positions as reference locations.

Given the good agreement between simulations and experimental values on the concrete roof, the WENDI-2 correction factors were determined following the procedure described above. Table 5.9 lists the correction factors and the corrected neutron H*(10). For the correction factors, uncertainties of about 10% have to be taken into account, which arise from intrinsic uncertainties of the response function and the source spectra. Figure 5.26 shows the ratio between the corrected neutron H*(10) and the FLUKA reference values; on the concrete roof the corrected H*(10) agree better with the ones from FLUKA than those not corrected (see also Figure 5.23). On the side the values show a better agreement than before the correction but as already mentioned they cannot be employed as reference.

The benchmark conducted for the FLUKA-2015 simulations with the WENDI-2 measurements validated the reliability of the FLUKA reference values for the

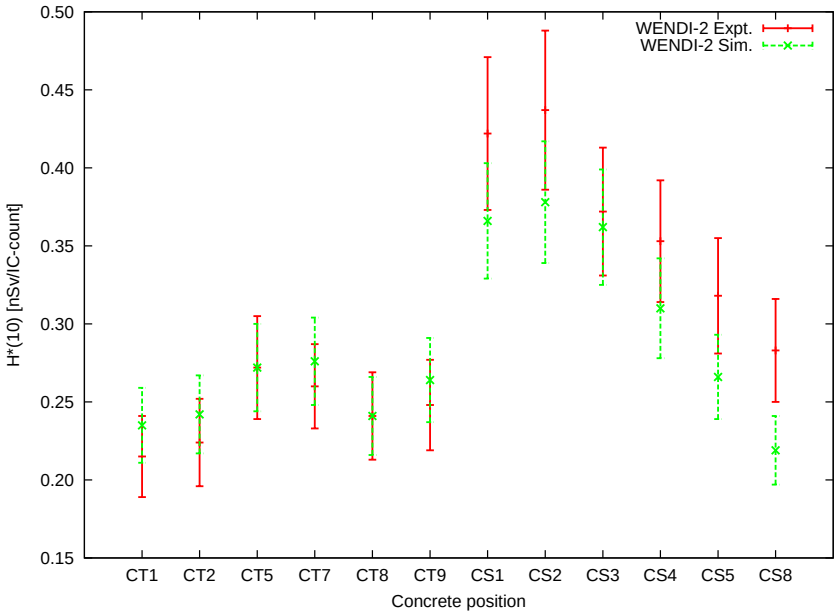

Figure 5.25: *Plot of the neutron H*(10) measured with the WENDI-2 (WENDI-2 Expt.) and the ones obtained by the convolution of the FLUKA fluence spectra and the WENDI-2 response function (WENDI-2 Sim.).*

concrete roof positions. The field correction factors had to be calculated and applied since the WENDI-2 was calibrated in a radiation field very different from the CERF one. In view of the accreditation process several improvements and further analysis have to be taken into account:

- accurate geometry modeling to validate the concrete side reference values;
- chemical analysis of the CERF concrete to be included in the simulations;
- neutron measurement intercomparison employing other detectors, e.g. LINUS, TEPC;
- simulation of the neutron spectral fluences with the target under the iron roof and validation via measurements.

Table 5.9: *WENDI-2 neutron H*(10) values corrected via the correction factors (shown in column 2) for several positions. The ratio with the new FLUKA reference values is listed in column 4.*

Position	**Correction factor**	**WENDI-2 Corr.** [nSv/IC]	**Ratio WENDI-2 Corr./FLUKA**
CT1	1.20± 0.12	0.179± 0.041	0.91± 0.21
CT2	1.18± 0.12	0.190± 0.042	0.92± 0.21
CT5	1.20± 0.12	0.227± 0.052	1.00± 0.23
CT7	1.16± 0.12	0.225± 0.044	0.94± 0.18
CT8	1.14± 0.11	0.212± 0.042	1.00± 0.20
CT9	1.20± 0.12	0.207± 0.046	0.94± 0.21
CS1	1.18± 0.12	0.359± 0.076	1.15± 0.25
CS2	1.17± 0.12	0.375± 0.078	1.15± 0.24
CS3	1.14± 0.11	0.325± 0.064	1.03± 0.20
CS4	1.12± 0.11	0.315± 0.059	1.14± 0.22
CS5	1.16± 0.12	0.275± 0.057	1.19± 0.25
CS8	1.11± 0.11	0.256± 0.048	1.29± 0.24

5.4 Cross-section measurements at CERF

Spallation cross-sections from thin natural copper and iron targets bombarbed by the CERF beam were measured in an activation experiment. The activity of several spallation products (13 for copper and 15 for iron) was measured by γ-spectrometry, allowing the absolute cross-section of the mixed hadron beam to be derived. FLUKA simulations provided the ratio between the proton- and pion-induced reaction cross-sections for a given spallation product, allowing to extrapolate the individual cross-sections for the proton- and the pion-induced reactions (see Sections 5.2.3 and 5.2.4). The values were also compared with existing literature data showing that CERF does not provide only a simulated workplace reference field, but its potentialities extend to the high-energy physics research. It is worth noting that this experiment relies on the proper calibration of the IC (Section 5.2).

5.4.1 Motivations

Spallation refers to nuclear inelastic reactions that occur when subatomic particles with incident energy higher than 100-150 MeV interact with a target nucleus.

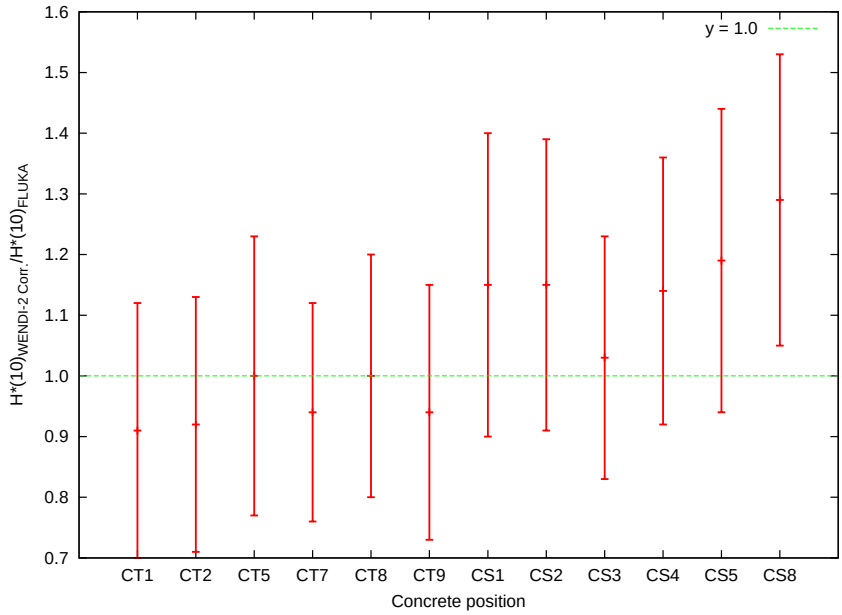

Figure 5.26: *Neutron H*(10) ratio between the WENDI-2 measurements corrected for the CERF field and the results from FLUKA. The green line is the ratio equal to one.*

At these energies the de Broglie wavelength is short enough to allow the particle to interact with the individual nucleons inside the nucleus. The incident particle first undergoes a series of reactions with the nucleons, where high-energy secondary particles (such as protons, neutrons and pions) from a few MeV up to the energy of the incident particle are created inside the nucleus (intranuclear cascade). Some of these high-energy hadrons, together with low-energy particles in the MeV range, leave the nucleus and may induce other spallation reactions in a different nucleus (internuclear cascade). This process mainly occurs in thick targets. The nucleus, which is in an excited state, relaxes by emitting low energy particles, mostly neutrons. After evaporation the final nucleus (spallation product) may be radioactive and decay by γ-emission [62].

An accurate knowledge of the spallation product inventory within a target is important for many applications: disposal of material, operation, maintenance, safety and decay heat analysis for neutron spallation sources [79], activation issues in high-energy particle accelerators [80] and benchmarking of Monte Carlo codes [81]. The knowledge of the reaction cross-section for a spallation product is therefore fundamental. Spallation cross-section data are widely available for energies up a few GeV [61], but for higher energies (especially above 28 GeV) very limited data have been published. This is particularly true for pion-induced

reactions for which no data are available. The spallation reactions used in this experiment are of direct relevance in activation studies, since ^{nat}Cu and ^{nat}Fe are commonly employed in high-energy particle accelerators and their surrounding structures [82].

5.4.2 Experimental set-up

The experiment was performed by exposing hyperpure ^{nat}Cu and ^{nat}Fe foils to the CERF primary beam. For simplicity the particle energy was assumemed to be 120 GeV, even if the actual value is slightly lower. For the calculations the kaon fraction has been re-distributed on the other two components according to their relative weight, i.e. the beam composition has been assumed to be 62.6% positive pions and 37.4% protons; this takes also into account the pion decay explained in Section 5.2.4. This re-distribution has a negligible effect because of the limited importance of the kaon component, whose relative weight is well below the final relative uncertainty on the cross-section values derived from the experiment, and because the kaon-induced spallation cross-section lies in between the proton- and the pion-induced one as verified via FLUKA simulations [82]. The beam was delivered to CERF with a typical intensity in the range 10^6 to 10^8 particles per SPS spill, with a beam extraction time of about 10 s over an SPS cycle of about 45 s.

The experimental set-up was similar to the one explained in Section 5.2.4. The ^{nat}Cu and ^{nat}Fe foils with dimensions 50 x 50 mm^2 were fixed on a Plexiglas frame mounted on both ends of a hollow aluminium tube placed downstream of the IC (see Figure 5.9). The foils were irradiated in sandwiches of three to take into account the recoil of some of the nuclei produced in the spallation process that can leave the foil in the same direction of the primary beam (Lorentz boost). To maintain the equilibrium between the loss of recoil nuclei knocked out of the foil and the gain of nuclei knocked into the foil from upstream material, only the central one must be considered for data analysis, whereas the upstream and the downstream ones act as catchers. These catchers, having the same thickness of the central foil, are thick enough to capture all the knocked on or knocked back products. The beam size was smaller than the foil dimensions so that all particles traversing the IC hit the foils [82].

The foil thicknesses were 0.5 mm, 0.25 mm and 0.125 mm for ^{nat}Cu; 2 mm for ^{nat}Fe, with 1% estimated uncertainty. The thicknesses were chosen as a compromise between the need of an induced activity high enough to reduce the statistical uncertainty of the γ-spectrometry measurements and the need of thin targets, i.e. targets in which the energy lost by the incident beam is small (E_{loss} / $E_{beam} \leq$ 5% [62]). This reduces to a minimum the production of secondary particles inside the target, which generally undergo further collisions and could result in internu-

Table 5.10: *Foil atomic surface densities [82].*

Fe foils (ρ_{Fe} = 7.874 g/cm^3, M$_{Fe}$ = 55.840 g/mol)			
Foil thickness X$_{Fe}$	2.0 mm		
N$_x$	$1.6983{\cdot}10^{22}$		cm^2
Cu foils (ρ_{Cu} = 8.920 g/cm^3, M$_{Cu}$ = 63.546 g/mol)			
Foil thickness X$_{Cu}$	0.125 mm	0.250 mm	0.500 mm
N$_x$	$1.0567{\cdot}10^{21}$ cm^2	$2.1133{\cdot}10^{21}$ cm^2	$4.2266{\cdot}10^{21}$ cm^2

clear cascades. By assuming that the value of the interaction lengths for protons and pions at 120 GeV is similar to the one at 18 GeV (i.e. 140.2±3.2 g/cm^2 for protons, 163.8±9.0 g/cm^2 for pions [83]), the beam fraction that interacts in the target is always less than 1% [82]. This guarantees that overall influence of the target on the beam transmission is negligible. Furthermore, the average fraction of energy of the incident beam lost in the target was estimated simulating a 120 GeV proton beam impinging on an iron target 2.0 mm thick by means of FLUKA code. The results showed that it is about 1%.

The hyperpure ^{nat}Cu and ^{nat}Fe foils have the following compositions, as declared by the manufacturer [84]: 99.991% ^{nat}Cu, with impurities in ppm: Ag 70, Fe 2, Ni 2, Pb 2, Si 2, Al 1, Bi 1, Ca 1, Mg 1, Sn 1, Mn < 1, Na < 1, Cr < 1; 99.998% ^{nat}Fe, impurities in ppm: Ag 1, Al 2, Ca 3, Cr 1, Cu 2, Mg 2, Mn 1, Ni 1, Si 3. The effect of the impurities on the radioisotope production is negligible. This has been verified via several sets of FLUKA simulations, in which the foils were first simulated as 100% pure, and then with added impurities. The values of the surface atomic densities N_x to be used in Eq. 5.7, which explains how the production cross-section σ can be calculated (see also Section 5.2.3), are obtained from the foil density, the molar mass and the thickness (Table 5.10) [82].

$$\sigma = \frac{A(t)}{N_x \Phi' (1 - e^{-\lambda \cdot t_{IRR}}) e^{-\lambda \cdot t_{WAIT}}} \tag{5.7}$$

The beam intensity recorded by the IC was written every second in a log-file, from which the value of Φ' to be used in Eq. 5.7 was obtained. Since the beam intensity was recorded every second, the irradiation time was subdivided in one second irradiation slots (t_{IRR} = 1 s). For each of these slots a corresponding waiting time t_{WAIT} was considered. Thanks to this method any fluctuation in the beam intensity during the irradiation was properly taken into account. The foils were counted in the CERN γ-spectrometry laboratory with a Canberra low

background coaxial high-purity germanium (HPGe) detector. For a more accurate analysis of the gamma lines, the activated foils were counted twice: a short (10 minutes) measurement immediately after the irradiation and a longer one (about 8 hours) later. The analysis was performed using the Canberra Genie 2000 and the PROcount 2000 software. They include a set of spectrum analysis algorithms, which provide nuclide identification, interference correction, weighted mean activity, background subtraction and efficiency correction. They also take into account geometrical effects, self-absorption in the sample and decay of the isotope during the measurements, and provide a global uncertainty. Only the radioisotopes with an activity higher than 1 Bq were considered for the cross-section calculations [82].

5.4.3 Results and discussion

The beam effective cross-section σ for each of the reactions of interest was derived from Eq. 5.7 by employing the values of N_x, Φ', $A(t)$, t_{WAIT} and t_{IRR}, obtained as explained in Section 5.4.2. The cross-sections of the proton- and pion-induced reactions were calculated from Eq. 5.8 and 5.9.

$$\sigma_\pi = \frac{\sigma}{0.626 + 0.374\frac{\sigma_p}{\sigma_\pi}} \tag{5.8}$$

$$\sigma_p = \frac{\sigma - 0.626\sigma_\pi}{0.374} \tag{5.9}$$

Tables 5.11 and 5.12 list the cross-sections of the spallation reactions that generated an activity in the foils higher than 1 Bq. The global uncertainty is the quadratic sum of the uncertainty on the γ-spectrometry, the one on the IC calibration factor (10%) and the uncertainty on the foil thickness, i.e. on the knowledge of N_x. The uncertainty on the beam composition is not taken into account since it is below 2% [65]. The production of the listed radioisotopes derives only from the proton- and pion-induced spallation reactions. For the reactions on ^{nat}Cu foils the cross-section is the average of the values obtained from the three thicknesses.

A comparison between the cross-section obtained at 120 GeV and the ones found in the literature at lower energies is given in Figures 5.27 and 5.28; this shows the data available for proton-induced spallation reactions (for the pion-induced reactions no data are available) at energies higher than 500 MeV. The comparison shows that in most cases the cross-section at 120 GeV is comparable with the values available at the highest energies, i.e. around 20-30 GeV, confirming that the cross-section is energy independent above a certain energy. This behaviour is coherent with the fact that above about a few hundred MeV, the total elastic and non-elastic cross-sections for hadron-nucleus collisions are approximately constant [62]. This is foreseen by many physical models: the Sihver

Table 5.11: *Cross-sections of the spallation reactions on ^{nat}Cu derived from the activation experiment.*

Nuclear reaction	**Cross-section**	**Nuclear reaction**	**Cross-section**
^{nat}Cu(p,x)^{42}K	2.20±0.39 mb	^{nat}Cu(π+,x)^{42}K	1.67±0.30 mb
^{nat}Cu(p,x)^{43}K	0.91±0.19 mb	^{nat}Cu(π+,x)^{43}K	0.65±0.14 mb
^{nat}Cu(p,x)^{43}Sc	2.72±0.26 mb	^{nat}Cu(π+,x)^{43}Sc	2.61±0.25 mb
^{nat}Cu(p,x)^{44}Sc	3.79±0.17 mb	^{nat}Cu(π+,x)^{44}Sc	3.45±0.15 mb
^{nat}Cu(p,x)^{47}Sc	1.83±0.21 mb	^{nat}Cu(π+,x)^{47}Sc	1.41±0.17 mb
^{nat}Cu(p,x)^{48}Cr	0.21±0.06 mb	^{nat}Cu(π+,x)^{48}Cr	0.21±0.06 mb
^{nat}Cu(p,x)^{48}Sc	1.15±0.21 mb	^{nat}Cu(π+,x)^{48}Sc	0.81±0.15 mb
^{nat}Cu(p,x)^{52}Mn	3.83±0.52 mb	^{nat}Cu(π+,x)^{52}Mn	3.87±0.52 mb
^{nat}Cu(p,x)^{55}Co	0.51±0.10 mb	^{nat}Cu(π+,x)^{55}Co	0.56±0.11 mb
^{nat}Cu(p,x)^{56}Mn	2.65±0.14 mb	^{nat}Cu(π+,x)^{56}Mn	1.98±0.10 mb
^{nat}Cu(p,x)^{57}Ni	0.77±0.14 mb	^{nat}Cu(π+,x)^{57}Ni	0.77±0.14 mb
^{nat}Cu(p,x)^{58}Co	18.79±6.00 mb	^{nat}Cu(π+,x)^{58}Co	18.03±5.76 mb
^{nat}Cu(p,x)^{61}Cu	11.14±0.51 mb	^{nat}Cu(π+,x)^{61}Cu	11.47±0.52 mb

model [85], valid for $Z_{target} \leq 26$, which assumes that in a proton-nucleus interaction the cross-section is energy-independent for energies above 200 MeV; the limiting fragmentation model [86], which assumes the energy-independence of the cross-section for sufficiently high energies of the bombarding particle; the Letaw model [87], valid for $Z_{target} > 5$, which assumes that in a proton-nucleus interaction the cross-section is energy independent above 2 GeV, with a possible small increase at very high energies ($\geq$ 100 GeV); the Glauber model [88], which allows to compute reliably the hadron-nucleus cross-section on the basis of the hadron-proton one and of the nuclear density distribution, which predicts cross-sections almost constant at energies above a few GeV with a slow increase at the highest energies.

The outcome of this experiments shows that the CERF facility is suitable to be employed for cross-section measurements at very high-energies. This makes CERF a very powerful facility, the use of which can go from radiation protection, e.g. dosimetry and calibration of survey-meters, to high-energy physics experiments.

Table 5.12: *Cross-sections of the spallation reactions on ^{nat}Fe derived from the activation experiment.*

Nuclear reaction	**Cross-section**	**Nuclear reaction**	**Cross-section**
^{nat}Fe(p,x)^{24}Na	3.97±0.44 mb	^{nat}Fe(π+,x)^{24}Na	2.92±0.33 mb
^{nat}Fe(p,x)^{42}K	4.22±0.57 mb	^{nat}Fe(π+,x)^{4}2K	3.14±0.42 mb
^{nat}Fe(p,x)^{43}K	1.39±0.19 mb	^{nat}Fe(π+,x)^{43}K	0.90±0.12 mb
^{nat}Fe(p,x)^{43}Sc	3.72±0.63 mb	^{nat}Fe(π+,x)^{43}Sc	3.73±0.63 mb
^{nat}Fe(p,x)^{44}Sc	8.30±0.93 mb	^{nat}Fe(π+,x)^{44}Sc	7.85±0.88 mb
^{nat}Fe(p,x)^{46}Sc	6.01±2.33 mb	^{nat}Fe(π+,x)^{46}Sc	4.82±1.87 mb
^{nat}Fe(p,x)^{47}Sc	3.90±0.53 mb	^{nat}Fe(π+,x)^{47}Sc	2.89±0.40 mb
^{nat}Fe(p,x)^{48}Cr	0.59±0.08 mb	^{nat}Fe(π+,x)^{48}Cr	0.64±0.08 mb
^{nat}Fe(p,x)^{48}Sc	0.60±0.13 mb	^{nat}Fe(π+,x)^{48}Sc	0.36±0.08 mb
^{nat}Fe(p,x)^{48}V	16.53±2.08 mb	^{nat}Fe(π+,x)^{48}V	16.23±2.05 mb
^{nat}Fe(p,x)^{51}Cr	29.41±11.59 mb	^{nat}Fe(π+,x)^{51}Cr	28.14±11.09 mb
^{nat}Fe(p,x)^{52}Fe	0.50±0.07 mb	^{nat}Fe(π+,x)^{52}Fe	0.54±0.08 mb
^{nat}Fe(p,x)^{52}Mn	10.32±1.16 mb	^{nat}Fe(π+,x)^{52}Mn	10.49±1.18 mb
^{nat}Fe(p,x)^{54}Mn	44.75±8.82 mb	^{nat}Fe(π+,x)^{54}Mn	43.14±8.50 mb
^{nat}Fe(p,x)^{55}Co	0.61±0.08 mb	^{nat}Fe(π+,x)^{55}Co	0.51±0.07 mb

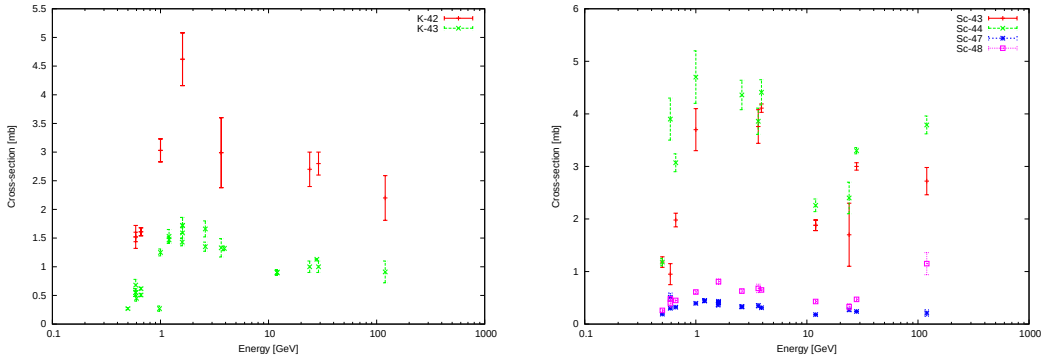

(a) *Potassium*

(b) *Scandium*

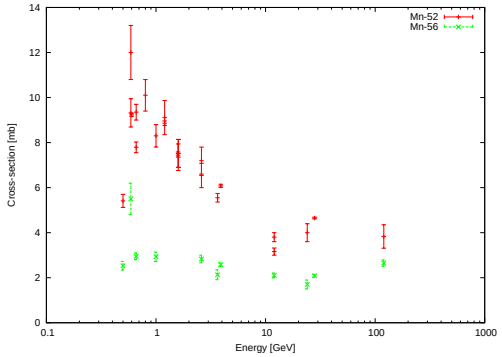

(c) *Manganese*

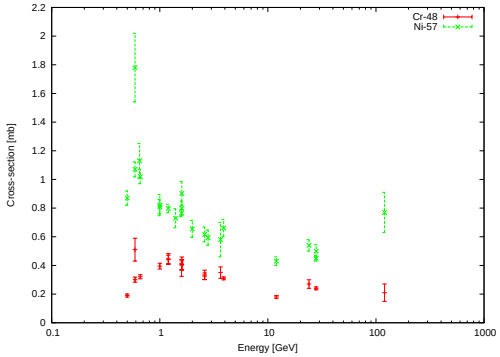

(d) *Chromium and Nickel*

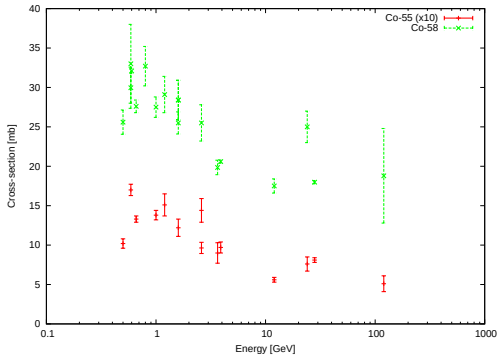

(e) *Cobalt*

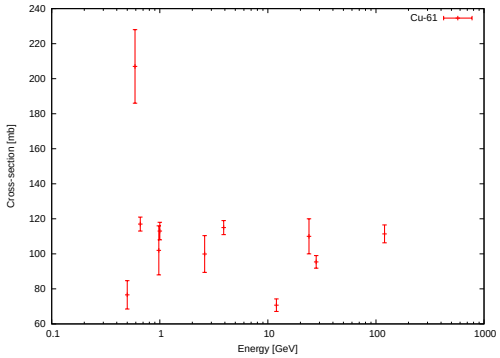

(f) *Copper*

Figure 5.27: *Cross-sections of the spallation reactions on ^{nat}Cu for the production of several isotopes.*

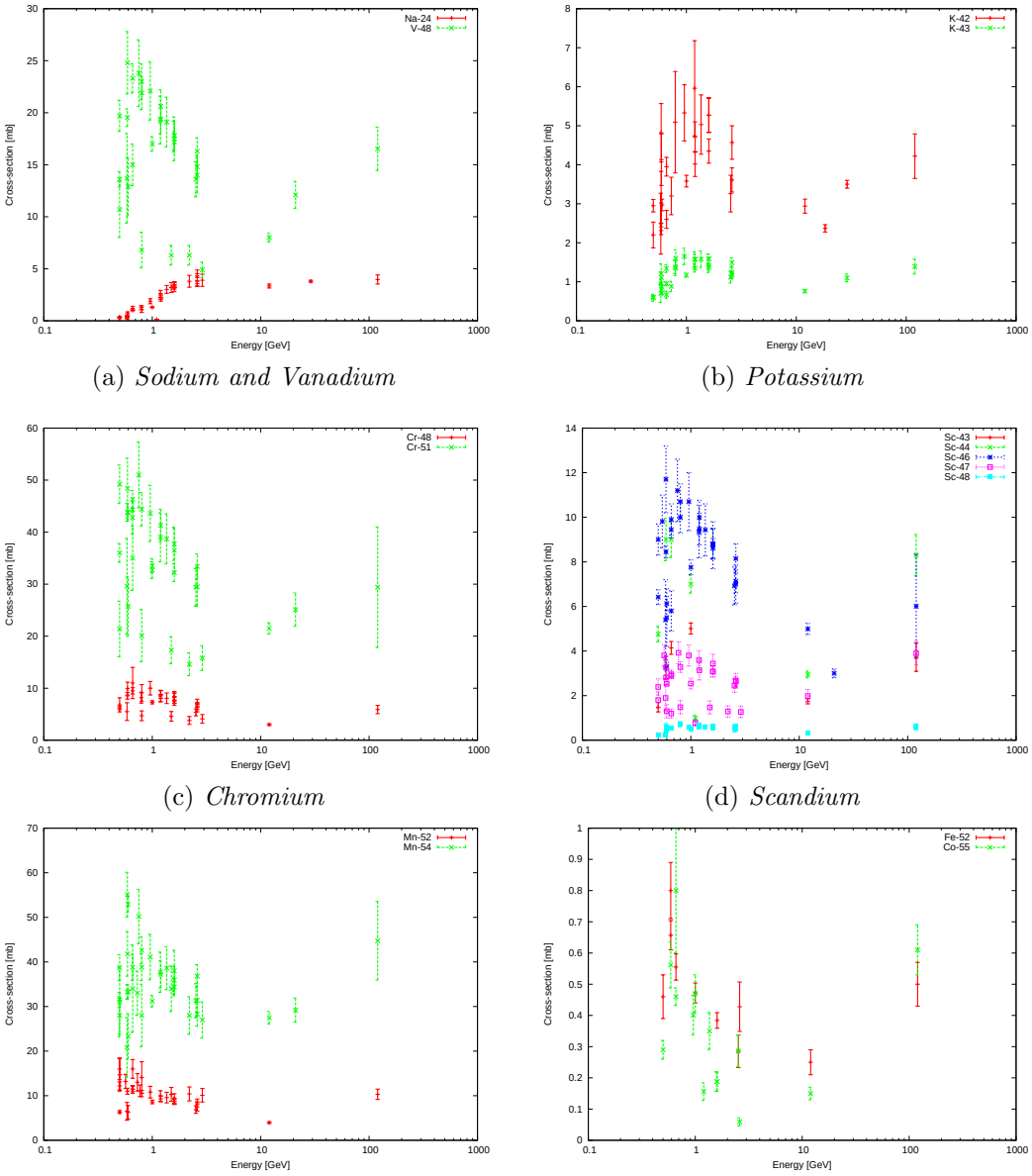

(a) *Sodium and Vanadium* (b) *Potassium*

(c) *Chromium* (d) *Scandium*

(e) *Manganese* (f) *Iron and Cobalt*

Figure 5.28: *Cross-sections of the spallation reactions on ^{nat}Fe for the production of several isotopes.*

Conclusions

A new state-of-the-art calibration facility was designed and built at CERN. A fundamental optimization work was carried out during the design phase by means of MC simulations: building design, shielding definitions, calculation of air and concrete activation, verification of the ozone production for the 11.8 TBq Co-60 source, and study of the skyshine effect. The Monte Carlo method was also used to assess the influence of scattered neutrons in the calibration positions since their contribution shall be subtracted from measurements. The neutron radiation field was characterized by measuring the H*(10) through the SmartREM rem-counter; the results were then analyzed by using the generalized-fit method in order to consider the scattered neutron contribution. This procedure provided an accurate characterization of the neutron radiation field for the current use of the laboratory. The air-kerma rate from the gamma sources was measured with ionization chambers; special care was taken to calculate the uncertainty budget. Even though the facility is already operational, there are still new perspectives for the continuation of the project.

- Shadow-cone design. A set of shadow-cones to assess the neutron scattering contribution will be designed using Monte Carlo calculations to optimize the shape and the number of cones.

- Finalization of the neutron field characterization. Bonner Sphere measurements will be carried out to determine the neutron spectrum at some calibration positions. The results will be compared with the MC simulations presented in this work.

- Accreditation as Secondary Standard Laboratory. An accreditation procedure will be undertaken in order to be able to provide official calibration certifications. This will require to document technical manuals and a quality assurance program; since ISO recommendations were followed during the entire work, the accreditation will be straightforward.

The work performed for the new calibration facility was integrated and completed by characterizing the CERF facility, a unique workplace field that simulates

the neutron spectrum encountered in the proximity of high-energy accelerators and at commercial flight altitudes. The calibration factor of the CERF beam monitor was verified by the well-know ^{27}Al activation technique. Another activation reaction (on the ^{nat}Cu) was also investigated and showed to be suitable. The characterization of the CERF radiation field was carried out with the present development version of the FLUKA code; upgraded neutron spectra and H*(10) reference values to be used for calibrations were provided. The FLUKA results were also benchmarked with recent WENDI-2 measurements showing a good agreement, especially on the concrete roof positions. Eventually, the capabilities of CERF allowed high-energy spallation cross-sections on ^{nat}Fe and ^{nat}Cu to be measured for the first time; these cross-sections are of great importance for e.g. activation issues in high-energy particle accelerators, and for benchmarking MC codes. However, in order to make CERF an accredited workplace neutron field, the following studies and measurements still have to be performed.

- Intercomparison of neutron detectors on the concrete roof and comparison with Monte Carlo results.
- Investigation of the simulation results on the concrete side positions and new FLUKA simulations with the copper target placed under the iron roof; the results will be benchmarked with experimental measurements.
- Design and construction of a back-up beam monitor.
- Design and construction of a new target support system for improving the beam set-up.
- Accreditation as workplace radiation field: validation of the calibration techniques and reference values, estimation of the uncertainties and redaction of the quality assurance manuals.

Bibliography

[1] S. Pomp, D. T. Bartlett, S. Mayer, G. Reitz, S. Rottger, M. Silari, F. D. Smit, H. Vincke, and H. Yasuda. High-energy quasi-monoenergetic neutron fields: existing facilities and future needs. Technical report, EURADOS, 2013.

[2] H. Schuhmacher. Neutron calibraton facilities. *Radiation Protection Dosimetry*, 110:33–42, 2004.

[3] Reference neutron radiations - Characteristics and methods of production, 2001. ISO 8529-1.

[4] Reference radiation fields - Simulated workplace neutron fields - Characteristics and methods of production, 2008. ISO 12879-1.

[5] X and gamma reference radiation for calibrating dosemeters and doserate meters and for determining their response as a function of photon energy - Radiation characteristics and production methods, 1996. ISO 4037-1.

[6] S. A. Dupree and S. K. Fraley. *A Monte Carlo Primer, A practical approach to radiation transport*. Springer Science+Business Media, LLC, 2002.

[7] G. A. Holton. Value-at-Risk: Theory and Practice. `http://value-at-risk.net`.

[8] N. Metropolis and S. Ulam. The monte carlo method. *Journal of the American Statistical Association*, 44(247):335–341, 1949.

[9] S. Agostinelli et al. GEANT4 - a simulation toolkit. *Nuclear Instruments and Methods in Physics Research A*, 506:250–303, 2003.

[10] J. Allison et al. Geant4 developments and applications. *IEEE Transactions on Nuclear Science*, 53:270–278, 2006.

[11] A. W. Chao and M. Tigner, editors. *Handbook of Accelerator Physics and Engineering*, chapter 1. World Scientific Publishing Co. Pte. Ltd., 2009.

[12] D. B. Pelowitz. *MCNPX User's Manual, Version 2.5.0*. Los Alamos National Laboratory, April 2005. LA-CP-05-0369.

[13] T. Sato et al. Particle and Heavy Ion Transport code System, PHITS, version 2.52. *Journal of Nuclear Science and Technology*, 50(9):913–923, 2013.

[14] A. Ferrari, P. R. Sala, A. Fassò, and J. Ranft. FLUKA: a multi-particle transport code. CERN 2005-10 (2005), INFN/TC_05/11, SLAC-R-773.

[15] T. T. Böhlen, F. Cerutti, M. P. W. Chin, A. Fassò, A. Ferrari, P. G. Ortega, A. Mairani, P. R. Sala, G. Smirnov, and V. Vlachoudis. The FLUKA Code: Developments and Challenges for High Energy and Medical Applications. *Nuclear Data Sheets*, 120:211–214, 2014.

[16] Glenn F. Knoll. *Radiation Detection Measurement*. John Wiley & Sons, Inc., 4^{th} edition, 2010.

[17] Conversion Coefficients for use in Radiological Protection against External Radiation, 1996. ICRP Publication 74.

[18] C. Birattari, A. Ferrari, C. Nuccetelli, M. Pelliccioni, and M. Silari. An Extended Range Neutron Rem Counter. *Nuclear Instruments and Methods in Physics Research A*, 297:250–257, 1990.

[19] L. Jagerhofer, E. Feldbaumer, C. Theis, S. Roesler, and H. Vincke. A new method to calculate the response of the WENDI-II rem counter using the FLUKA Monte Carlo Code. *Nuclear Instruments and Methods in Physics Research A*, 691:81–85, 2012.

[20] `http://www.thermoscientific.com`.

[21] R. H. Olsher, H. H. Hsu, A. Beverding, J. H. Kleck, W. H. Casson, D. G. Vasilik, and R. T. Devine. WENDI: an improved neutron rem meter. *Health Physics*, 79(2):170–181, 2000.

[22] Berthold technologies gmbh & co. KG. `https://www.berthold.com`.

[23] B. Burgkhardt, G. Fieg, A. Klett, A. Plewnia, and B. R. L. Siebert. The neutron fluence and H*(10) response of the new lb 6411 remcounter. *Radiation Protection Dosimetry*, pages 361–364, 1997.

[24] J. W. Leake, T. Lowe, and R. S. Mason. Improvements to the Leake Neutron Detector I. *Nuclear Instruments and Methods in Physics Research A*, 519:636–646, 2004.

[25] https://www.fst-sensortechnik.com/seiten/frms1.html.

[26] *Safety code F*, 2006. https://edms.cern.ch/file/335729/2/F_E.PDF.

[27] S. Agosteo, M. Magistris, A. Mereghetti, M. Silari, and Z. Zajacova. Shielding data for 100-250 MeV proton accelerators: double differential distributions and attenuation in concrete. *Nuclear Instruments and Methods B*, 265:581–589, 2007.

[28] P. Carbonez, F. Pozzi, and H. Vincke. Neutron background measurements on the Prévessin site. Technical Report EDMS 1386952, CERN, 2014.

[29] C. Theis, D. Forkel-Wirth, M. Fuerstner, S. Mayer, Th. Otto, S. Roesler, and H. Vincke. Field calibration studies for ionisation chambers in mixed high-energy radiation fields. *Radiation Protection Dosimetry*, (126):299–305, 2007.

[30] Reference neutron radiations - Calibration fundamentals of radiation protection devices related to the basic quantities characterizing the radiation field, 2000. ISO 8529-2.

[31] S. Damjanovic, S. Gilardoni, S. Roesler, J. Vollaire, and M. Widorski. Shielding studies for the route Goward/PS crossing. Technical Report EDMS 1161799, CERN, 2011.

[32] https://www.nucleonica.com/Application/Shielding.aspx.

[33] A. H. Sullivan. *A guide to radiation and radioactivity levels near high energy particle accelerators*. Nuclear Technology Publishing, 1992.

[34] A.J. Koning and D. Rochman. Modern nuclear data evaluation with the TALYS code system. *Nuclear Data Sheets*, 113, 2012.

[35] Ordonnance sur la radioprotection (ORaP) du 22 juin 1994. https://www.admin.ch/opc/fr/classified-compilation/19940157/index.html.

[36] Francesco Paolo La Torre, private communication.

[37] A. Fassó, K. Goebel, M. H́ofert, C. Nuttal, and A. Perrot. Formation d'ozone dans l'anneau principal du LEP et sa dispersion dans l'atmosphere par le systeme de ventilation. Technical Report LEP note 379, CERN, 1982.

[38] A. Chevalier, F. Gheusi, R. Delmas, C. Ordóñez, C. Sarrat, R. Zbinden, V. Thouret, G. Athier, and J.-M. Cousin. Influence of altitude on ozone levels and variability in the lower troposphere: a ground-based study for western Europe over the period 2001-2004. *Atmospheric Chemistry and Physics*, 7:4311–4326, 2007.

[39] `https://www.nws.noaa.gov/ost/air_quality/FAQs.htm`.

[40] J. F. Kircher, J. S. McNulty, J. L. McFarling, and A. Levy. Irradiation of Gaseous and Liquid Oxygen. *Radiation Research*, 13:452–465, 1960.

[41] Z. I. Kertesz and G. F. Parsons. Ozone formation in air exposed to Cobalt-60 gamma radiation. *Science*, 142:1289–1290, 1963.

[42] E. Aza, N. Dinar, G. P. Manessi, and M. Silari. A Bonner Sphere spectrometer for pulsed fields. *Radiation Protection Dosimetry*, 2015. Submitted for publication.

[43] P. Carbonez and F. Pozzi. Commissioning of the new rp calibration facility. Technical report, CERN, 2015. To be published.

[44] X and gamma reference radiation for calibrating dosemeters and doserate meters and for determining their response as a function of photon energy - dosimetry for radiation protection over the energy ranges 8 keV to 1.3 MeV and 4 MeV to 9 MeV, 1997. ISO 4037-2.

[45] A. Fassò, A. Ferrari, J. Ranft, and P. R. Sala. FLUKA: Present Status and Future Developments. In A. Menzione and A. Scribano, editors, *Proceedings IV International Conference on Calorimetry in High Energy Physics*, pages 493–502, 1994. Italy, 21-26 September 1993.

[46] A. Fassò, A. Ferrari, J. Ranft, and P. R. Sala. New Developments in FLUKA Modelling of Hadronic and EM Interactions. In H. Hirayama, editor, *Proceedings on Simulating Accelerator Radiation Environments (SARE3)*, volume 97(5), pages 32–44. KEK, 1997. Tsukuba, Japan, May 1997.

[47] A. Ferrari and P. R. Sala. An Update about FLUKA. In G. R. Stevenson, editor, *Proceedings 2nd Workshop of Simulating Accelerator Environments*, pages 158–170. CERN, 1997. CERN Divisional Report TIS-RP/97-05.

[48] A. Ferrari and P. R. Sala. The Physics of High Energy Reactions. In A. Gandini and G. Reffo, editors, *Proceedings Workshop on Nuclear Reaction Data and Nuclear Reactors Physics, Design and Safety*, volume 2, pages 424–532. Internation Centre for Theoretical Physics, 1998. Miramare-Trieste, Italy 15 April-17 May 1996.

[49] Short introduction to the use of the H6 beam, 2000. http://sba.web.cern.ch/sba/BeamsAndAreas/H6/H6manual.pdf.

[50] G. Ambrosini et al. Measurement of charged particle production from 450 GeV/c protons on beryllium. *European Physical Journal C*, 10:605–627, 1999.

[51] A. Mitaroff and M. Silari. The CERN-EU high-energy Reference Field (CERF) facility for dosimetry at commercial flight altitudes and in space. *Radiation Protection Dosimetry*, 102:7–22, 2002.

[52] F. P. La Torre, G. P. Manessi, F. Pozzi, C. T. Severino, and M. Silari. A new verification of the calibration factor of the CERF beam monitor. Technical Report EDMS 1311291, CERN, 2013.

[53] A. Aroua, J. Bourges, and R. C. Raffnsoe. Beam monitoring and data logging for the H6 experiment. Technical report, CERN, 1993. CERN/TIS/RP/TM/93-20.

[54] G. Battistoni, S. Muraro, P. R. Sala, F. Cerutti, A. Ferrari, S. Roesler, A. Fassó, and J. Ranft. The FLUKA code: description and benchmarking. In *Proceedings of the Hadronic Shower Simulation Workshop 2006*, volume 49, pages 31–49. AIP Conference Proceeding, 2007. FLUKA Version 2011.2.4.

[55] Absorbed dose determination in external beam radiotherapy: an internal code of practice for dosimetry based on standards of absorbed dose to water. Technical report, IAEA, 2000. Series No. 398.

[56] J. C. Liu, S. Roesler, and G. R. Stevenson. Carbon-11 in beam measurements during the September 1993 CERN-CEC experiment. Technical report, CERN, 1993. CERN/TIS-RP/TM/93-43.

[57] G. R. Stevenson, J. C. Liu, K. O'Brien, and J. Williams. Beam intensity measurements using ^{11}C activation for the CERN-CEC experiments. Technical report, CERN, 1994. CERN/TIS/RP/TM/94-15.

[58] J. B. Cumming. Monitor reactions for high energy proton beams. *Annual Review of Nuclear Science*, 13:261–286, 1963.

[59] A. Ferrari, F. P. La Torre, G. P. Manessi, F. Pozzi, and M. Silari. Monitoring reactions for the calibration of relativistic hadron beams. *Nuclear Instruments and Methods in Physics Research A*, 763:177–183, 2014.

[60] S. B. Kaufman, M. W. Weisfield, E. P. Steinberg, B. D Wilkins, and D. J Henderson. Spallation of aluminum by 300 GeV protons. *Physical Review C*, 19:962–964, 1979.

[61] Nuclear reaction database (EXFOR), 2014. `http://cdfe.sinp.msu.ru`.

[62] D. Filges and F. Goldenbaum. *Handbook of Spallation Research*, 2009. Wiley-VCH, Weinheim.

[63] S. I. Baker, R. A. Allen, and P. Yurista. Cu(p,x)^{24}Na cross section from 30 to 800 GeV. *Physical Review C*, 43:6, 1991.

[64] C. Theis, K. H. Buchegger, M. Brugger, D. Forkel-Wirth, S. Roesler, and H. Vincke. Interactive three dimensional visualization and creation of geometries for monte carlo calculations. *Nuclear Instruments and Methods in Physics Research A*, 562:827–829, 2006.

[65] H. W. Atherton, C. Bovet, N. Doble, G. Von Holtey, L. Piemontese, A. Placci, M. Placidi, D. E. Plane, M. Reinharz, and E. Rossa. Technical report, CERN, 1980. Yellow Report 80-07.

[66] Korea Atomic Energy Research Institute (KAERI). Photon Cross-sections and Attenuation Coefficients. `http://atom.kaeri.re.kr`.

[67] M. C. Hopper, C. Raffnsoe, and G. R. Stevenson. Beam monitoring in May 1993 CERN-CEC experiments. Technical report, CERN. CERN/TIS/RP/TM/93-21.

[68] H. Vincke, S. Mayer, I. Efthymiopoulos, A. Fabich, D. Forkel-Wirth, M. J. Muller, and C. Theis. Accurate PIC calibration by the use of a coincidence of two scintillators. Technical report, CERN, 2004. CERN/SC/RP/TN/2004-090.

[69] J. P. Butler and D. C. Santry. Excitation curves for the reactions Al^{27}(n,α)Na^{24} and Mg^{24}(n,p)Na^{24}. *Canadian Journal of Physics*, 41(2):372–983, 1963.

[70] A. F. Stehney and E. P. Steinberg. The effect of thick targets on some nuclear reactions commonly used to monitor high energy proton beams. *Nuclear Instruments and Methods*, 59:102–108, 1968.

[71] J. B. Cumming, J. Hudis, A. M. Poskanzer, and S. Kaufman. Al^{27}(p,3pn)Na^{24}/C^{12}(p,pn)C^{11} Cross-Section Ratio in the GeV Region. *Physical Review Letters*, 128:2932–2397, 1962.

[72] R. Brandt, C. Gfeller, and W. Stoetzel-Riezler. Some remarks concerning the proton flux monitor reaction ^{27}Al(p,3pn)^{24}Na. *Nuclear Instruments and Methods*, 30:109–111, 1968.

[73] J. Robb Grover. Nuclear Reactions of Tantalum with 5.7 GeV Protons. *Physical Review*, 126:1540–1554, 1962.

[74] RELEASE-NOTES.fluka2011.2c.

[75] Alfredo Ferrari, private communication.

[76] M. Caresana, M. Helmecke, J. Kubancak, G. P. Manessi, K. Ott, R. Scherpelz, and M. Silari. Instrument intercomparison in the high-energy mixed field at the CERN-EU Reference Field (CERF) facility. *Radiation Protection Dosimetry*, 161:67–72, 2014.

[77] Chris Theis, private communication.

[78] L. Jagerhofer et al. Characterization of the WENDI-II REM Counter for its Application at MedAustron. *Progress in Nuclear Science and Technology*, 2:252–262, 2011.

[79] W. S. Charlton, T. A. Parish, A. P. Belian, and C. A. Beard. Measured and calculated radionuclide production from copper, gold, and lead spallation targets. *Nuclear Instruments and Methods in Physics Research B*, 142:9–16, 1998.

[80] National Council on Radiation Protection and Measurements. NCRP REPORT NO.144 - RADIATION PROTECTION FOR PARTICLE ACCELERATOR FACILITIES. *Radiation Protection Dosimetry*, 113:456–457, 2005.

[81] L. Sihver, D. Mancusi, K. Niita, T. Sato, L. Townsend, C. Farmer, L. Pinsky, A. Ferrari, F. Cerutti, and I. Gomes. Benchmarking of calculated projectile fragmentation cross-sections using the 3-D, MC codes PHITS, FLUKA, HETC-HEDS, MCNPX_HI, and NUCFRG2. *Acta Astronautica*, 63:865–877, 2008.

[82] A. Ferrari, F. P. La Torre, G. P. Manessi, F. Pozzi, and M. Silari. Spallation cross sections for ^{nat}Fe and ^{nat}Cu targets for 120 GeV/c protons and pions. *Physical Review C*, 89, 2014.

[83] H. Cranell, C. J. Cranell, H. Whiteside, J. F. Ormes, and M. J. Ryan. Interaction Lengths of Energetic Pions and Protons in Iron. *Physical Review D*, 7:730–740, 1973.

[84] GoodFellow, see online catalog at `https://www.goodfellow.com`.

[85] L. Sihver, C. H. Tsao, R. Silberberg, T. Kanai, and A. F. Barghouty. Total reaction and partial cross section calculations in proton-nucleus ($z_t \leq 26$) and nucleus-nucleus reactions (z_p and $z_t \leq 26$). *Physical Review C*, 45:1225–1236, 1993.

[86] J. Benecke, T. T. Chou, C. N. Yang, and E. Yen. Hypothesis of Limiting Fragmentation in High-Energy Collisions. *Physical Review*, 188:2159–2169, 1969.

[87] J. R. Letaw, R. Silberberg, and C. H. Tsao. Proton-nucleus total inelastic cross sections: an empirical formula for E>10 MeV. *The Astrophysical Journal Supplement Series*, 51:271–276, 1983.

[88] R. J. Glauber and G. Matthiae. High-energy scattering of protons by nuclei. *Nuclear Physics B*, 21:135–157, 1970.

Acknowledgments

After the 160 and more pages of this PhD work, now it is time to thank! Yes, because after three years of work and experience there are many people that I would sincerely like to thank.

First of all, I thank my wonderful wife, Gioia: you have been (and you are) great! You have always encouraged my work at CERN and you have always shown big consideration for what I was doing. These three years have also (in particular, I would say!) been the period of our engagement, our marriage and the birth of our amazing daughter Elodie Myriam. Thanks also to her! I will always remember that the writing phase of my thesis coincided with her period in the belly of her mother! Thank you "Micetta Panetta" for all of your gorgeous smiles!

Thanks to my mum Natalina, my dad Giuliano, my brother Daniele, his wife Nadia and their children Sara and Simone, because what I have done in these three years is also the result of what I had the possibility to do during my study career.

Thanks to my "acquired" relatives and my wonderful nephews and nieces: Emma, Loris, Pamela, Stefano, Anna, Maddalena, Giosue', Diletta, Angelica, Umberto, Serena, Ettore and Gabriele. It has always been nice to share my CERN experience with you all.

Thank you Pierre! You have been a "very" supervisor: you have followed very well my work and you have given me the possibility/responsibility of working independently. I can surely say that in addition to a supervisor I have discovered a friend.

Thank you Marco for your precious support in keeping everything on track and for your wide willingness.

Thank you Prof. Macian for having given the possibility to carry out my PhD work at TUM.

Thanks to my colleagues! Although you were not directly involved in my work, sharing with your the CERN environment/office/group has been very nice and precious for my working life. Thank you: Alessandro, Alessio, Clizia, Damiano, Eleni, Evi, Fabrizio, Francesco, Giacomo, Nesrine, Silvia, Stefano and Stuart.

Thank you Nick: you made the German bureaucracy smooth with me! I am happy to have shared the same adventure at TUM with you.